DISSERTATION

USE OF CHEMICAL IONIZATION MASS SPECTROMETRY FOR STUDY OF PHOTOCHEMICAL PROPERTIES: KETONE PHOTOLYSIS QUANTUM YIELDS

Submitted by

Tyson C. Berg

Department of Chemistry

In partial fulfillment of the requirements

For the Degree of Doctor of Philosophy

Colorado State University

Fort Collins, Colorado

Spring 2025

Doctoral Committee:

Advisor: Delphine K. Farmer

A.R. Ravishankara
Justin B. Sambur
Shantanu Jathar

ABSTRACT

USE OF CHEMICAL IONIZATION MASS SPECTROMETRY FOR STUDY OF PHOTOCHEMICAL PROPERTIES: KETONE PHOTOLYSIS QUANTUM YIELDS

Measurements of organic radicals produced during organic trace gas photolysis are critical to our understanding of radical budgets throughout the troposphere. This dissertation demonstrates the utility of chemical ionization mass spectrometry for measurements of radical quantum yields in the photolysis of organic trace gases in the laboratory setting.

Chapter 2 addresses the development of a coupled chemical ionization mass spectrometer with iodide reagent ions (I-CIMS) and wide band light source instrument design, which was used to measure the quantum yield for $CH_3C(O)$ from acetone photolysis, through measurement of $CH_3C(O)O_2$. Acetone is the most abundant oxygenated organic gas in the troposphere and its photolysis can account for up to 1/3 of radical production in the upper troposphere. The results from this chapter demonstrate that the I-CIMS can be used for acetone photolysis measurements under conditions of the troposphere.

In Chapter 3, the I-CIMS measurements of the $CH_3C(O)$ quantum yield in acetone photolysis are expanded to temperatures (223 to 323 K) and pressures (150 to 850 mbar) reflecting the conditions of the troposphere. The measurements are used to parameterize the quantum yield of $CH_3C(O)$ for use in models of tropospheric radical production. The parameterization shows that acetone photolysis near the tropopause may be up to 1.4 times slower than previously expected. These are the only measurements of acetone photolysis under tropospheric conditions based on the detection of the dominant radical product, $CH_3C(O)O_2$.

Chapter 4 explores a new, multiple-reagent ion system with Cl_2^- as the primary reagent ion (Cl_2-CIMS). Cl_2-CIMS provides higher sensitivity for small acyl peroxy radicals than achieved with I-CIMS. However, the higher background of Cl_2-CIMS leads to higher limits of detection and the uncertainty on multiple reagent ion chemistries makes this system unsuitable for ambient measurements. Cl_2-CIMS could be further improved through larger changes to the instrument design than those discussed here, and other novel reagent ion chemistries may be accessible using the multi-step ionization mechanism that produces Cl_2^-.

Chemical ionization mass spectrometry is well-suited to fast, speciated measurements of radicals and is thus useful for measurements of complex photolysis mechanisms, like that of acetone in the troposphere. Further instrument development could improve CIMS sensitivities and limits of detection to organic radicals, expanding its utility to more photochemical systems and ambient measurements of radicals as well.

ACKNOWLEDGEMENTS

Thank you to the coauthors of the papers that make up the bulk of this dissertation: to Dr. A.R. Ravishankara and Dr. Delphine K. Farmer for advising my research and striving to mold me into a better scientist, to Dr. Michael F. Link for mentoring my use of chemical ionization mass spectrometry and advising method development, to Soojin Lee for aiding in completion of many of the temperature-dependent photolysis experiments and running chemical box models. My work would have undoubtedly been impossible without all these contributions. Thank you as well to Dr. M.J. Riches for including some of my other work in a publication on wildfire smoke's impact on pine tree photosynthesis, which will not otherwise be discussed here.

Thank you to those who provided equipment and services integral to the completion of my research. Dr. James R. Neilson provided the Ocean Optics spectrometer used for photolysis measurements. Dr. Frank Flocke provided the peroxyacetyl nitrate source required to calibrate the acetyl peroxy radical. Dr. Russell Perkins provided the liquid cooling and heating units used for temperature control measurements. A special thank you to Tom Frederick for repeated maintenance of the KiloArc light source without aid from the manufacturer. Without his help, many of these measurements would not have happened.

Thank you to the members of the Farmer research group. It is an honor to have worked with such wonderful scientists during my time at Colorado State University.

Finally, thank you to my family for all the love and support they provided over the last 5 and a half years. Thank you to my wife, Calli, son, Beckham, and our dog, Nico, for providing a warm welcome home each night, without fail, and pushing me to better myself every day.

TABLE OF CONTENTS

CHAPTER 1: INTRODUCTION

In Earth's atmosphere, oxidation by free radicals is the primary means of removal of trace gases.[1] Our understanding of air pollution and global climate change depends on trace gas identities, concentrations, and lifetimes.[2] These qualities depend, in turn, on the availability of radicals and the rates and mechanisms of oxidation reactions that alter the trace gases composition of the atmosphere or lead to their removal from the atmosphere entirely.[3]

The primary source of radicals in the Earth's troposphere is the reaction of $O(^1D)$, from the photolysis of ozone (O_3), with water.

$$O_3 + h\nu \rightarrow O(^1D) + O_2$$

$$O(^1D) + H_2O \rightarrow 2OH$$

The hydroxyl radicals (OH) formed from this process oxidize trace gases, with OH lifetimes being much less than one second.[4] In subsequent reactions, the products of trace gas oxidation often recycle radicals and O_3, creating the oxidation cycles that clean Earth's atmosphere.[5]

Below the planetary boundary layer and, specifically, in polluted continental regions, modeling of radical production can be difficult due to the complexity of radical sources and sinks for the many natural and anthropogenic sources of trace gases.[6–8] However, these regions account for little of the total volume of the troposphere.

It was thought that radical production in the relatively clean free troposphere could be modeled through the $O(^1D) + H_2O$ mechanism alone. When measurements of OH concentrations in the free troposphere became possible, it was quickly found that the $O(^1D) + H_2O$ mechanism alone underpredicted radical production.[9] This discrepancy was largely due to missing radical production from the photolysis of organic trace gases.

Photolysis of organic gases leads to radical production without the initial consumption of a radical. The addition of aldehyde, peroxide, and ketone photolysis to models of tropospheric improved agreement to measurements, but uncertainties and persistent underprediction of upper tropospheric radical production remain.[10] The uncertainties are partly related to difficulties in measuring photolysis rates of the trace gases that impact radical production throughout the troposphere. Organic peroxy and hydroperoxy radicals (RO_2 and HO_2) are often the most immediate products of trace gas photolysis in the troposphere.[3] These radicals are difficult to measure due to their short lifetimes, requiring fast measurement techniques and minimal production even in laboratory experiments to avoid secondary chemistry.[11] Their visible and UV absorption spectra are largely unstructured and overlap, making quantification by spectroscopic methods rather difficult.[12] The remainder of this dissertation will describe advancements in the use of chemical ionization mass spectrometers for accurate, fast measurement of RO_2 with the specific goal of improving our understanding of acetone and other ketone photolysis throughout the troposphere.

Acetone is one of the most abundant oxygenated organic trace gases in the troposphere[13,14] and one of the most photochemically studied oxygenated organic molecules.[15] When measurements of OH identified underestimation of radical concentrations throughout the free troposphere, acetone photolysis was suggested to possibly account for most observed discrepancies.[16] More recent models suggest acetone photolysis is less important than initial estimates but may still equal $O(^1D) + H_2O$ production rates in the upper troposphere when water vapor mixing ratios are ~100 ppm or lower.[17,18]

Acetone photolysis in the troposphere occurs through a Norrish type I mechanism, forming one acetyl radical ($CH_3C(O)$) and one methyl radical (CH_3).[19]

$$CH_3C(O)CH_3 + h\nu \rightarrow CH_3C(O)CH_3^*$$

$$CH_3C(O)CH_3^* \rightarrow CH_3C(O) + CH_3;\ \lambda \leq 338\ \text{nm}$$

As with other organic radicals in the troposphere, these quickly add oxygen to produce an acetyl peroxy radical ($CH_3C(O)O_2$) and a methyl peroxy radical (CH_3O_2), and production of OH and HO_2 ensues from the further reactions of these RO_2.

$$CH_3C(O) + O_2 \xrightarrow{+M} CH_3C(O)O_2$$

$$CH_3 + O_2 \xrightarrow{+M} CH_3O_2$$

The primary fate of these peroxy radicals is loss to reaction with NO or themselves. $CH_3C(O)O_2$ may react with NO_2, when present, to form peroxyacetyl nitrate (PAN), a radical reservoir species.[20] In the cold upper troposphere, the lifetime of PAN against thermal decomposition is long, allowing for long-range transport of PAN formed from acetone photolysis.[21]

Despite the extensive study of acetone photolysis, uncertainties remain in both the acetone photolysis rates and mechanism under conditions of the troposphere. The current photolysis quantum yield recommendations include secondary decomposition of $CH_3C(O)$, which is temperature-dependent.[22]

$$CH_3C(O)^* \xrightarrow{+M} CH_3 + C(O)$$

Later studies found that this secondary decomposition component may not occur at wavelengths greater than 280 nm available in the troposphere.[23] Further uncertainties exist for acetone photolysis, including the impacts of tropospheric conditions, such as temperature and the presence of water.[24] Literature quantum yields disagree for wavelengths approaching the acetone photolysis threshold of 338 nm, where the available actinic flux is the largest, but acetone absorption cross sections are small.[25]

Many of these uncertainties may be addressed through methods that can directly measure the short-lived radical products of acetone photolysis in the troposphere, but this was largely unavailable in past studies. Instead, many studies measured stable end products of acetone photolysis. CO is a frequent tracer for acetone photolysis, formed through the eventual decomposition of $CH_3C(O)$,[26–29] as well as a pathway that produces CO and C_2H_6.[23,30] As CO is at best a minor product of acetone photolysis in the presence of O_2, measurements of CO were largely performed without O_2. Thus, these measurements are unable to fully reveal how acetone photolyzes in the troposphere. Other stable product analyses, such as measurements of biacetyl formed through combination of two $CH_3C(O)$[29] or production of CH_4 and C_2H_6,[31] have the same issues; as do more extensive methods that rely on introduced secondary reactions with $CH_3C(O)$, such as the reaction of Br_2 and $CH_3C(O)$ used by Khamaganov et al.[32,33] Some measurements of $CH_3C(O)$ and CH_3 in the absence of O_2 are available as well.[34,35] In the presence of O_2, CO_2 becomes a major end-product of acetone photolysis, which some studies have measured.[26,36,37] Studies have also looked at the loss of acetone.[36,38,39] Neither analysis provides detailed information on the initial products, and both are subject to the possibility of unintended secondary chemistry, as with the methods that could not measure with O_2. For immediate product quantum yields, studies have measured PAN production by introducing NO_2 to the reaction mixture.[40] This method can produce quantum yields for $CH_3C(O)$ (Φ_{CH3CO}) under tropospheric conditions and even provide information on other products from larger ketones, like MEK. However, secondary chemistry is also a concern in these systems,[41] as is the ability to properly transfer thermally unstable PAN from the reaction chambers and through gas chromatographs for analysis.[40] In situ measurements of PAN using Fourier Transform IR spectroscopy are possible.[42]

The current recommended quantum yields from Blitz et al.[22,43] also do not use measurements of a primary radical product from acetone photolysis. Φ_{CH3CO} from Blitz et al.[22,43] were measured through the production of OH (using laser-induced fluorescence) formed in the reaction of $CH_3C(O)$ with O_2.[44–46] The primary process in acetone photolysis in the troposphere is the production of $CH_3C(O)O_2$, and the channel that produces OH is minor under tropospheric pressures (much less than 10% at the tropopause). Blitz et al.[22,43] measured Φ_{CH3CO} primarily in He to enhance OH yields with little O_2 and at pressures at or below those of the troposphere. Their tropospheric quantum yields are obtained by fitting and extrapolating their data. Questions remain about this parameterization. These questions may be answered through the measurement of Φ_{CH3CO} in air and pressures relevant to the whole troposphere.

Chemical ionization mass spectrometry (CIMS) is an analytical technique that could be used to evaluate acetone photolysis under tropospheric conditions. It is based on the ionization of analytes through reaction with reagent ions.[47] Following ionization, these analytes can be separated and identified based on their masses. Modern CIMS instruments provide simultaneous detection of hundreds to thousands of analytes, with ppt-level limits of detection and time resolution at or below 1 Hz.[48,49] CIMS has seen widespread usage in ambient atmospheric sampling. There are many examples of CIMS used to measure radicals in the atmosphere, including OH,[50,51] HO_2,[52,53] and RO_2.[54–56] However, attempts to use current CIMS instrumentation for the measurement of photolysis quantum yields are limited.

Link et al.[57] first presented the use of a commercial atmospheric pressure interface chemical ionization mass spectrometer with iodide reagent ions (I-CIMS) for measurement of acyl radical quantum yields from methyl ethyl ketone (MEK) and biacetyl under tropospheric

conditions with acyl radical yields in acetone photolysis as a reference. The I-CIMS detected acyl peroxy radicals ($RC(O)O_2$) through clustering reactions with I^- reagent ions.

$$I^- + RC(O)O_2 \xrightarrow{+M} I(RC(O)O_2)^-$$

Production of $RC(O)O_2$ could be assumed to be equal to production of stable RC(O) during ketone photolysis. Experiments were carried out using 254 nm excitation in synthetic air and pressures from 90 to 840 mbar. Quantum yields were calculated through actinometry by comparing the production of $I(RC(O)O_2)^-$ to $I(CH_3C(O)O_2)^-$ signal produced from acetone photolysis under the same conditions. The acetone photolysis mechanism is simpler at this higher excitation energy than at the energies available in the troposphere, and the quantum yields change little with wavelength close to 254 nm[29,58,59] and are independent of temperature.[33] Using these concepts 254 nm reference quantum yields for $CH_3C(O)$ could be used from the data of Rajakumar et al.[35] at 248 nm.

The results of the Link et al.[57] study showed quantum yields for MEK and biacetyl in agreement with the limited prior literature on these two ketones.[35,41] The implications of these agreements were critical. These were the only quantum yields generated from measurements of the immediate radical products of MEK and biacetyl photolysis in the troposphere: $CH_3C(O)O_2$ for biacetyl and $CH_3C(O)O_2$ and the propionyl peroxy radical ($C_2H_5C(O)O_2$) for MEK. $CH_3C(O)O_2$ and $C_2H_5C(O)O_2$ from MEK photolysis were measured simultaneously at different mass-to-charge ratios, providing no interference between the radical signals. The I^- cluster ions formed also allowed simple differentiation of radical signals from background in these clean laboratory experiments. As a result, the I-CIMS method was able to generate more information on MEK photolysis than prior literature. This article demonstrated the utility of current CIMS instruments for measurements of radical quantum yields in complex photochemical systems.

The use of I^- to detect $CH_3C(O)O_2$ is established. The detection sensitivity is on the order of 1 ppt at atmospheric pressures, which translates to roughly 2.5 x 10^7 radicals per cm^3. Other reagent ions detect organic peroxy radicals as well, including CH_3O_2.[56] To optimize CIMS for measurements of ketone quantum yields, alternative reagent ion systems must be investigated.

This dissertation discusses further advancement of CIMS for radical quantum yield measurements in the photolysis of atmospheric trace gases. The focus of this work was first to develop methods for measuring $CH_3C(O)O_2$ and then to determine the quantum yields in acetone and other ketone photolysis under tropospheric conditions. Additionally, we explored an alternative CIMS reagent ion, Cl_2^-, to measure $CH_3C(O)O_2$. The results of these studies are presented in three chapters:

Chapter 2: The Quantum Yields for Thermalized $CH_3C(O)$ from Acetone Photodissociation as a Function of Wavelength and Pressure.

Chapter 3: The Quantum Yields for $CH_3C(O)$ in Acetone Photolysis as a Function of Temperature, Pressure, and Wavelength.

Chapter 4: Cl_2^- Chemical Ionization Mass Spectrometry (Cl_2-CIMS) for Measurement of Acyl Peroxy Radicals.

Together, these chapters will demonstrate the importance of CIMS as a technique for better measurements of trace gas photolysis, lowering uncertainty in models of tropospheric radical production. Chapter 5 summarizes the findings of this work and briefly describes the potential for new work suggested by our studies.

CHAPTER 2: THE QUANTUM YIELDS FOR THERMALIZED $CH_3C(O)$ FROM ACETONE PHOTODISSOCIATION AS A FUNCTION OF WAVELENGTH AND PRESSURE

2.1 Abstract

Acetone photolysis is a key source of HO_x (= HO + HO_2) and PAN in the upper troposphere. However, radical product quantum yield studies of acetone photolysis under tropospheric conditions are limited, due to difficulties in measuring the produced radicals. We used a chemical ionization mass spectrometer with iodide reagent ions, coupled to a photolysis reactor and a continuous-wave light source. We measured room temperature quantum yields for $CH_3C(O)$ in acetone photolysis by detecting $CH_3C(O)O_2$. We provide quantum yields for $CH_3C(O)$ from acetone photolysis as a function of wavelength and pressure relevant to the troposphere and compare our data to prior literature data for acetone photolysis. Observed quenching rate coefficients for air were the largest near 306 nm, the approximate dissociation barrier on the first excited triplet energy surface of acetone. We observed minimal influence of pressure on $CH_3C(O)$ quantum yields for 280 to 295 nm and above 320 nm. The quantum yields stopped decreasing as the wavelength increased beyond 320 nm.

2.2 Introduction

Acetone is a ubiquitous volatile organic compound (VOC) in Earth's troposphere.[13] It is emitted by anthropogenic and natural processes[60,61] and produced during the photooxidation of other VOCs.[62] Photolysis of acetone is expected to be an important source of OH and HO_2 (HO_x) to the upper troposphere. There are contradictory indications of the importance of this HO_x source.[16,18] One reason for the contradictions is that acetone photolysis quantum yields (denoted

by the symbol Φ in this chapter) under UT conditions are limited to few studies with no direct measurements of the yields of primary radical products, CH_3 and $CH_3C(O)$.

In the troposphere, where the available photolysis wavelengths are limited to >290 nm, two photolysis channels for decomposing acetone molecules are energetically possible.

$$CH_3C(O)CH_3 + h\nu \rightarrow CH_3C(O)CH_3^* \quad \text{R1}$$

$$CH_3C(O)CH_3^* + h\nu \rightarrow CH_3C(O) + CH_3;\ \lambda \leq 338\,nm \quad \text{R2a}$$

$$CH_3C(O)CH_3^* + h\nu \rightarrow\rightarrow CO + 2CH_3;\ \lambda \leq 299\,nm \quad \text{R2b}$$

where the 298 K thresholds for R2a and R2b are 338 and 298 nm, respectively. Reaction R2b is expected to be a stepwise process involving the dissociation of excited $CH_3C(O)$ from R2a.[58] The acetyl (CH_3CO) and methyl (CH_3) radicals quickly add oxygen to form acetyl peroxy ($CH_3C(O)O_2$) and methyl peroxy (CH_3O_2) radicals in the atmosphere.

$$CH_3C(O) + O_2 \xrightarrow{+M} CH_3C(O)O_2 \quad \text{R3a}$$

$$CH_3 + O_2 \xrightarrow{+M} CH_3O_2 \quad \text{R3b}$$

The peroxy radicals formed following acetone photolysis produce HO_x rapidly through atmospheric reactions. Atmospheric models suggest acetone photolysis in the upper troposphere, where H_2O abundance is low, is a HO_x source comparable to the primary $O(^1D) + H_2O$ source.[17,63] $CH_3C(O)O_2$ from acetone photolysis can also react with NO_2 to form peroxy acetyl nitrate (PAN),[20] a long-lived NOx and $CH_3C(O)O_2$ reservoir.

Though acetone photodissociation has been previously quantified,[22,23,29,36] uncertainties exist for both the total acetone dissociation quantum yields (Φ_{Ac}) and the quantum yields for products including $CH_3C(O)$ (Φ_{CH_3CO}), CH_3 (Φ_{CH_3}), CO (Φ_{CO}), and other minor products under tropospheric conditions. Direct measurements of Φ_{CH_3CO} and Φ_{CH_3} at wavelength > 280 nm are unavailable. The current NASA/JPL recommendation for radical quantum yields as a function of

temperature and pressure from acetone photolysis[64] are based on Φ_{CH_3CO} measured by Blitz et al.[22,43] and pressure-independent Φ_{CO} estimated by Gandini and Hackett[29] and Horowitz.[28] Blitz et al.[22,43] did not measure $CH_3C(O)$ directly. Instead, they detected OH radicals formed as a minor channel in the $CH_3C(O)$ reaction with O_2. Blitz et al.[46] measured the OH yields from $CH_3C(O)$ + O_2 as a function of pressure and assumed this was unimpacted by changes in acetone excitation energy. In addition, Φ_{CO} has been measured in the absence of O_2, a molecule that is expected to control the fates of both electronically excited acetone and the radicals formed from acetone photolysis under tropospheric conditions. Studies after those of Blitz et al. have found evidence for pressure dependence of Φ_{CO} at wavelengths around 248-266 nm.[26,33,35] Other studies of acetone photolysis under tropospheric conditions relied on measurements of acetone loss[24,36,38] production of stable products,[26,36,40,65] or indirect detection of the radicals (in the absence of O_2).[32] It is important to note that O_2 in the atmosphere can play the dual role of reacting with electronically excited acetone and converting the product radicals to peroxy radicals.

The difficulty in measuring acetone photolysis quantum yields has also led to ambiguity in acetone photo-physics at excitations > 290 nm. Absorption of a photon in this wavelength range results in the electronic excitation of an acetone molecule from the singlet ground state ($^1S_0$) to the first excited singlet ($^1S_1$).[15] The barrier height for acetone dissociation on the $^1S_1$ surface is not well established but is thought to be above the photon energies available in the troposphere. Instead, dissociation is expected to occur primarily after intersystem crossing (ISC) to the first excited triplet energy surface (T_1),[34] over a barrier located ca. 306 nm (391 kJ/mol) above the $^1S_0$ ground vibration level.[39] Dissociation from highly vibrationally excited S_0 states ($^1S_{0,v}$) following internal conversion (IC) from $^1S_1$ (or ISC from T_1) is also possible.

A recent master equation model for acetone photo dissociation developed by Barker[25] found dissociation following ISC to best describe the acetone photolysis quantum yields. This model showed that the thermalization of acetone in the T_1 state should yield a nearly constant dissociation quantum yield over the ca. 330 to 338 nm wavelength range. This feature in the quantum yield variation with wavelength was not observed by Blitz et al.[22] Gierczak et al.[36] did observe hints of this feature when measuring total acetone dissociation through the production of CO_2 (Φ_{Ac}) at 337 nm. Similar evidence can be found (though limited) in the data of Emrich and Warneck,[40] who relied on GC measurements of PAN following $CH_3C(O)O_2$ reaction with NO_2. It is possible that Φ_{Ac} does not approach zero until the 338 nm photolysis threshold.

The above description shows that further measurements of primary radical products of acetone photolysis under tropospheric conditions are needed to obtain accurate quantum yields. Such data would also help elucidate acetone photo-physics. Chemical ionization mass spectrometry (CIMS) is an analytical technique suitable for selective and sensitive measurements of organic peroxyl radicals[54,66,67] and HO_2[52,53,55] in the gas phase. This technique provides high detection sensitivity (ppt range) for $CH_3C(O)O_2$ and has minimal interferences.[68–70] We recently demonstrated the application of CIMS equipped with iodide reagent ions (I-CIMS) for the detection of $CH_3C(O)O_2$ and $C_2H_5C(O)O_2$ produced from photolysis of acetone, methyl ethyl ketone, and diacetyl.[57] The I-CIMS detected these radicals as iodide adducts, which could be easily separated from background ions through high-resolution peak fitting. We also demonstrated using $CH_3C(O)O_2$ and $CH_3C(O)O_2$ as proxies Φ_{CH_3CO} and $\Phi_{C_2H_5CO}$ in methyl ethyl ketone photolysis at 254 nm, and measurements of Φ_{CH_3CO} for diacetyl, in agreement with the literature.[41,71]

Here, we describe using I-CIMS to measure Φ_{CH_3CO} in acetone photolysis, under relevant wavelengths and pressures for the troposphere. The I-CIMS measures $CH_3C(O)O_2$ as an indicator

of $CH_3C(O)$ production (R3a). We obtain Φ_{CH_3CO} by comparing $CH_3C(O)O_2$ production at wavelengths between 280 and 330 nm to production at a reference wavelength of 254 nm. Acetone photolysis at 254 nm was previously demonstrated as an actinometer for other ketones.[57] We provide Φ_{CH_3CO} data as a function of wavelength and pressure at 298 K and compare these values to prior studies. We also describe observations of non-zero Φ_{CH_3CO} at excitation wavelengths approaching the threshold for acetone photolysis.

2.3 Methods

An atmospheric pressure interface, chemical ionization mass spectrometer (high-resolution time-of-flight mass analyzer) with iodide reagent ions (I-CIMS; Aerodyne Research Inc., Billerica, MA) was coupled to a photoreactor with a constant gas flow at the pressure of interest. Light from a continuous-wave wide-band light source (a high-pressure 1000 W Xenon lamp) was dispersed by a monochromator to isolate selected wavelengths. $CH_3C(O)$ was converted to $CH_3C(O)O_2$ formed from acetone photolysis. The I^- adduct of $CH_3C(O)O_2$ was quantified under tropospheric conditions of wavelength and pressure at ambient temperature (298 ± 2 K). A schematic diagram of the apparatus is shown in Figure 2.i.

2.3.1 Measurement of $CH_3C(O)O_2$ in acetone photolysis

In a photolysis flow reactor, mixtures of acetone in air (or N_2 with a small amount of O_2) were exposed to light of selected wavelengths between 254 and 335 nm. The I-CIMS sampled post-photolysis analyte mixtures, detecting $CH_3C(O)O_2$ as the iodide cluster, $I(CH_3C(O)O_2)^-$. We could not detect other photolysis and reaction products.

2.3.2 Photolysis measurement apparatus

The custom reactor (Figure 2.i) was a jacketed 1" O.D. Pyrex tube equipped with quartz windows to pass the photolysis light beam orthogonal to the direction of flow. The photolysis

volume in the reactor was roughly 0.3 cm^3, and the residence time within this volume was approximately 0.04 s. Mixtures of 1-10% acetone in ~1.3 bar N_2 were premade in 12 L glass bulbs. Flow from the acetone bulbs was mixed with ≥ 2 L/min flow of ultra zero air in ¼" PFA tubing long enough (~1 m) for the gases to mix before entering the reactor. The concentration of acetone in the reactor was calculated from the measured flow rates, pressure in the reactor, and the known acetone concentration in the mixture held in 12 L glass bulbs.

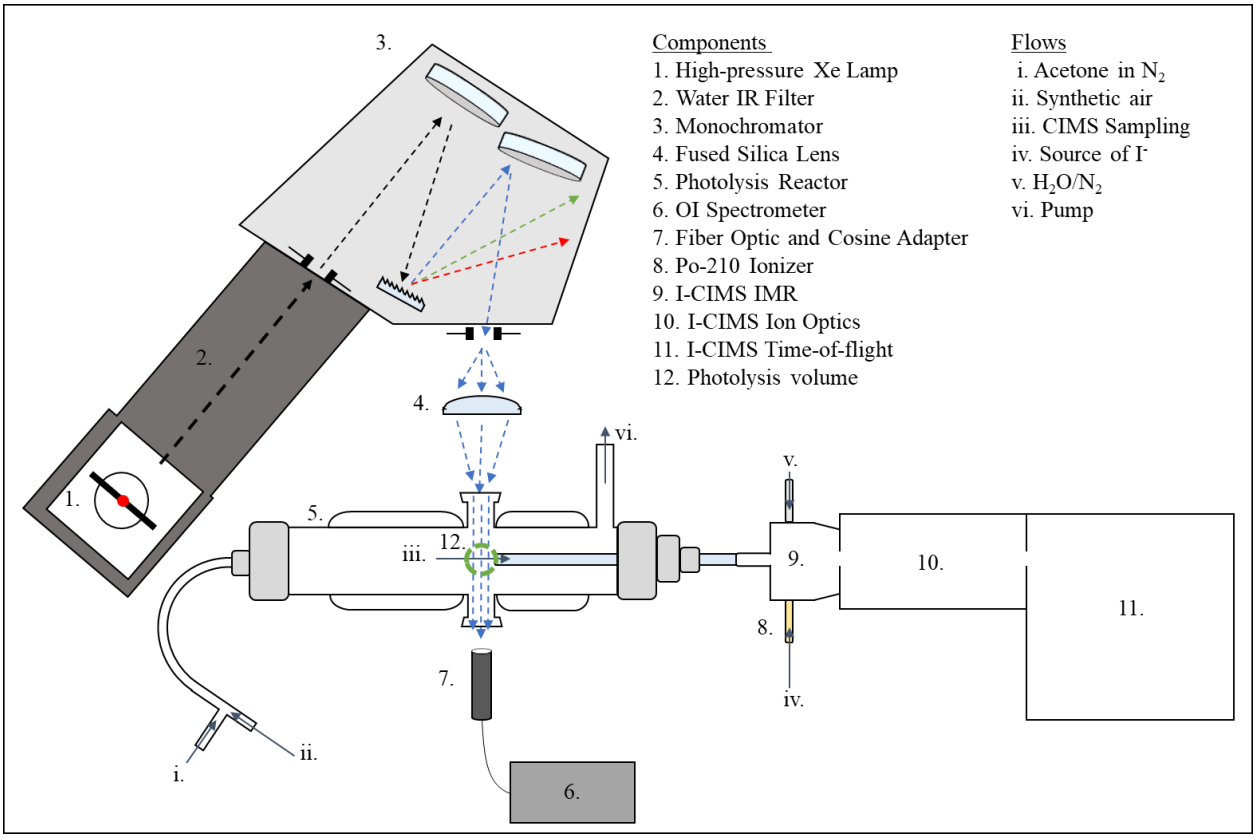

Figure 2.i Schematic of the apparatus used to measure Φ_{CH_3CO}. Standard numerals identify apparatus components, while Roman numerals denote gas flows. Dashed arrows show the path of light through the light source and reactor, and solid arrows show the gas flow direction.

A 1 kW high-pressure Xe lamp light source was coupled to an iHR320 monochromator (Horiba Instruments Inc.) for wavelength selection. A liquid-cooled water reservoir filtered out the IR wavelengths before the lamp output entered the monochromator. This component reduced the

heating of the monochromator from the 1 kW light source. The iHR320 selected photolysis wavelengths at a resolution of 3.7 nm (FWHM) for 1 mm entrance and exit slits. We also operated with 2 mm slit widths, as needed, to increase flux by approximately a factor of four. The resolution decreased to 5 nm when 2 mm slits were used. An anti-reflection coated, fused silica lens (ThorLabs Inc.) was used to focus the output beam and pass it through the photolysis reactor.

An HR2000-CG-UV-NIR spectrometer (OI spectrometer; Ocean Insight) measured the wavelength and intensity of light exiting the reactor (See figure 2.i) through a fiber optic cable and cosine adapter. We calibrated the OI spectrometer's spectral response as a function of wavelength in the UV using an SL-3 deuterium lamp (StellarNet Inc.). The SL-3 spectral output was calibrated to a NIST-traceable standard by StellarNet. The wavelength scale of the Ocean Insight spectrometer was calibrated using Hg lines from a Pen-Ray lamp (Analytik Jena).

Our Φ_{CH_3CO} experiments required monitoring the relative light source intensities (at 254 nm and the wavelength of interest), not the actual intensity. The OI spectrometer provided relative intensities using the intensity response function and wavelength scale calibrations described above. A more detailed description of OI spectrometer calibration and data usage for Φ_{CH_3CO} experiments are provided in Appendix A.2. The wavelength from the OI spectrometer agreed to ± 1 nm with that read out by the monochromator. The measured wavelength varied by 0.25 nm on average between 1- and 2-mm slits (tested at 320 nm). The wavelength precision at each slit width was between 0.2 and 0.3 nm (1σ) for most wavelengths. The measured photolysis wavelength was used to calculate Φ_{CH_3CO}, as described in Appendix A.2, and is reported for every Φ_{CH_3CO} experiment in Appendix B. For simplicity, Φ_{CH_3CO} throughout this chapter are described using the wavelength selected on the monochromator software unless otherwise stated.

2.3.3 I-CIMS measurement of $CH_3C(O)O_2$

The I-CIMS sampled the post-photolysis content of the reaction via a ¼" O.D. glass tube at the center of the photolysis reactor and approximately 0.5 cm downstream of the photolysis region. The I-CIMS design is described in detail elsewhere.[49,72,73] In short, three sections make up the I-CIMS detection system used here: (a) an ion-molecule reactor (IMR), where sampled analytes are ionized by reaction with iodide reagent ions; (b) an ion optics section, which transports and focuses ions from the IMR to the detector; and (c) a time-of-flight high resolution (≤ 3500 m/Δm) mass analyzer. We generated iodide reagent ions by flowing mixtures of CH_3I in N_2 through a Po-210 α-particle source and injected the I^- reagent ions into the IMR orthogonal to the sampling flow. A third IMR inlet allowed modulation of IMR H_2O pressure, by introducing H_2O-saturated N_2 flow. An RH-probe monitored H_2O vapor pressure. It is necessary to maintain a constant water vapor pressure in the IMR to keep the detection sensitivity constant. We operated the I-CIMS and IMR settings (P_{H_2O} = 0.8 mbar; P_{total} = 100 mbar) for optimal sensitivity to detect $CH_3C(O)O_2$.[57]

We detect $CH_3C(O)O_2$ in the I-CIMS as an iodide adduct ion, $I(CH_3C(O)O_2)^-$. The sensitivity of the I-CIMS to $CH_3C(O)O_2$ was 2.5 normalized (per million reagent ions) counts per second (ncps) per part per trillion. Background count rates for $I(CH_3C(O)O_2)^-$ were 20-30 ncps (1σ precision ± 8 ncps). We determined $CH_3C(O)O_2$ sensitivity by fully thermally dissociating known concentrations of PAN.[57,74] Further details on the PAN production method and associated materials are in Appendix A.3.

Under the O_2 concentrations used here, $CH_3C(O)$ formed from acetone photolysis is rapidly (<< 0.01 sec) converted to $CH_3C(O)O_2$ by reaction with O_2. This conversion time was on the order of microseconds in air and was < 0.02 s for 1 ppm of O_2. Measured signals of $I(CH_3C(O)O_2)^-$ correspond to $CH_3C(O)$ produced from acetone photolysis under conditions of our experiments

(R1-3b). The photodecomposition of acetone in the presence of O_2 also forms CH_3O_2, but we could not detect $I(CH_3O_2)^-$ in the I-CIMS mass spectra, as noted in Appendix A.4.

$$CH_3C(O)CH_3 + h\nu \rightarrow CH_3C(O) + CH_3 \quad \text{R1-2a}$$

$$CH_3C(O) + O_2 \xrightarrow{M} CH_3C(O)O_2 \quad \text{R3a}$$

$$CH_3C(O) + O_2 \rightarrow OH + products \quad \text{R3c}$$

$$CH_3C(O)O_2 + I^- \xrightarrow{M} I(CH_3C(O)O_2)^- \quad \text{R4a}$$

$$CH_3C(O)O_2 + I(H_2O)^- \rightarrow I(CH_3C(O)O_2)^- + H_2O \quad \text{R4b}$$

2.3.4 Materials

We degassed liquid acetone (≥99.5%; Sigma-Aldrich) in a storage flask at least three times by freezing in liquid N_2 and pumping out the headspace. The headspace of purified acetone liquid in the vacuum storage flask provided gaseous acetone for making the mixture in the bulb. We prepared mixtures of 1% to 10% acetone in N_2 in 12 L Pyrex bulbs, initially pressurized to 1300 mbar. We note that the room temperature vapor pressure of acetone is approximately 250 mbar, roughly a factor of two higher than the maximum pressure added to any glass bulb. The bulbs were passivated with a few mbar of acetone before making up the stock mixture. We measured acetone concentrations in the bulb via 254 nm absorbance before use in photolysis experiments. The absorbance measured concentrations agreed within 10% of that calculated from the measured pressures of acetone and N_2. (We note that we did not need an absolute concentration of acetone in the reactor to complete our measurements). Ultra-zero air (99.999% pure), pure O_2 (99.994%), 1% O_2 in N_2, and ultra-higher purity N_2 (99.999 were obtained from Airgas. As noted earlier, the flow rates of all gases were controlled by calibrated mass flow controllers and mixed before entering the reactor.

2.3.5 Measurements of Φ_{CH_3CO}

Acetone photolysis at 254 nm served as the reference for Φ_{CH_3CO} measurements. Acetone photolysis around 254 nm has been extensively studied, and the total dissociation quantum yields are near unity under all conditions.[22,33,34,75,76] Furthermore, this is close to 248 nm, where the pressure dependence of $CH_3C(O)$ formation has been studied.[35,76] We expect the change in this pressure dependence is minimal from 248 to 254 nm.[59] The $CH_3C(O)O_2$ signal from the photolysis at 254 nm and the desired wavelength was measured in steps while keeping acetone concentrations constant. The quantum yield at the wavelength of interest, λ, relative to 254 nm is given by E1.

$$\Phi_{CH_3CO,\lambda} = \Phi_{CH_3CO,254} \times \frac{I(CH_3C(O)O_2)^-_\lambda}{I(CH_3C(O)O_2)^-_{254}} \times \frac{\sigma_{254}}{\sigma_\lambda} \times \frac{F_{254}}{F_\lambda} \quad \text{E1}$$

where Φ_{CH_3CO} are the quantum yields for $CH_3C(O)$, σ are the absorption cross sections at the photolysis wavelengths, F are photon fluxes, and $I(CH_3C(O)O_2)^-$ are signals at λ and 254 nm. The relative photon flux at wavelengths λ and 254 nm, F_{254}/F_λ, was measured by the OI spectrometer as the photolysis light exited the reactor (Figure 2.i). We assumed that Φ_{CH_3CO} reported by Rajakumar et al.[35] as a function of pressure at 248 nm is valid for 254 nm. We also measured Φ_{CH_3CO} at 248 nm relative to 254 nm and found them to be the same within uncertainties. We used σ reported by Gierczak et al.[36] and modified it to account for the larger line width of our photolysis light, as explained in Appendix A.5.

During measurements of Φ_{CH_3CO}, acetone concentration, total flow rate, and pressure in the reactor were kept constant for 20 to 60 min. The monochromator was programmed to switch between 254 nm and the wavelength of interest five times, to obtain Φ_{CH_3CO}. The monochromator always scanned from high-to-low λ to reach 254 nm and always from low-to-high when transitioning to the target wavelength. This enabled precise reproducibility of wavelength and

avoided backlash of the monochromator. Note that the wavelength of the photolysis light source was always measured using the OI spectrometer. Between wavelength changes, the photolysis beam was blocked to measure the background signal and its uncertainty. Details on the experimental conditions for measuring Φ_{CH_3CO}, including number of repetitions, pressure, and effective wavelength are in Appendix B. A typical measurement sequence is shown in Figure 2.ii.

We measured Φ_{CH_3CO} at five pressures from 150 to 850 mbar (roughly the atmospheric pressure in Fort Collins, CO). A diaphragm pump (DOA-P704-AA; Gast Manufacturing Inc.), with pumping speed controlled by a manual needle valve, maintained a constant pressure in the reactor. The pressure in the reactor was measured using a calibrated MKS Baratron.

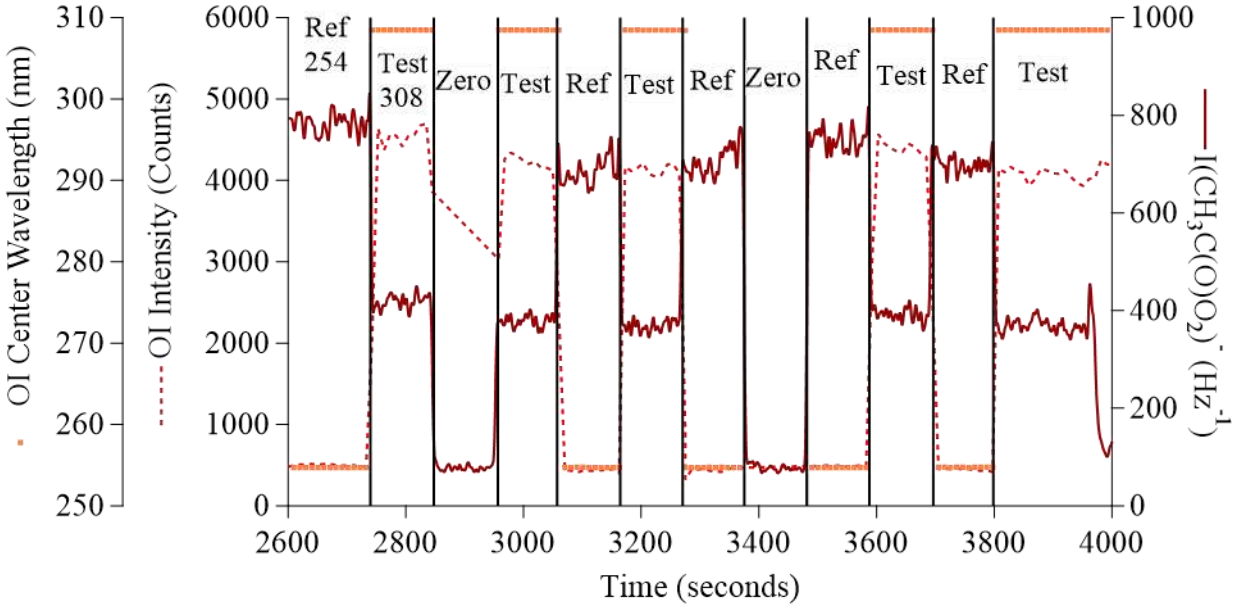

Figure 2.ii A typical time series for measuring Φ_{CH_3CO} (308 nm, 100 second steps) showing overlayed OI spectrometer and I-CIMS signals. The left-most axis shows the emission center wavelength as reported by the OI spectrometer (nm; orange dots). The next left axis shows the OI spectrometer reported intensity (counts; red dashed line). The right axis shows $I(CH_3C(O)O_2)^-$ signal intensity (Hz^{-1}; dark red line). Reference (ref), test, and background (zero) steps are labeled and separated by black vertical lines. Background-subtracted signal ratios from adjacent steps were used as described in E1 (Ref = 254; Test = λ) to calculate up to 5 replicates of Φ_{CH_3CO} for each measurement sequence. More than 300 measurement sequences were performed for this study.

2.4 Results and Discussion

We measured quantum yields for the formation of thermalized $CH_3C(O)$ radicals at various wavelengths between 254 nm and 330 nm, all relative to that at 254 nm. All our reported studies are at 298 ± 5 K. The pressures in the reactor ranged from ~850 mbar (approximate maximum ambient pressure in Fort Collins, CO) to 150 mbar at five pressures (850, 700, 500, 300, and 150 mbar); thus, it covered the tropospheric pressure range of interest. The upper-pressure limit was determined by the ambient pressure. The lower-pressure limit was constrained by the configuration of the CIMS detector and the need to maintain sufficient pressure in the ion-molecule reactor while keeping a reasonable bypass flow rate. (Reconfigurations of the CIMS instruments should allow exploring a wider range of pressures.)

We did not carry out actinometry to determine the photolysis light flux but measured the relative intensity of photolysis light as it exited the reactor using a calibrated spectrometer whose response was traceable to the NIST primary standard. As noted later, we could estimate the photolysis flux from the photon flux measured using a calibrated spectrometer at the exit of the reactor. Also, we generated known concentrations of the $CH_3C(O)O_2$ radicals from the thermal dissociation of PAN. Thus, the measured production of $CH_3C(O)O_2$ radicals at 254 nm (where the quantum yield is known) could be used to estimate the light flux. All these estimates agreed to within 10%. Lastly, some initial attempts were made by examining the loss of ClC(O)C(O)Cl due to photolysis as a measure of the photon flux. In principle, we did not need to know the absolute photon flux as we measured the relative quantum yields. We do not need the exact acetone concentration in the reactor, as it was constant, and the measurements were made relative to a reference wavelength. Further, the acetone concentrations in our stock mixture in 12 L bulbs were measured via UV absorption at 254 nm and the concentrations in the reactor could be calculated

from measured flow rates. Therefore, the uncertainties in photon flux, acetone concentration, and absolute UV cross-sections do not influence our measured values. We know the relative absorption cross sections of acetone and relative photon flux as a function of wavelength.

We conducted experiments and ran chemical models to ensure our Φ_{CH_3CO} measurements were not impacted by radical loss in the reactor or the unexpected effects of high acetone concentrations. The 0-D box model showed a detectable impact of radical-radical reactions at [$CH_3C(O)O_2$] > 300 ppt for 850 mbar, with a 5% loss of ($CH_3C(O)O_2$) at 500 ppt (Appendix A.1). In practice, $CH_3C(O)O_2$ loss was unmeasurable up to 400 ppt at 850 mbar for a total reactor flow rate of ca. 2150 mL/min. At 150 mbar, $CH_3C(O)O_2$ concentrations without significant radical-radical reaction loss extended above 400 ppt. All our quantum yield measurements were carried out with $CH_3C(O)O_2$ abundances below this level. Examples of linear $CH_3C(O)O_2$ response over these concentration ranges are provided in Appendix A.6. The radical signals at [$CH_3C(O)O_2$] > 500 ppt followed the same trend when varying acetone concentration and light intensity at 280, 290, and 300 nm, indicating radical-radical reaction loss as the cause of non-linear changes in $CH_3C(O)O_2$ at higher concentrations than those used for Φ_{CH_3CO} measurements. The attenuation of light in the reactor was negligible, with an upper limit of 1.5% loss for $\sigma_{280} = 4.91\times10^{-20}$ cm^2 and 3×10^{16} cm^{-3} of acetone. Measured absorption cross sections using the KiloArc for wavelengths between 280 and 325 nm agreed with reference data from Gierczak et al.[36] (Appendix A.5).

It has been shown that ground-state acetone can quench fluorescence from the excited state,[77] particularly at wavelengths approaching the photolysis threshold. Further, acetone can also prevent dissociation from excited states by rapidly quenching it. Therefore, we measure the yield of $CH_3C(O)O_2$ as a function of acetone concentration at 254 nm, 308, and 320 nm (Figure 2.iii). Acetone concentrations of up to 1.5×10^{16} cm^3 were used, but $CH_3C(O)O_2$ concentrations produced

by photolysis were maintained below 400 ppt to prevent any loss via self-reactions and reactions with CH_3O_2. The results are shown in Figure 2.iii and suggest that the 'self-quenching' by acetone is essentially negligible under the conditions of our experiments.

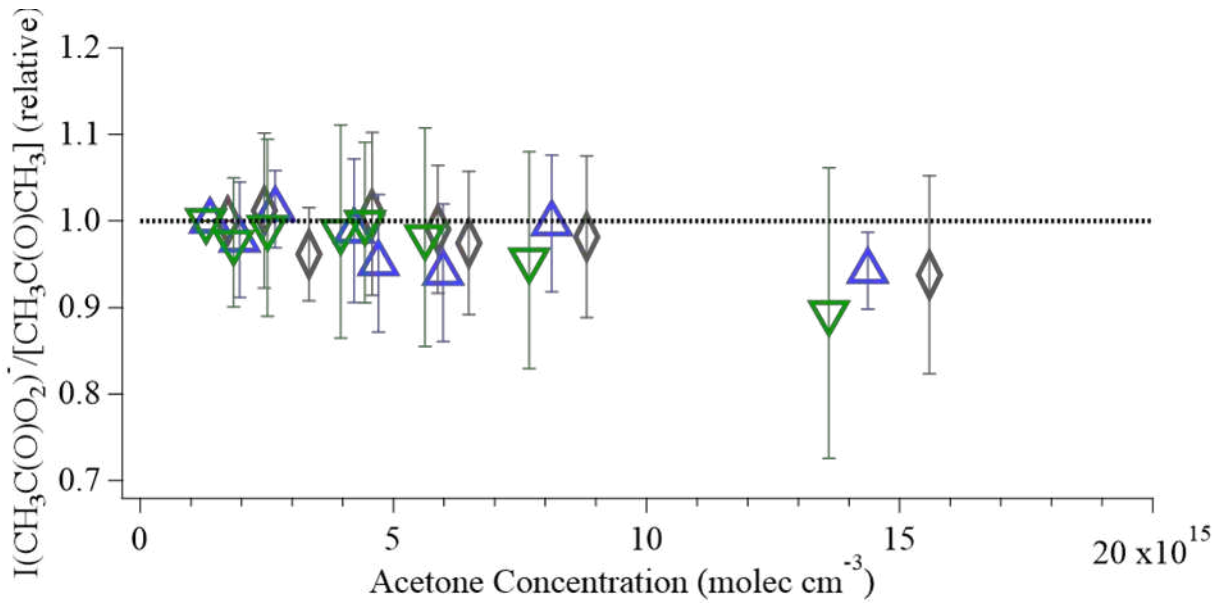

Figure 2.iii $I(CH_3C(O)O_2)^-$ signal normalized to acetone concentration at 254 (green triangles), 308 (blue triangles), and 320 nm (grey diamonds) for acetone concentrations up to 16 $\times 10^{15}$ cm^3. $I(CH_3C(O)O_2)^-$ signal was normalized to that obtained at 1 $\times 10^{15}$ cm^3 acetone. The dotted lines represent the expected $I(CH_3C(O)O_2)^-$ for negligible acetone quenching. Error bars are one standard deviation across 10 concentration change experiments.

The absorption cross-section of acetone at longer wavelengths of our study, 320 to 330 nm, drops off significantly. Therefore, we used wider slits (2 mm) to obtain higher photon flux at these wavelengths. Tests carried out with 1 mm and 2 mm slits showed that the results were essentially the same. The results of these tests are shown in Figure 2.iv. The potential differences in effective photolysis wavelength because of the change in spectral width of the photolysis light did not make a measurable difference.

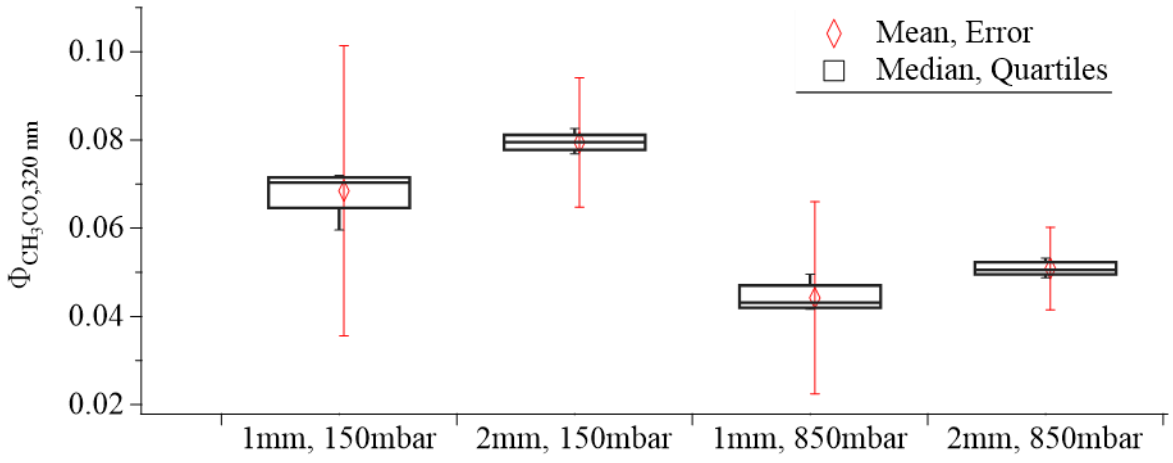

Figure 2.iv: $\Phi_{CH_3CO,320nm}$ measured at 850 and 150 mbar with 1 mm and 2 mm monochromator slits. Box plots show the median and 10th, 25th, 75th, and 90th percentiles for each experiment (5 trials). Red diamonds show the mean, with error bars showing 2σ experimental uncertainties (approximately 50% for 1 mm slits and 20% for 2 mm).

2.4.2 Influence of O_2 on $CH_3C(O)$ quantum yield

We examined the influence of O_2 on Φ_{CH_3CO}. First, O_2 can quench excited acetone at rates different than N_2. Second, O_2 can react with excited acetone to produce free radicals. We varied the abundance of O_2 between 1 ppm in N_2 to 100% O_2. 1 ppm of O_2 was sufficient to convert all $CH_3C(O)$ radicals to $CH_3C(O)O_2$ before entering the CIMS inlet. As shown in Figure 2.v, the measured Φ_{CH_3CO} were independent of O_2 abundance. This test showed that the quenching rates of excited acetone are essentially the same in N_2, O_2, and air. Further, this test showed that O_2 did not react with the excited acetone to produce $CH_3C(O)$ or $CH_3C(O)O_2$ radicals.

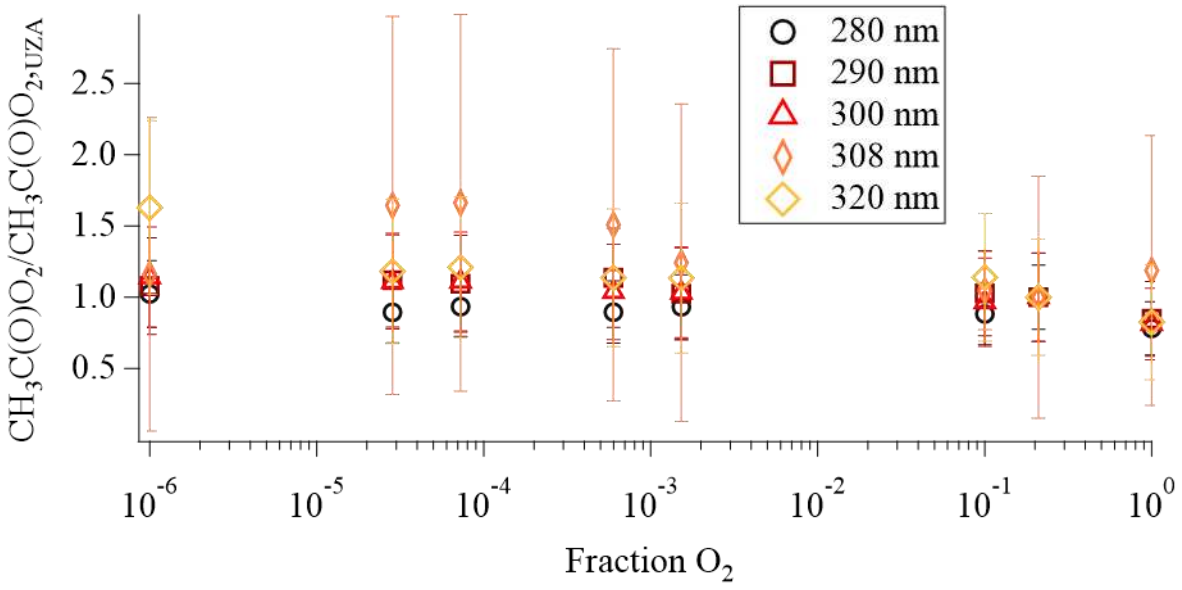

Figure 2.v Production of $CH_3C(O)O_2$ as a function of O_2 mixing ratio, relative to production in ultra-zero air, at 280 (black circles), 290 (dark-red squares), 300 (red triangles), 308 (orange diamonds), and 320 nm (yellow diamonds). Error bars represent 1σ signal uncertainties.

2.4.3 Φ_{CH_3CO} as a function of pressure

Using the production of $CH_3C(O)O_2$ at 254 nm as a reference, we measured Φ_{CH_3CO} at room temperature from 280 to 330 nm and pressures from 850 to 150 mbar. Figure 2.vi shows the averages of measured quantum yields as a function of the effective photolysis wavelengths. All the measured values are tabulated in Appendix B.

We obtained a 2σ experimental error of 28% for wavelengths ≤ 320 nm. This error was found through propagating the precision of our measurements (the I-CIMS and OI spectrometer signals) and the reported uncertainties in the values of σ_λ and $\Phi_{CH_3CO,254nm}$. Due to the much lower signal, uncertainty for 325 and 330 nm was 50%. The 2σ precision within the experiments was much smaller (9%). Repeat Φ_{CH_3CO} measurements at a given wavelength and pressure varied from the mean with an average standard deviation of 10%, though variations for some conditions were much larger as is visible in Figure 2.vi.

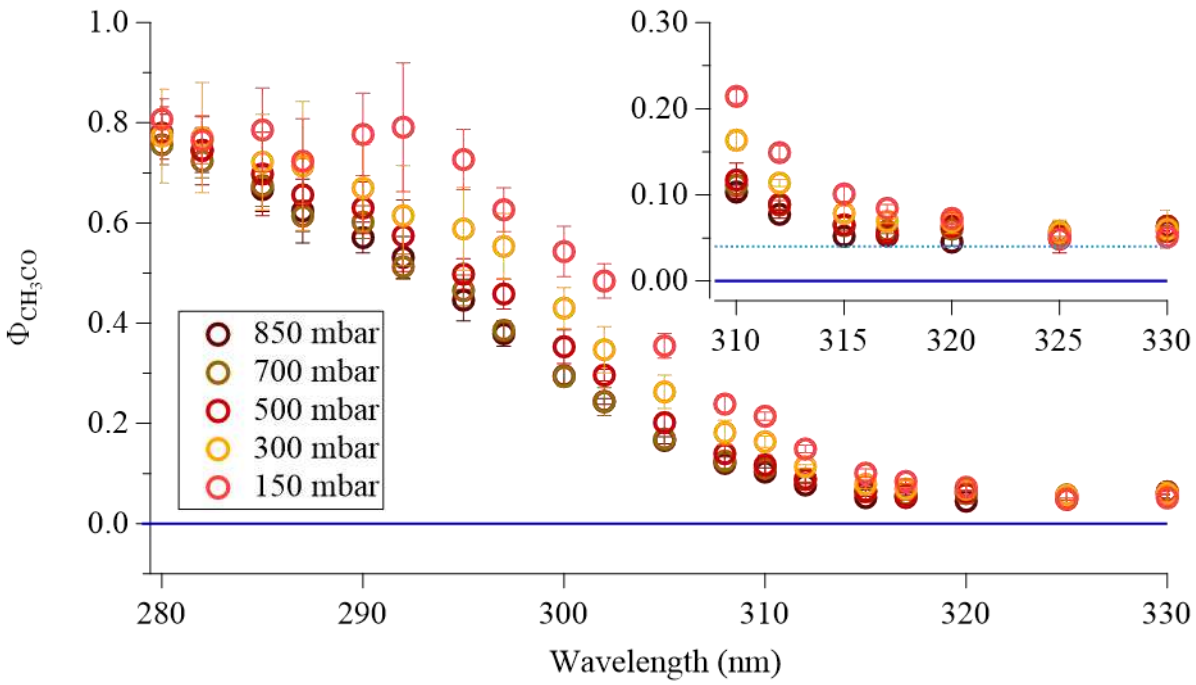

Figure 2.vi Φ_{CH_3CO} for thermalized $CH_3C(O)$ at wavelengths and pressures utilized in this study. Data points are an average of at least five replicates. Error bars are 1σ precision. Blue solid lines are used to denote 0. The inset graphic shows Φ_{CH_3CO} from 310 to 330 nm, where we observed Φ_{CH_3CO} of approximately 0.04 (denoted by the dashed light-blue line). This finding is contrary to some of the previously reported values.

At the shortest wavelength segment (280-292 nm), the change in Φ_{CH_3CO} with pressure was minimal, with an upper limit of approximately 0.8 for Φ_{CH_3CO}. At 150 mbar, Φ_{CH_3CO} in this wavelength region are nearly constant. In the center segment (295 – 315 nm), we observed decreases in Φ_{CH_3CO} as excitation wavelength increased at all pressures. We found that Φ_{CH_3CO} was finite at $\lambda > 315$ nm, reaching a minimum of 0.04. The small measured Φ_{CH_3CO} above 315 nm was essentially independent of pressure.

Φ_{CH_3CO} changes with pressure due to collisional quenching of electronically excited acetone. It could also increase with pressure by preventing the decomposition of vibrationally excited $CH_3C(O)$ formed in the photodissociation at wavelengths below 299 nm. We considered a

simplified system with two possible fates for acetone molecules following excitation at $\lambda \geq 300$ nm: dissociation to form $CH_3C(O)$ (R1) and collisional quenching by air molecules (R5).

$$CH_3C(O)CH_3^* + air \rightarrow CH_3C(O)CH_3 + air \quad \text{R5}$$

Φ_{CH_3CO} is determined as the ratio of the rate of dissociation (k_{diss}) divided by the total rate of dissociation and quenching by air (k_Q).

$$\Phi_{CH_3CO} = \frac{k_{diss}}{k_{diss} + k_Q[Air]} \quad \text{E2}$$

$$k_{Q1} = 0.79k_{Q,N_2} + 0.21k_{Q,O_2} \quad \text{E3}$$

We carried out Stern-Volmer analyses by plotting $1/\Phi_{CH_3CO}$ against the number density of the bath gas.

$$\frac{1}{\Phi_{CH_3CO}} = 1 + \frac{k_Q[Air]}{k_{diss}} \quad \text{E4}$$

We present Stern-Volmer analyses of the change in Φ_{CH_3CO} with air concentration in Figure 2.vii, Table 2.a, and Appendix A.7 Figure 2.vi. The slopes of the linear least squares regression lines represent k_Q/k_{diss}.

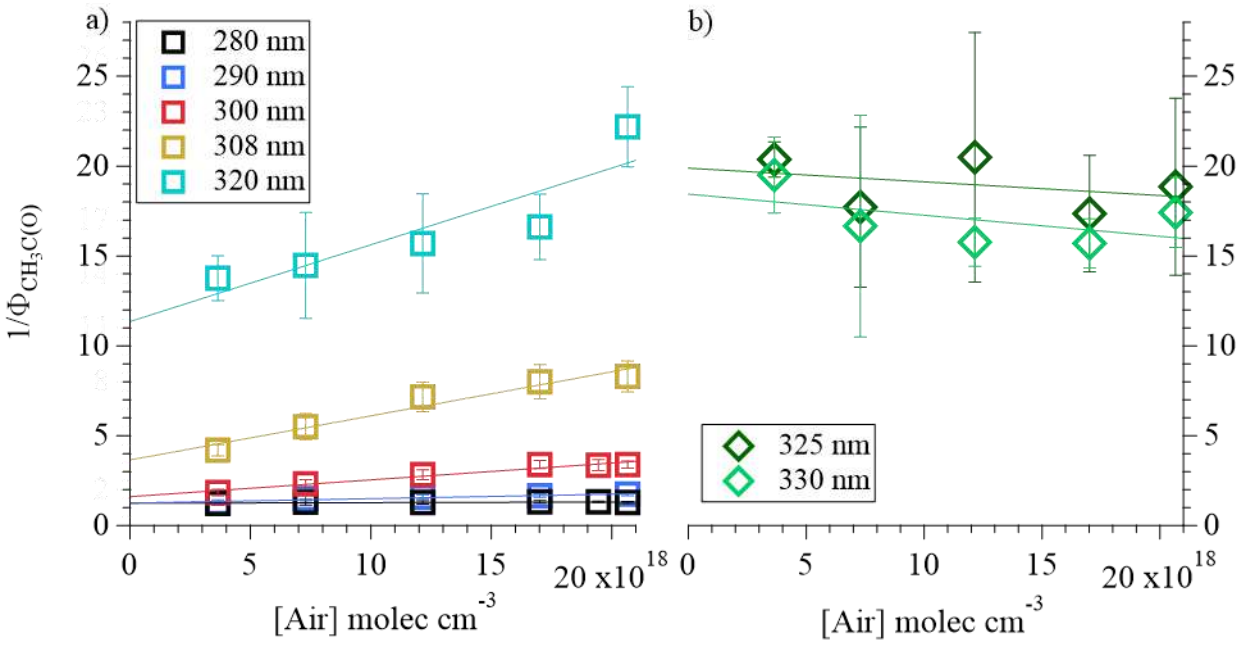

Figure 2.vii a) Example $1/\Phi_{CH_3CO}$ data showing Stern-Volmer relationships between Φ_{CH_3CO} and reactor pressure for 280 to 320 nm. b) $1/\Phi_{CH_3CO}$ data for 325 and 330 nm, showing no clear relationship between pressure and Φ_{CH_3CO}. Lines represent linear correlations to air molecule number density. Error bars represent 1σ standard deviation.

The impact of air pressure on quenching on Φ_{CH_3CO} shows an interesting pattern. The quantum yields at short wavelengths, 280 and 290 nm are weakly dependent on pressure suggesting rapid photodissociation of the excited acetone. When analyzed using a simple Stern-Volmer analysis applicable to a two-state system, the rate coefficient for quenching by N_2/O_2 is estimated to be $k_{Q1} < 1\times10^{-13}$ for 280 and 282 nm. These values were found by multiplying the slopes by the known k_{diss} (1.9×10^{7} s^{-1}) at 284 nm. Φ_{CH_3CO} from 280 to 320 nm show a "normal" behavior expected for quenching of electronically excited acetone before dissociation (decrease in quantum yield with increasing pressure). We observed increases in quenching as the excitation energy decreased. Specifically, this increase with wavelength appears greatest near the expected triplet photodissociation threshold of 306 nm, with a maximum slope at 315 nm. Slight non-linearity emerged in the Stern-Volmer fits for some wavelengths, specifically noticeable for 308

nm in Figure 2.vii; such behavior is to be expected given the complexity of the system involving more than one excited state. At wavelengths longer than 315 nm, k_Q decreased slightly and is near zero at $\lambda \geq 325$ nm.

Interestingly, Φ_{CH_3CO} at 325 and 330 nm are independent of pressure. These are the wavelengths where Φ_{CH_3CO} were expected to be essentially zero (very close to the thermodynamic threshold for dissociation). This near independence on pressure may indicate a different dissociation mechanism at these long wavelengths.

Table 2.a Stern-Volmer Fit Data for Quenching by Air

Wavelength nm	Slope 10^{-20} cm^3	σ_{Slope} $\pm 10^{-20}$ cm^3	R^2
280	0.3	0.2	0.52
282	0.4	0.2	0.58
285	1.3	0.3	0.91
287	1.6	0.3	0.91
290	2.5	0.4	0.94
292	3.6	0.9	0.83
295	5.0	0.7	0.94
297	6.6	0.6	0.98
300	9	1	0.96
302	12	2	0.94
305	20	2	0.96
308	25	3	0.94
310	30	7	0.93
312	34	6	0.93
315	49	8	0.93
317	39	10	0.82
320	43	13	0.79

2.4.4 Comparison with previous studies

Numerous studies have examined the quantum yields in the photodissociation of acetone as a function of pressure. The older studies focused on end-product analyses. Emrich and Warneck[40] converted the $CH_3C(O)$ radical to $CH_3C(O)O_2$ and then PAN, which was measured. Gierczak et al.[36] examined the loss of acetone and the formation of CO_2 and other products. Nàdasdi et al.[38] also measured acetone loss for 308 nm photolysis. Khamaganov et al.[32] were able to measure $CH_3C(O)$ in the absence of O_2 through reaction with Br_2 (using fluorescence of Br), but at limited relevant wavelengths (300 and 308 nm). Rajakumar et al. measured the quantum yield for $CH_3C(O)$ at 248 nm by detecting $CH_3C(O)$ via cavity ring-down spectroscopy. The most extensive studies are those of Blitz and colleagues[22,43] who used OH produced by the reaction of $CH_3C(O)$ radical with O_2 as a proxy for $CH_3C(O)$ radical.[22] Blitz et al.[22] included in their parameterization a secondary $CH_3C(O)$ decomposition channel (R2b). The inclusion of this channel was based on prior measurements of Gandini and Hackett,[75] who measured $CH_3C(O)$ recombination to form biacetyl ($CH_3C(O)C(O)CH_3$), and the CO and CH_4 yields measured by Horowitz.[28] We include here, again, the reactions that directly influence our measurements $\Phi_{\mathrm{CH_3CO}\cdot}$.

$$CH_3C(O)CH_3 + h\nu\ (\lambda > 290\ nm) \rightarrow CH_3C(O)CH_3^* \qquad \text{R1}$$

$$CH_3C(O)CH_3^* \rightarrow CH_3C(O) + CH_3 \qquad \text{R2a}$$

$$CH_3C(O) \rightarrow CO + CH_3 \qquad \text{R2b'}$$

$$CH_3C(O) + O_2 \xrightarrow{M} CH_3C(O)O_2 \qquad \text{R3a}$$

$$CH_3C(O) + O_2 \rightarrow OH + products \qquad \text{R3c}$$

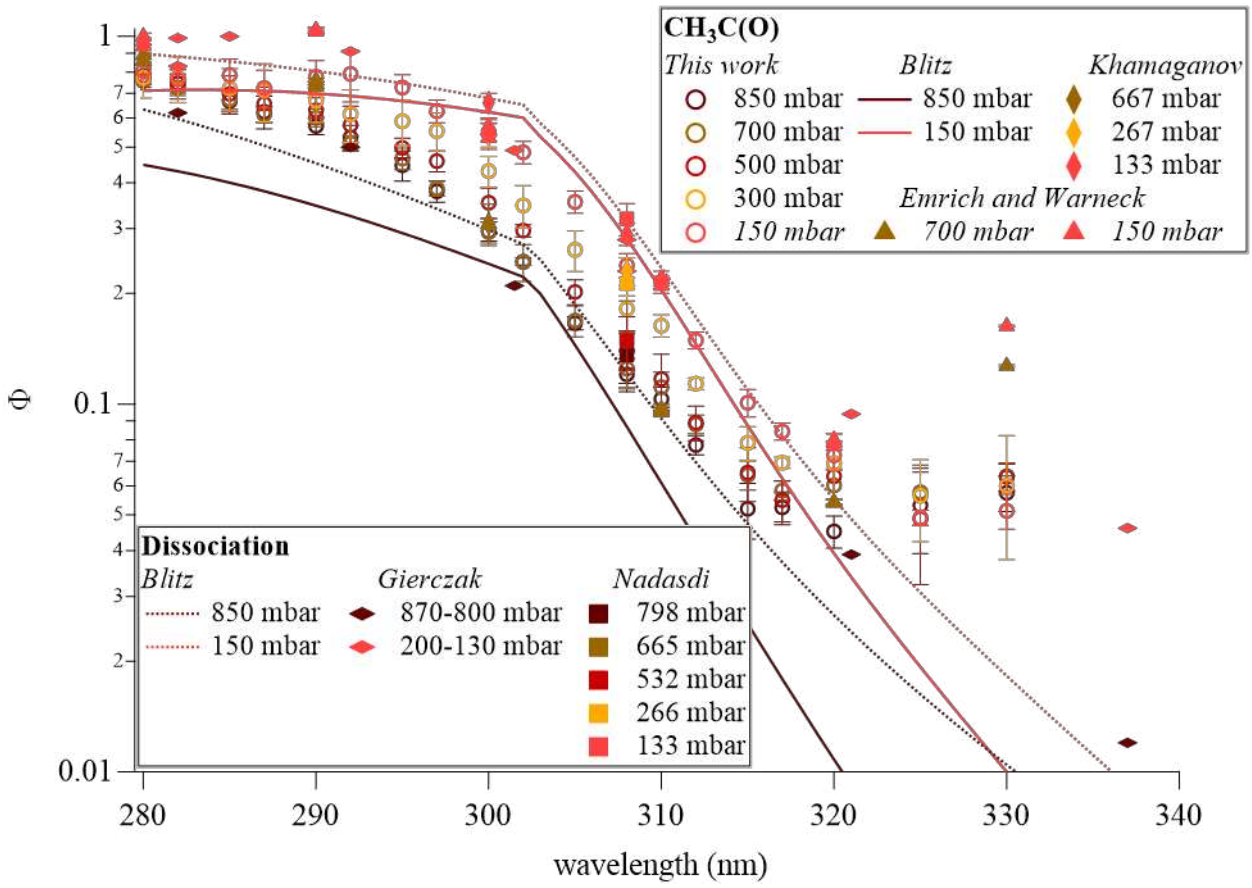

Figure 2.viii Comparison of acetone quantum yields to literature values. Comparison includes Φ_{CH_3CO} from this work (open circles), Emrich and Warneck[40] (triangles), Khamaganov et al.[32] (vertical diamonds), parameterized values from Blitz et al.[22] (solid lines), and quantum yields of acetone dissociation from Blitz et al.[22] parameterization (dotted lines), Gierczak et al.[36] (horizontal diamonds), Nàdasdi et al.[38] (squares). Error bars for experimental values represent measurement precisions.

Our measurements of Φ_{CH_3CO} represent only $CH_3C(O)$ that is stabilized by collisions after acetone photolysis and reacts with O_2 to form $CH_3C(O)O_2$. The $CH_3C(O) + O_2$ reaction can produce OH (R3c), rather than $CH_3C(O)O_2$. The branching ratio for R3c increases at lower pressures. The I-CIMS could not observe products of R3c. The yield of OH is minor (~10%) at 150 mbar.[1–3] Recent studies have shown this channel to contribute less than 4% at pressure and bath gases used in this study.[78] This branching ratio is not expected to be influenced by the nascent energy of $CH_3C(O)$ following photolysis at different wavelengths.[79] The amount of $CH_3C(O)$ lost

due to R3c did not influence our $CH_3C(O)O_2$ measurements even at lowest pressures of our study. In addition, R3c occurs to the same extent for the reference and test wavelengths of this study, insignificant influence on the measured Φ_{CH_3CO}. Further decomposition of $CH_3C(O)$ to CH_3 + CO would not be directly observed in our system. This process is included in the Blitz et al.[22] parameterization of acetone photolysis above 280 nm. Later studies concluded that CO production from $CH_3C(O)$ is unimportant.[23] There is the possibility for minor formation of CO + C_2H_6 at all wavelengths used here.[23] We could not detect either C_2H_6 or CO using the I-CIMS. We compare our data to literature values for Φ_{CH_3CO} and acetone dissociation quantum yields in Figure 2.viii.

Excitation energy up to and beyond the triplet photolysis barrier (~306 nm) largely explains Φ_{CH_3CO} and its pressure variation in the shortest (280 to 292 nm) and middle (295 to ~320 nm) wavelengths. Acetone molecules excited at wavelengths between 280 and 295 nm were not effectively quenched by air molecules even at the higher pressures of our study, leading to Φ_{CH_3CO} quantum yields that were largely independent of pressure. This observation suggests that k_{diss} at these wavelengths are very large compared to the quenching by air. The lack of dependence differs from some prior literature findings. Though Φ_{CH_3CO} at 150 mbar was larger than Φ_{CH_3CO} calculated from the Blitz et al.[22] parameterizations for this wavelength range, our 150 mbar Φ_{CH_3CO} are generally 20% lower than the unity quantum yield identified by Gierczak et al.[36] and Emrich and Warneck.[40] Though the contribution of CO formation from the secondary decomposition of $CH_3C(O)$ is expected to be minimal, some pressure-dependent loss of $CH_3C(O)$ would help explain this difference. The lower internal energies of acetone excited between 295 and 320 nm, are quenched below the dissociation threshold more easily by collision with air molecules. Over this wavelength range, our data is much closer to prior measurements.[22,32,36,38,40]

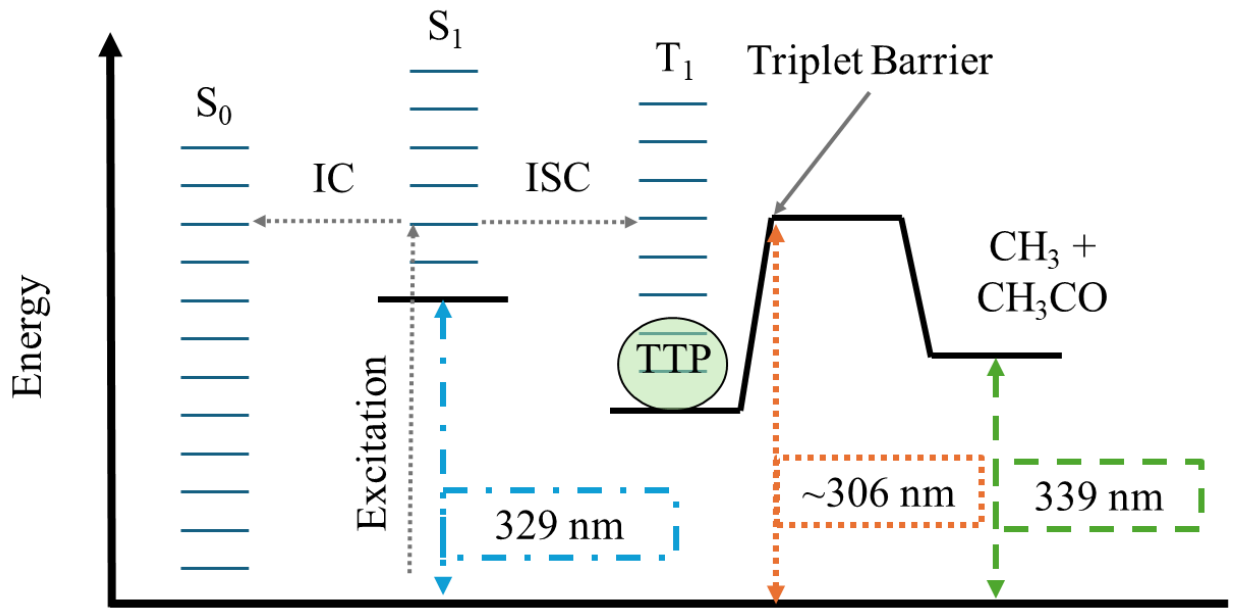

Figure 2.ix Energy diagram for acetone photoexcitation adapted from Barker.[25] Simplified S_0, S_1 and T_1 energy states are shown alongside the triplet barrier for dissociation in the CH_3 and $CH_3C(O)$. Dotted arrows denote photoexcitation, internal conversion (IC), and intersystem-crossing (ISC) transitions. Double arrows threshold wavelengths shown from the S_0 origin to the S_1 origin (blue), triplet photodissociation barrier (orange), and dissociation products (green). These energies were all taken from Barker.[25] The higher energy of the S_1 origin compared to the products suggests the potential for photolysis at all excitation wavelengths after IC to the low barrier S_0 state. The area highlighted in green and labeled 'TTP' provides a rough estimate of the T_1 energy level that contributes to non-zero Φ_{CH_3CO} >315 nm through thermalized triplet photolysis.

The quantum yields at wavelengths longer than 320 nm show clear evidence that Φ_{CH_3CO} does not decrease to zero as the wavelength approaches the photolysis threshold. This result agrees with the recent findings of Barker[25] based on a detailed examination of the individual processes involved in acetone photodissociation. According to the photophysics-based model,[25] wavelength-independent Φ_{CH_3CO} occurs at low excitation energies as the low energy triplet acetone is thermalized, leading to a consistent distribution of molecules on the triplet energy surface with sufficient energy to decompose, regardless of excitation energy. In our data, the onset of non-zero Φ_{CH_3CO} begins at slightly shorter wavelengths than those predicted by Barker. Though the experimental uncertainty at $\lambda > 320$ nm excitation is large, due to the low $I(CH_3C(O)O_2)^-$ signals,

we note that the Φ_{CH_3CO} asymptote is more than an order of magnitude larger than calculated by Barker at 1000 mbar.[25] The larger Φ_{CH_3CO} asymptote would arise if the triplet barrier were significantly lower than previously identified, the rate coefficient for the triplet dissociation is larger, or due to the enhanced importance of internal conversion from the excited singlet to a vibrationally excited ground state at low excitation energies. The barrier for the dissociation of ground state acetone can be estimated to be small from the measured thermal dissociation of acetone.[80] The origin of the excited singlet energy surface (329 nm) lies above the threshold for decomposition of the ground state (339 nm), such that any internal conversion results in acetone with enough energy to break the C-C bond. The Barker model suggests the importance of the relative rates of intersystem crossing (both between S_1 and T_1 and T_1 and S_0) and internal conversion, both of which are altered by collisional interactions,[25] on the resulting fate of photoexcited acetone molecules. Barker's model agrees with the limited results of Gierczak et al.[36] at 337 nm which were also lower ($\geq$0.01) than our lower limit of 0.04. Blitz et al. did not observe non-zero quantum yields,[22] while Emrich and Warneck[40] reported a value of Φ_{CH_3CO} at 330 nm, at least a factor of two larger than those observed here.

Our observed pressure dependence of Φ_{CH_3CO} at λ > 320 nm differs from shorter wavelengths. By comparison, our results at 320 nm agree quite closely with the results of both Gierczak et al.[36] and Emrich and Warneck.[40] We do not currently have an explanation for the observed lack of pressure dependence at 325 and 330 nm. Regardless of the larger Φ_{CH_3CO} limit or the unexpected pressure effects at λ > 320 nm, our observations of a long wavelength Φ_{CH_3CO} asymptote agrees with Barker's model of the acetone photolysis mechanism. Barker had many adjustable parameters in his model. Therefore, his model could be consistent with our observations if some of those parameters were varied.

2.5 Conclusions

Our I-CIMS coupled with a wide-band light source and monochromator produced Φ_{CH_3CO} in acetone photolysis for wavelengths from 280 to 330 nm pressures from 150 to 850 mbar, through measurement of the primary product of acetone photolysis in the troposphere, $CH_3C(O)$ (via conversion to $CH_3C(O)O_2$). We presented room temperature Φ_{CH_3CO} as a function of wavelength and pressure, which may be used to model acetone photolysis rates and photo-physics. In addition, we identified clear evidence of Φ_{CH_3CO} that does not approach zero as excitation wavelengths approach the photolysis threshold of 338 nm at 298 K. Our study is comprehensive in terms of pressures and wavelengths used. Also, we have directly measured the yield for $CH_3C(O)$ radical production. Other questions remain about the acetone photodissociation mechanism in the troposphere, including the potential impacts of quenching by water. In the upper troposphere, water vapor pressure is sufficiently small that the quenching by H_2O will have to be unrealistically large to make a difference. Further measurements at reduced temperatures could help better define Φ_{CH_3CO} under upper tropospheric conditions. As noted earlier, we do not see any evidence for reaction of $CH_3C(O)CH_3^*$ with O_2. The atmospheric photolysis rates of acetone found using the present method are shown in Chapter 3.

CHAPTER 3: QUANTUM YIELDS FOR $CH_3C(O)$ IN ACETONE PHOTOLYSIS AS A FUNCTION OF PRESSURE, TEMPERATURE, AND WAVELENGTH

3.1 Abstract

Acetone is one of the most abundant non-methane trace gases, and its photolysis contributes to radical production in the upper troposphere. Due to a lack of measurements of the radical products from acetone photolysis in the troposphere, the rates and mechanism of acetone loss and potential HO_x and PAN production from its photolysis products are uncertain. Here, we expand our previous chemical ionization mass spectrometry measurements of acetone photolysis to conditions representative of the troposphere: temperatures from 228 to 323 K, pressures between 150 and 850 mbar, and excitation wavelengths from 280 to 325 nm. These studies measured one of the primary radical products of acetone photolysis in air, the acetyl peroxy radical. We parameterize the acetyl peroxy radical quantum yields under tropospheric conditions and compare our data and parameterizations with those prior studies. Our results indicate that acetone photolysis in the upper troposphere is up to a factor of 1.4 slower than previously calculated.

3.2 Introduction

Production of radicals in the troposphere is often driven by photolysis of O_3. Photolysis of ozone produces $O(^1D)$, which reacts with water vapor to make hydroxyl radicals (OH). Hydroxyl radicals oxidize trace gases, removing climate-forcing gases and pollutants. Subsequent reactions of the oxidized trace gases recycle radicals and O_3 back into the atmosphere.[4] The results of oxidation are not always beneficial. Under the right conditions, the oxidation of trace gases can "clean" the atmosphere, through trace gas removal, or worsen air quality, producing photochemical smog, particulate matter, or oxygenated gases that are hazardous to human health.

Discrepancies and uncertainties exist between measured and modeled OH and HO_2 (HO_x) concentrations, particularly in the upper troposphere.[10] Measured HO_x concentrations are often larger than calculated in this region. Understanding the cause of this discrepancy will improve predictions of the total oxidative potential throughout the troposphere.

In regions with underpredictions of HO_x concentrations, photolysis of other trace gases could be a source of additional HO_x.[3] Acetone is the most abundant oxygenated organic gas in the troposphere,[13,14] and acetone photolysis is expected to be a significant source of HO_x in the upper troposphere.[9] However, the contribution of acetone photolysis to the HO_x budget in the upper troposphere is not fully understood. At present, it is expected that acetone photolysis may equal the rate of radical production from ozone photolysis in the upper troposphere, where water concentrations are low.[17]

The dominant immediate products of acetone photolysis in the troposphere are the acetyl ($CH_3C(O)$) and methyl (CH_3) radicals.[15] These radicals quickly add oxygen at tropospheric pressures to produce acetylperoxy ($CH_3C(O)O_2$) and methylperoxy (CH_3O_2) radicals. The primary radical products of acetone photolysis are difficult to detect.[12] Currently used values for acetone photolysis quantum yields were not generated from direct measurements of those products under tropospheric conditions and photon excitation energies.[22] The lack of more direct measurements of photolysis products leads to uncertainties in the quantum yields in acetone photolysis in the troposphere and ambiguity in the acetone photolysis mechanism near the energy threshold for photolysis (338 nm at 298 K).[25]

Chapter 2 describes the use of chemical ionization mass spectrometry with iodide reagent ions (I-CIMS) to measure the quantum yields of thermalized $CH_3C(O)$ (Φ_{CH3CO}) in acetone photolysis in synthetic air through the detection of $CH_3C(O)O_2$.[81] We combined our I-CIMS with

a selectable wavelength light source and photolysis reactor. To calculate quantum yields, we compared the production of $CH_3C(O)O_2$ at wavelengths between 280 and 330 nm to previously reported quantum yield for [35] $CH_3C(O)$ at 254 nm at pressures between 150 – 850 mbar at 298 K.

Here, we extend the I-CIMS measurements of $CH_3C(O)$ quantum yields to temperatures (223 – 300 K), pressures (150 – 850 mbar), and wavelengths (280 – 325 nm) prevalent in the troposphere. We parameterize Φ_{CH3CO} from acetone photolysis as a function of temperature, pressure, and wavelength in the troposphere. Comparison of our parameterization to the currently recommended quantum yields for acetone reveals a mild decrease in the expected acetone photolysis rates in the uppermost regions of the troposphere, where temperatures reach ca. 220 K and pressures are less than 150 mbar.

3.3 Methods

We measured Φ_{CH3CO} using the instrument described in Chapter 2 but using a reactor with temperature varied between 228 and 323 K (Figure 3.i). In short, this design involved coupling an atmospheric-pressure interface, time-of-flight mass spectrometer (Tofwerk) equipped with iodide reagent ions (I-CIMS) to a KiloArc (Horiba) 1 kW Xe arc lamp with a monochromator to provide light of selected wavelength and a photoreactor. The I-CIMS measured the production of $CH_3C(O)O_2$ from acetone photolysis in air at wavelengths from 254 to 325 nm. We operated the I-CIMS ion-molecule reactor at 100 mbar total pressure and ~0.6 mbar H_2O. An iHR320 monochromator (Horiba) selected the photolysis wavelength with ~3.7 nm full width at half-maximum resolution for 1 mm entrance and exit slit widths and ~5.4 nm resolution for 2 mm slits. An antireflection-coated fused silica lens focused the monochromator beam to a spot ca. 1 cm^2 at the reactor center.

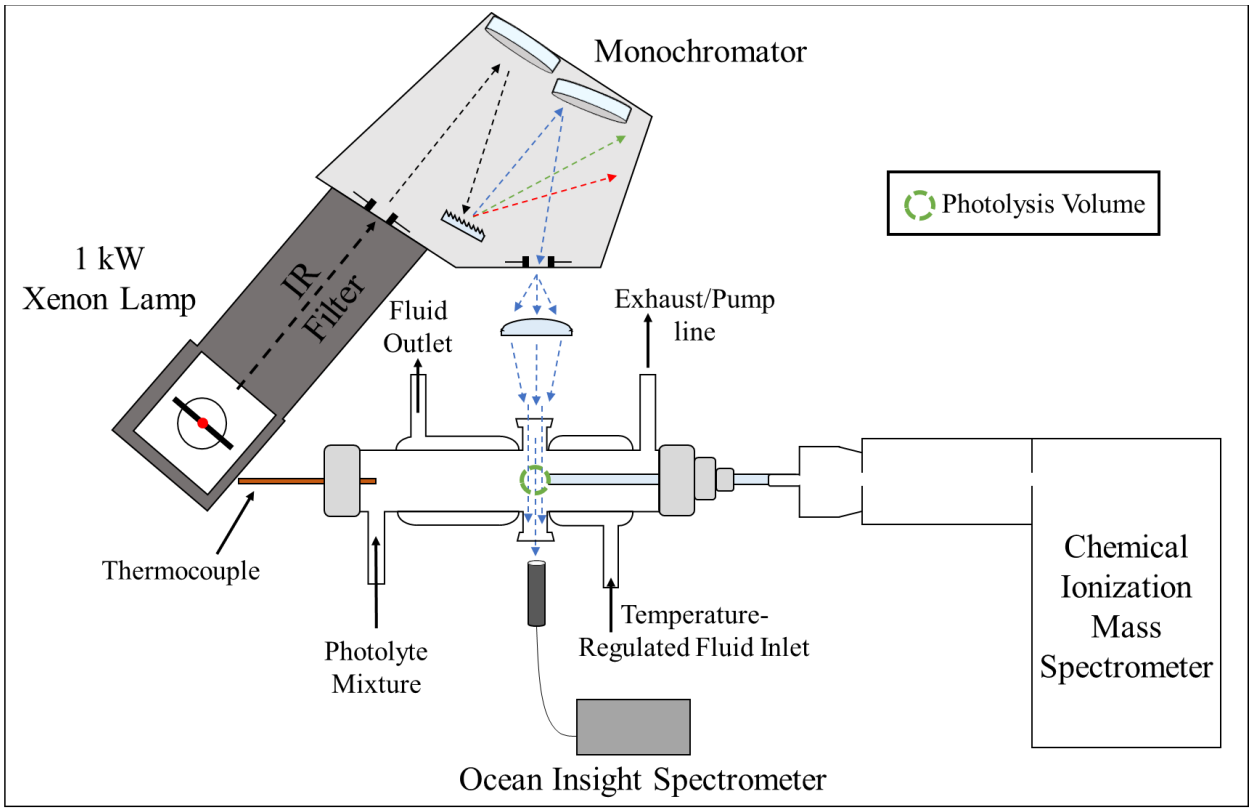

Figure 3.i Schematic of the I-CIMS acetone photolysis measurement system. This is a simplified version of the schematic included in Chapter 2, with the added depiction of the reactor jacket used for cooling and heating of the photolyte mixture.

The reactor (Allen Scientific Glass) was a modified 1" O.D. Pyrex tube with 2 mm thick walls. The reactor used in Chapter 2 was modified with an outer glass jacket for temperature control with cooled or heated liquid. The I-CIMS sampled the reactor flow through a 0.25" glass tube, which we inserted at one end of the 1" reactor tube to the edge of the photolysis region (≤ 0.5 cm from the beam path). We used the other end of the 1" reactor to insert a thermocouple to measure temperature in the photolysis region. A diaphragm pump connected to the exhaust stem reduced pressure in the reactor for measurements less than 850 mbar. The pumping rate was controlled by a manual needle valve. For experiments below room temperature, a ULT-80 (NesLab) recirculating chiller provided cooled ethanol flow to the reactor jacket. The chiller could cool the photolysis volume down to 228 K at 150, 300, and 500 mbar, but could not cool to this

temperature for higher pressures. For experiments at 50 °C, we connected the jacket to a flow of heated water from a 9112A11B (Polyscience) recirculating bath.

Experimental design and data processing also followed the methods described in Chapter 2. After setting the pressure and temperature for the experiment we introduced acetone into the reactor with a dilution flow of ultra-zero air (UZA; Airgas). Flow through the volume before the photolysis region ensured that the gas mixture was at the desired temperature. The total flow in the reactor was maintained between 2.5 and 3 L min^{-1} from the UZA mass flow controller. A MKS Baratron pressure transducer measured the reactor pressure. A thermocouple inserted into the photolysis region measured reactor temperature before the first planned experiment and every 2nd or 3rd experiment thereafter. We moved the thermocouple outside the reactor flow path after measuring the temperature.

Φ_{CH3CO} was calculated from the ratio of $CH_3C(O)O_2$ signals at a target wavelength between 280 and 325 nm to that measured when the monochromator was set at 254 nm. As shown by E1 this method derives Φ_{CH3CO} from relative signals of the $CH_3C(O)O_2$ product ion, $I(CH_3C(O)O_2)^-$, and the ratios of the measured photon fluxes at the two wavelengths.

$$\Phi_{CH_3CO,\lambda} = \Phi_{CH_3CO,254} \times \frac{I(CH_3C(O)O_2)^-_\lambda}{I(CH_3C(O)O_2)^-_{254}} \times \frac{\sigma_{254}}{\sigma_\lambda} \times \frac{F_{254}}{F_\lambda} \qquad \text{E1}$$

$\Phi_{CH_3CO,\lambda}$ is the quantum yield of $CH_3C(O)$ at the target wavelength, while $\Phi_{CH_3CO,254}$ is the quantum yield at 254 nm,[35] which was our reference wavelength. The $I(CH_3C(O)O_2)^-$ terms represent the measured ion signal from the reaction between I^- and $CH_3C(O)O_2$ at the two wavelengths, σ are the absorption cross section of acetone at the noted wavelengths, and F is the measured photon flux. The terms in E1 were used for a given temperature. $\Phi_{CH_3CO,254}$ is expected to be independent of temperature. The absorption cross sections of acetone are temperature-dependent, as the initial distribution of vibrational states for the population of acetone molecules

changes with temperature. We used the absorption cross-sections from Gierczak et al.[36] and adjusted it for temperature using the NASA-JPL parameterization.[64] Relative photolysis flux (F_{254}/F_{λ}) was measured at the light exit of the reactor by a calibrated HR2000-CG-UV-NIR spectrometer (Ocean Optics) connected to a fiber optic cable and cosine collector. Neither the $CH_3C(O)O_2$ concentration nor the total photon flux in the reactor needs to be explicitly known.

We performed five replicate quantum yield measurements at a given wavelength, pressure, and temperature. The script for controlling the monochromator setting cycled between a target and reference (254 nm) wavelength for each quantum yield determination. The light was blocked to collect instrument backgrounds after the 1st and 3rd trials. The waveforms of the measure variables ($I(CH_3C(O)O_2)^-$ and F) are shown in Figure 2.ii in Chapter 2.

3.4 Results and Discussion

3.4.1 Φ_{CH3CO} in acetone photolysis as a function of temperature, wavelength, and pressure

The quantum yields of $CH_3C(O)$ shown in Figure 3.ii demonstrate the impact of lowered temperatures on acetone photolysis. In general, Φ_{CH3CO} increased as pressure in the reactor was reduced, but decreased with decreasing temperature. Our results at the highest excitation energies (shortest wavelengths) suggest that thermalized $CH_3C(O)$ is the dominant product of acetone photolysis in the upper troposphere, with the subsequent decomposition of $CH_3C(O)$ unlikely to be an important process. The data above 315 nm shows the appearance of non-zero minimum quantum yields with the lowest observed quantum yields between 0.02 and 0.03 at all temperatures.

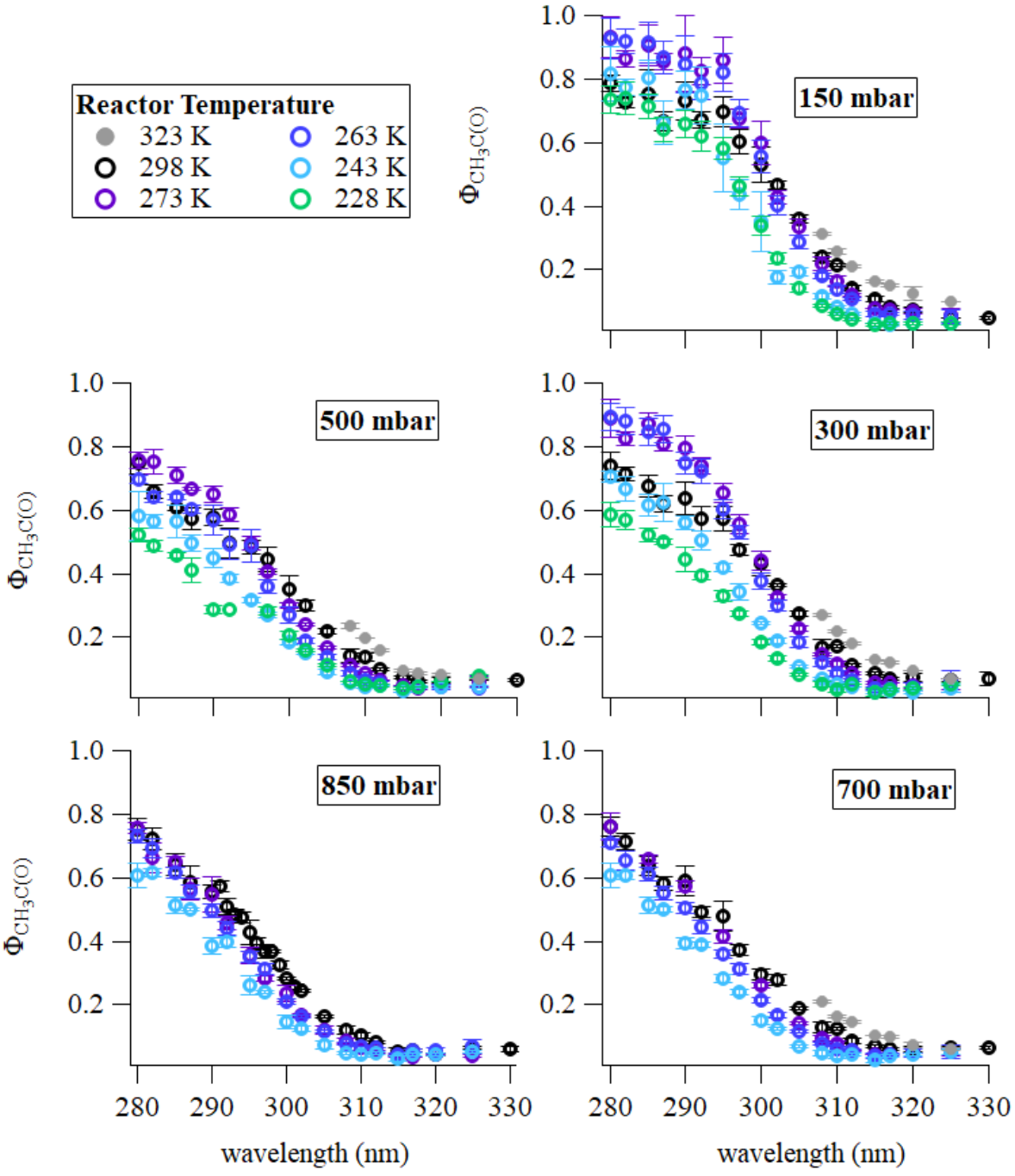

Figure 3.ii Quantum yields for $CH_3C(O)$ as a function of wavelength and temperature, separated by pressure. The markers represent an average of at least 3 measurements at each condition, with error bars being the 1σ standard deviations.

The quantum yields for $CH_3C(O)$ decreased with decreasing temperature at all wavelengths and pressures. For $\lambda < 290$ nm, the decrease from 298 to 228 K was < 30% for all pressures. At

longer excitation wavelengths greater than or equal to 290 nm, there was a greater dependence of Φ_{CH3CO} on temperature. The decreases in Φ_{CH3CO} from 298 K to 228 K were ≥ 60% for 302 to 315 nm excitation. The largest observed decrease in quantum yield from the room temperature experiments was 79% for 310 nm excitation at 300 mbar. The impacts of both temperature and pressure lessen above 315 nm. In Chapter 2, we observed no clear pressure dependence on Φ_{CH3CO} in the wavelength range between 315 and 325 nm (at 298 K). That observation holds for lower temperatures as well, within the uncertainty of our measurements. We observed a slight decrease in the minimum Φ_{CH3CO} over this wavelength range, from a minimum of ~0.04 at 298 K to ~0.03 at 228 K. These numbers are essentially the same.

Our data suggests that upper tropospheric acetone photolysis primarily results in the formation of $CH_3C(O)$. We observed slight increases of Φ_{CH3CO} (< 300 nm) between room temperature and both the 273 and 263 K data at 150 and 300 mbar. Φ_{CH3CO} at 500 mbar also increased slightly for 273 K in the lower wavelength range. Our comparison to literature data at 298 K in Chapter 2 suggests some pressure dependence on this process. A potential process that reflects our observations is provided in the acetone photolysis parameterization of Blitz et al.,[22] i.e., secondary decomposition of $CH_3C(O)$ before thermalization. However, Blitz et al.[22] suggest this process as only a function of excitation energy and temperature, and more recent literature has questioned the importance of nascent $CH_3C(O)$ decomposition for excitation wavelengths greater than 280 nm.[23,30]

From 248 to 266 nm, vibrationally hot $CH_3C(O)$ formed from acetone photolysis can decompose to CH_3 and CO.[34,59] This is a stepwise process.[58] Rajakumar et al.[35] observed this at 248 nm as a decrease in Φ_{CH3CO} with pressure, as fewer of the hot $CH_3C(O)$ could be stabilized by collisions before dissociation. Blitz et al.[22] observed signs of temperature-dependent $CH_3C(O)$

dissociation below 300 nm. Our data reflects this temperature-dependent $CH_3C(O)$ dissociation. Given the clear temperature dependence, dissociation of $CH_3C(O)$ is not important to acetone photolysis in the upper troposphere.

Our results for wavelengths > 315 nm demonstrate that Φ_{CH3CO} does not decrease to zero as the excitation wavelength approaches the acetone photolysis threshold for any conditions in the troposphere. As with our room temperature measurements, the pressure impacts on Φ_{CH3CO} at $\lambda >$ 315 nm are minimal at all studied temperatures. The change in Φ_{CH3CO} with temperature was also smaller than expected for the low excitation energies. The non-zero lower limit to Φ_{CH3CO} at all measurement conditions agrees with the acetone photolysis model developed by Barker.[25] However, the minimum Φ_{CH3CO} was consistently larger than that predicted by the Barker model for reasons that we are unable to identify. Experimental uncertainties of our measurements at > 315 nm were often large (~50%; 1σ precision of ~30%) due to low radical production. From those uncertainties, we estimate a lower limit Φ_{CH3CO} of 0.01 in the upper troposphere, which is larger than both the Barker model[25] and the parameterization of Blitz et al.[22]

3.4.2 Parameterization of Φ_{CH3CO} in the upper troposphere

Equations 2 through 4 provide our parameterization of Φ_{CH3CO} as a function of temperature, pressure, and excitation wavelength for tropospheric conditions. To obtain this parameterization, we first fit Φ_{CH3CO} as a function of wavelength at each temperature and pressure to a sigmoid curve (E2), following the method of Link et al.[82] in an upcoming publication on reanalysis of prior acetone photolysis data. We then parameterize the obtained coefficients for the sigmoid fits with pressure (E3a-b) and temperature (E4a-g) to reproduce our experimental data. Further details on all experimental fits can be found in Appendix C. A combination of linear (for χ_0 and χ_1) and exponential (for χ_2 and χ_3) functions were used to parameterize the sigmoid curves for pressure,

and polynomial functions of the form $y = A_0 + A_1x + A_2x^2$ were used to parameterize for temperature from 298 to 243 K.

$$\Phi_{CH_3CO}(\lambda) = \chi_0 + \frac{\chi_1}{1 + \exp\left(\frac{\chi_3 - \lambda}{\chi_2}\right)} \quad \text{E2}$$

$$\chi_{0-1} = (p)a_{0-1} + b_{0-1} \quad \text{E3a}$$

$$\chi_{0-1} = a_{2-3}\exp\left(-(p)c_{2-3}\right) + b_{2-3} \quad \text{E3b}$$

$$a_0 = (0.0123 \pm 0.0008) - (9.7\times10^{-5} \pm 6\times10^{-6})T + (1.9\times10^{-7} \pm 1\times10^{-8})T^2 \quad \text{E4a}$$

$$b_0 = (-15.8 \pm 0.3) + (0.125 \pm 0.002)T - (2.3\times10^{-4} \pm 4\times10^{-6})T^2 \quad \text{E4b}$$

$$a_1 = (-0.010 \pm 0.03) + (8\times10^{-5} \pm 2\times10^{-5})T - (1.6\times10^{-7} \pm 4\times10^{-7})T^2 \quad \text{E4c}$$

$$b_1 = (15 \pm 1) - (0.12 \pm 0.01)T + (2.2\times10^{-4} \pm 2\times10^{-5})T^2 \quad \text{E4d}$$

$$a_2 = (360 \pm 60) - (2.7 \pm 0.5)T + (5.1\times10^{-3} \pm 9\times10^{-4})T^2 \quad \text{E4e}$$

$$b_2 = (-510 \pm 90) + (3.9 \pm 0.7)T - (7\times10^{-3} \pm 1\times10^{-3})T^2 \quad \text{E4f}$$

$$c_2 = (0.55 \pm 0.05) - (4.1\times10^{-3} \pm 4\times10^{-4})T + (7.5\times10^{-6} \pm 7\times10^{-7})T^2 \quad \text{E4g}$$

$$a_3 = (-700 \pm 100) + (5.5 \pm 0.9)T - (0.010 \pm 0.002)T^2 \quad \text{E4e}$$

$$b_3 = (900 \pm 100) - (4.9 \pm 0.7)T + (9\times10^{-3} \pm 1\times10^{-3})T^2 \quad \text{E4f}$$

$$c_3 = (0.58 \pm 0.03) - (4.4\times10^{-4} \pm 2\times10^{-5})T + (8.4\times10^{-7} \pm 4\times10^{-8})T^2 \quad \text{E4g}$$

Figure 3.iii compares calculated Φ_{CH3CO} to our measurements. This system of equations reproduces our data over the temperature range included in fitting, but not below 243 K. We calculate Φ_{CH3CO} for T < 243 K using the change in Φ_{CH3CO} observed from 243 K to 228 K at 150, 300, and 500 mbar. The average decrease across all three pressures and all wavelengths is 0.4% K^{-1}. Application of this decrease at all wavelengths provided the best agreement with our measurements. A wavelength-dependent adjustment to Φ_{CH3CO} < 243 K is discussed in the Appendix C. Using the calculation of Φ_{CH3CO} < 243 K described above, the calculated Φ_{CH3CO} fit

the measured data well across temperature changes. Agreement across pressures is good at short wavelengths but diverges for lower pressures at $\lambda > 300$ nm. This is likely driven by the lack of consistent pressure dependence at the longest wavelengths.

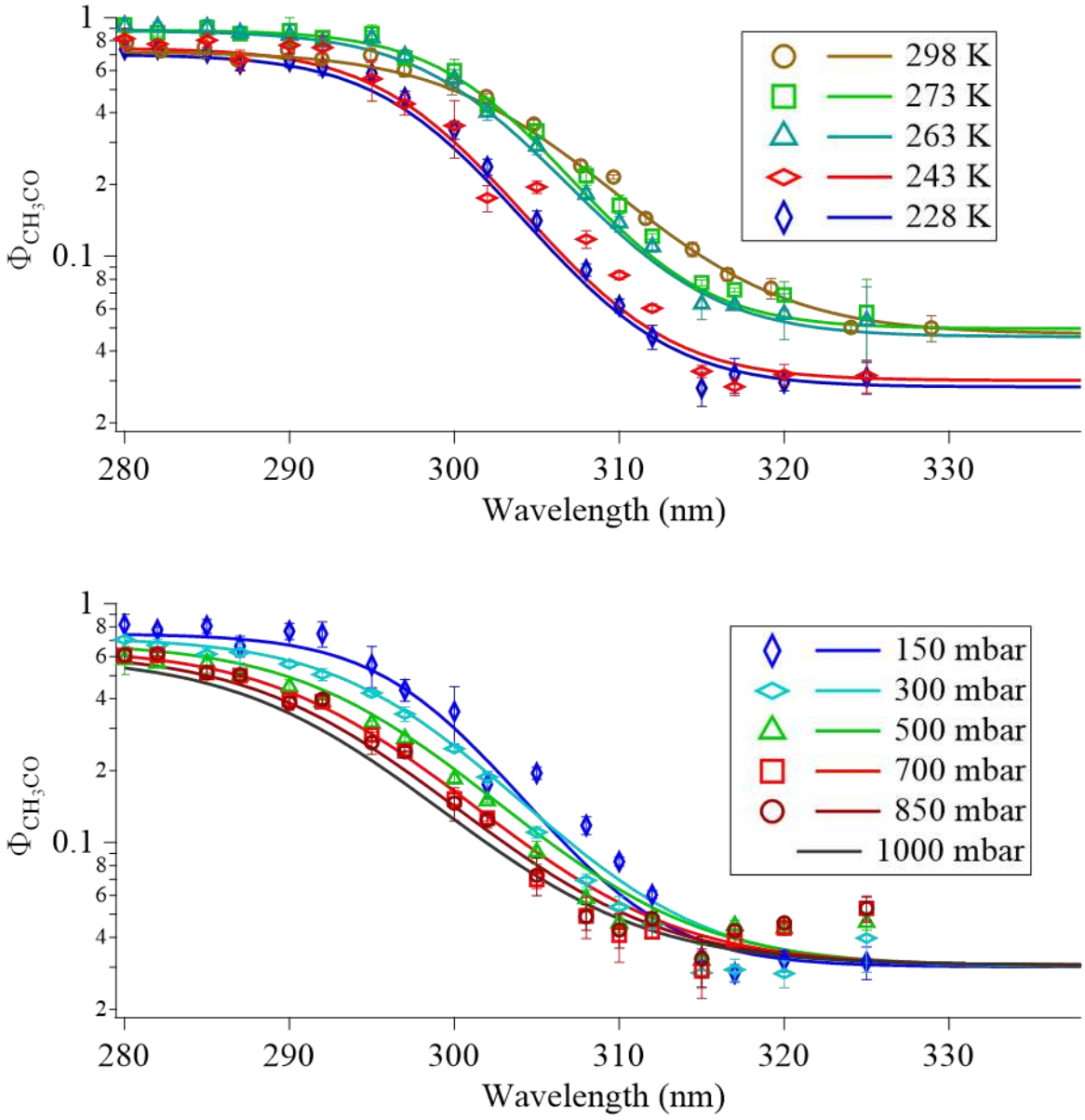

Figure 3.iii Comparison of parameterized data (solid lines) to measurements (markers): (upper) as a function of temperature at 150 mbar, (lower) as a function of pressure at 243 K.

We note that our parameterization only pertains to the production of thermalized $CH_3C(O)$ from acetone photolysis. I-CIMS is not able to detect loss of acetone, production of CO, or any

other products (CH_3O_2, C_2H_6) that could indicate CO formation. As such, our experimental design is blind to the photolysis channel leading to CO and C_2H_6.[23,30] As with the Blitz et al.[22] parameterization (hereafter referenced as Blitz), an additional component could be added to E2, describing the secondary decomposition of $CH_3C(O)$ to CH_3 and CO as a function of temperature and wavelength. We do not include the possible decomposition of vibrationally hot $CH_3C(O)$ in our parameterization. Both our data and that of Blitz suggest $CH_3C(O)$ decomposition occurs at temperatures > 273 K and excitation energies < 300 nm, making this process unimportant to acetone photolysis rates in most of the troposphere.

3.4.3 Comparison to acetone photolysis literature

We find some clear consistencies and differences in the comparison of our data with that of the Blitz parameterization. Our Φ_{CH3CO} as a function of wavelength and temperature at 150 mbar are shown in Figure 3.iv. Blitz used measurements of OH, a side product channel of the $CH_3C(O)$ + O_2 reaction.[22] Due to the low yields of OH production from this reaction, these Φ_{CH3CO} measurements were largely conducted at pressures lower than those used here. At 150 mbar the branching ratio for OH according to Blitz is 0.2 to 0.4 (depending on temperature) in an He bath gas.[46] However, other studies have found this yield to be much smaller in He[83] and even smaller in N_2.[44,79] Papadimitriou et al.[78] report an OH yield of about 0.03 at 150 mbar and even smaller values at higher pressures. We suggest that the Φ_{CH3CO} reported here accurately describes those produced in acetone photolysis in the troposphere.

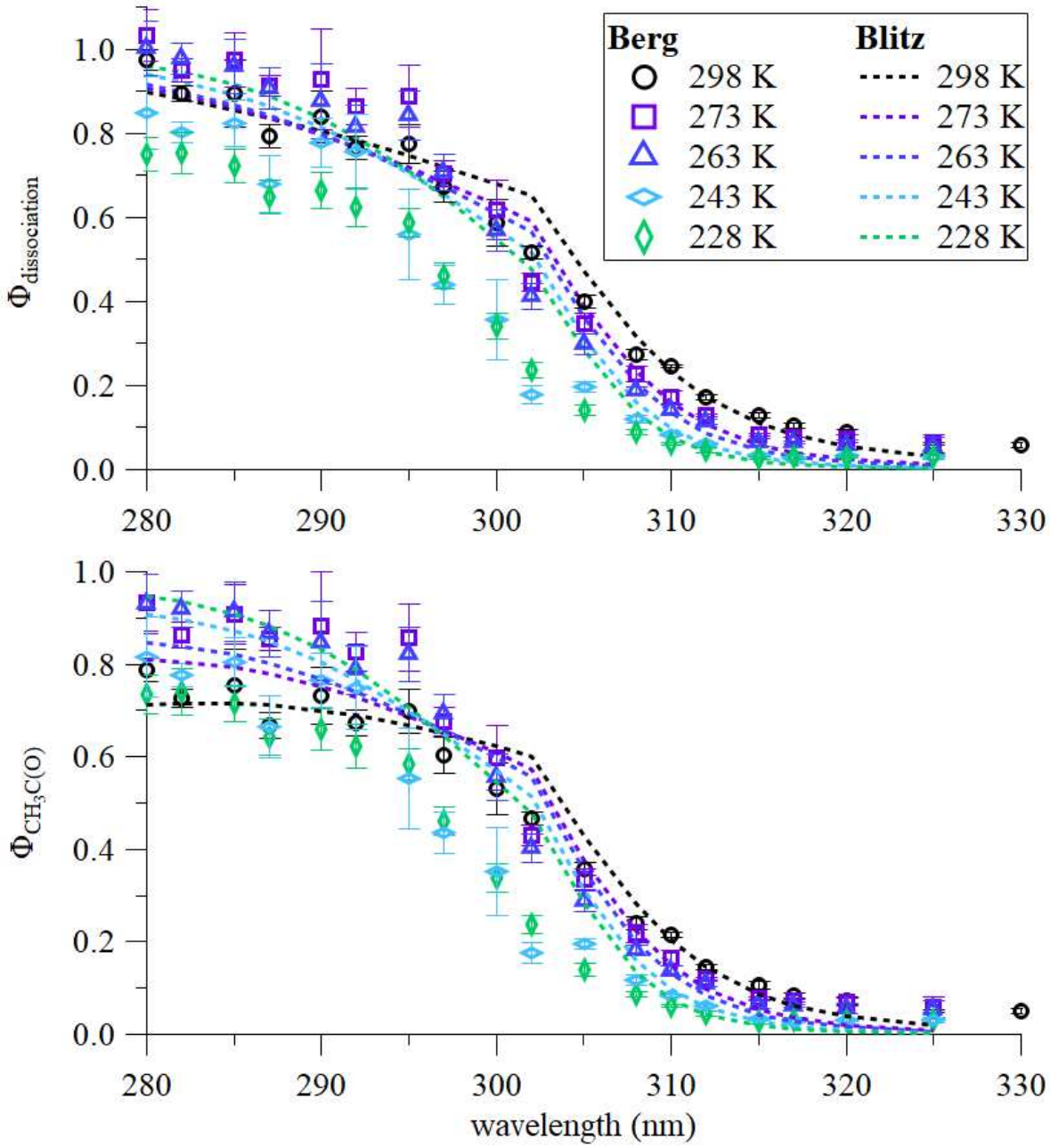

Figure 3.iv (Upper) Total acetone dissociation quantum yields ($\Phi_{dissociation}$) as a function of wavelength and pressure at 150 mbar, obtained through the addition of the Blitz parameterization of CO quantum yields (Φ_{CO}) to measured Φ_{CH3CO} for this study (markers) and Blitz (dashed lines). (Lower) Φ_{CH3CO} from this study and the Blitz parameterization as a function of wavelength and temperature at 150 mbar. Shaded areas represent the 1σ precision of our data.

Both datasets show an increase in Φ_{CH3CO} below ~300 nm upon decrease in temperature from 298 to 263 K. Our results agree with the inclusion of a temperature-dependent $CH_3C(O)$ decomposition

component (otherwise CO yield; Φ_{CO}) to the total acetone photodissociation quantum yield (Φ_{diss}) in this range (or some other process reduces Φ_{CH3CO} at higher temperatures). As shown in the upper portion of Figure 3.iv, Φ_{CO} proposed by Blitz (based on measurements by Gandini[29] and Hacket and Horowitz[28]) agrees with our Φ_{CH3CO} data. Addition of Blitz Φ_{CO} to our Φ_{CH3CO} at 150 mbar produces Φ_{diss} within a few percent of unity for temperatures between 263 and 298 K and wavelengths between 280 and 290 nm, in close agreement with room temperature Φ_{diss} measurements at similar pressures.[36] While the process that causes the temperature dependence of Φ_{CH3CO} between 280 and 290 nm is not clear from our measurements, the yields of this process agree with the proposed Φ_{CO} yield from Blitz.[22]

Where our data differs from the Blitz parameterization is in the temperature of the largest observed Φ_{CH3CO} between 280 and 290 nm and the overall dependency of Φ_{CH3CO} on temperature in the troposphere. Blitz measured Φ_{CH3CO} primarily in He and small amounts of O_2, with data suggesting similar quenching efficiency for He and N_2 or Air bath gases.[22] Our data suggests that N_2 and O_2 in the troposphere quench excited acetone more efficiently, with the largest Φ_{CH3CO} between 273 and 263 K. Our 243 and 228 K data show lower Φ_{CH3CO} in the upper troposphere even for 280 to 290 nm excitation. Our Φ_{CH3CO} are smaller from 290 to 310 nm for the conditions of the upper troposphere as well, with a larger overall temperature dependence in this wavelength range. Our Φ_{CH3CO} and those of Blitz converge around 312 nm for all temperatures. It is important to note that while there are differences between ours and that of Blitz, the overall values and their variation with wavelengths are very similar.

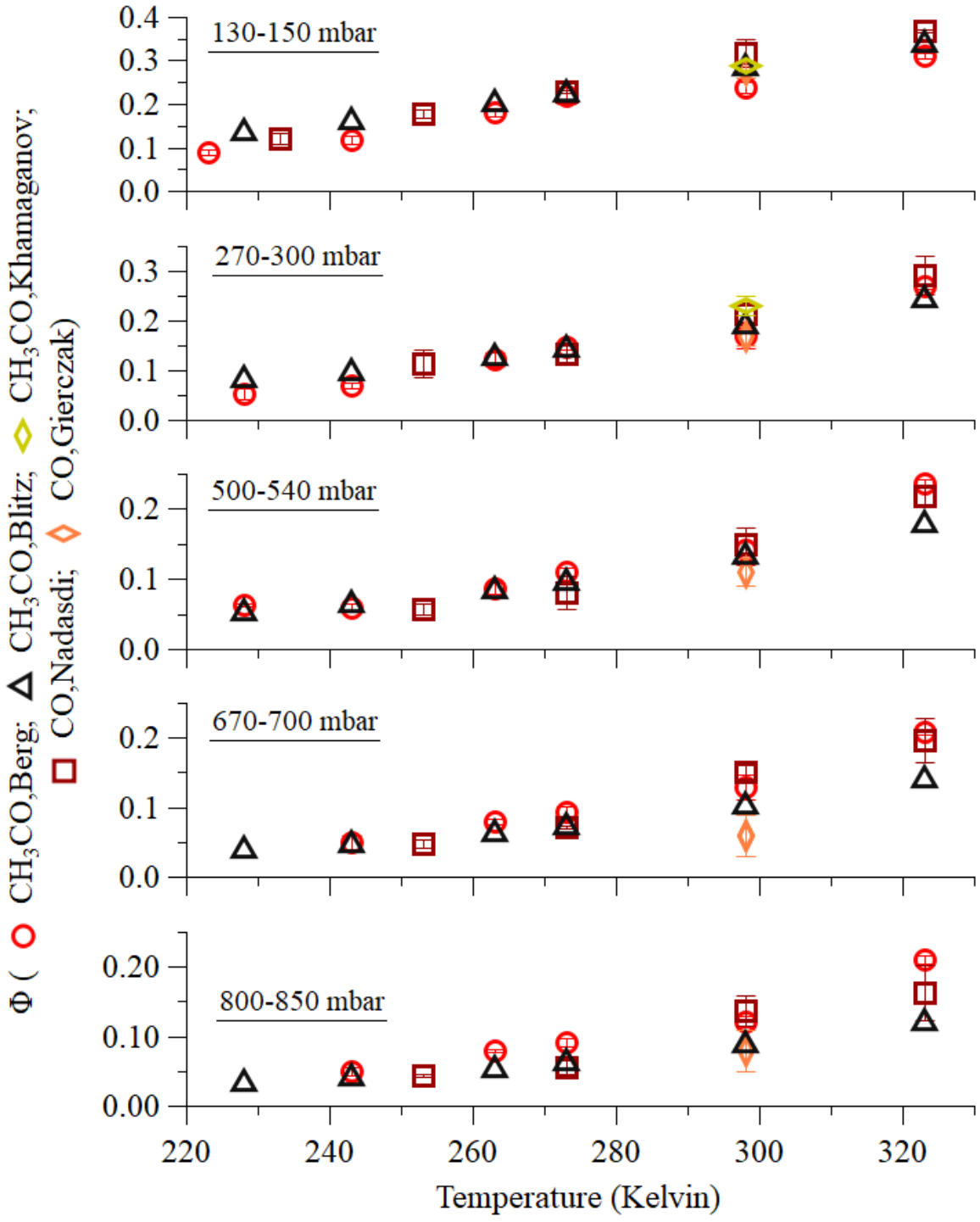

Figure 3.v Comparison of quantum yields to literature at 308 nm. Includes Φ_{CH3CO} from this study (red circles), Blitz[22] (black triangles), and Khamaganov et al.; and $\Phi_{dissociation}$ from Nadasdi et al.[38] (dark-red squares) and Gierczak et al.[36] (orange diamonds) included. Error bars taken from 1σ standard deviations of all measurements; not provided for calculated Φ_{CH3CO} from Blitz.

Photolysis of acetone has been extensively studied at 308 nm, and could, in theory, be used as a reference wavelength for calculating Φ_{CH3CO}. We compare our 308 nm Φ_{CH3CO} to literature data in Figure 3.v and find very good agreement overall. Φ_{CH3CO} from this study agrees quite well with Φ_{diss} from Nádasdi et al.[38] at all pressures and temperatures and with the room temperature measurements from Gierczak et al. for ≤ 500 mbar.[36] Both studies measured Φ_{diss} through the depletion of acetone (with some measurements of CO_2 production through secondary chemistry by Gierczak et al.)[36] primarily in synthetic air. Agreement with Blitz Φ_{CH3CO} is also good throughout, though their Φ_{CH3CO} are slightly larger at the pressures and temperatures of the upper troposphere.[22] The overall agreement in Figure 3.v suggests that the 308 nm Φ_{CO} included in the Blitz parameterization (0.03 at 298 K and 0.08 at 323 K) is an insignificant process in the troposphere for $\lambda \geq 308$ nm excitation.

Above 315 nm, our data shows near constant Φ_{CH3CO} with wavelength up to 325 nm (330 nm at room temperature), with minimum Φ_{CH3CO} larger than most previous literature. The onset of the minimum Φ_{CH3CO} in our data begins at shorter wavelengths than predicted by the Barker photophysical model.[25] The minimum Φ_{CH3CO} observed here (0.03) is over an order of magnitude larger than that predicted by Barker. Experimental evidence of non-zero acetone quantum yields approaching the photolysis threshold is limited. The room temperature Φ_{diss} reported by Gierczak et al.[36] at 337 nm were larger than the Barker model as well, though they observed a linear Stern-Volmer relationship; we see a slightly non-linear variation. Emrich and Warneck[40] present room temperature Φ_{CH3CO} at 330 nm which is also pressure-dependent, but much larger than other literature values (≥ 0.1). Blitz data instead suggests that Φ_{CH3CO} should decrease with excitation energy up to the 338 nm threshold.[22] Our data indicates that Φ_{CH3CO} in the thermalized triplet photolysis region (315 – 338 nm) is only slightly dependent on temperature and pressure, leading

to larger Φ_{CH3CO} in the upper troposphere than previously expected for this wavelength range (Figure 3.vi).

We have calculated the differences in the first order rate coefficient for the loss of acetone or production of $CH_3C(O)$, J value, for Blitz et al. and our data, and it is shown in Figure 3.vi. This is a very simple and illustrative calculation; atmospheric calculations need to be carried out as a function of altitude, solar zenith angle, and other conditions.

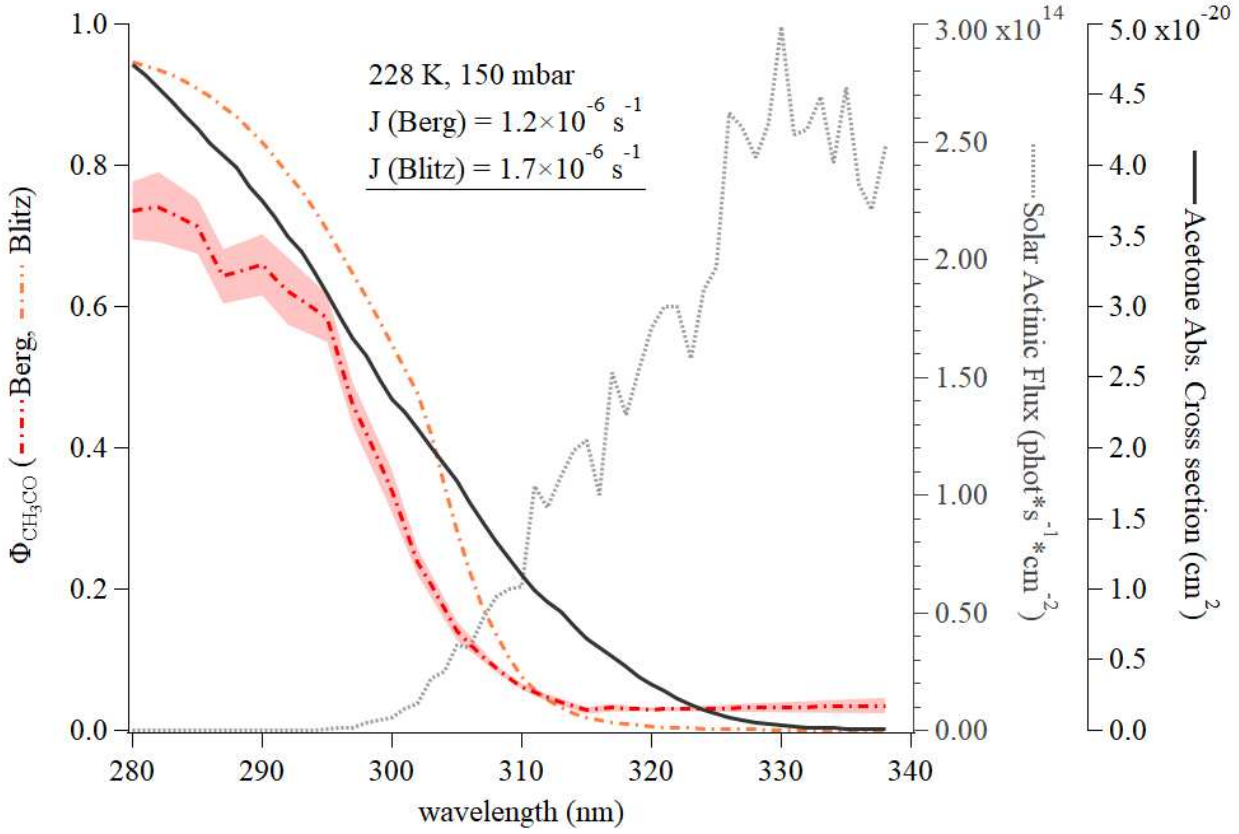

Figure 3.vi Comparison of upper troposphere acetone photolysis rates to current recommendations. The left ordinate shows Φ_{CH3CO} from this study (red dashed line) and the Blitz et al.[22] parameterization (orange dashed line) from 280 to 338 nm. These are shown alongside acetone absorption cross sections (right-most ordinate, black line) and solar actinic flux (right ordinate, dashed line) at 13.5 km calculated for a solar zenith angle of 0, an overhead ozone of 300 DU, and surface albedo of 10%. Acetone photolysis rate coefficients (J) are provided in the graph legend.

The calculated J-values using our quantum yields are 1.4 times lower than those from Blitz et al. This difference is primarily due to the differences in the quantum yields in the wavelength

region of 300 to 310 nm. Clearly, the finite value of the quantum yield at longer wavelengths has a minimal influence in the atmospheric photolysis rates.

Conclusion

Our I-CIMS measurements of Φ_{CH3CO} in acetone photolysis as a function of wavelength, temperature, and pressure mark the first such characterization of acetone photolysis through the detection of a primary radical product of its photolysis in the troposphere, $CH_3C(O)O_2$. Our measurements of Φ_{CH3CO} were made under conditions pertinent to the troposphere. Thus, the parametrization of Φ_{CH3CO} provided in this study is the most applicable such parameterization for atmospheric modeling of HO_x production from acetone photolysis. Our data supports previous findings that $CH_3C(O) + CH_3$ is the dominant product channel of acetone photolysis in the upper troposphere. In addition, we found evidence under all tropospheric conditions of a thermalized triplet dissociation regime for excitation wavelengths longer than 315 nm, producing non-zero $\Phi_{dissociation}$ for acetone up to the photolysis threshold. Under conditions of the upper troposphere, Φ_{CH3CO} below 300 nm in this study was smaller than the current recommendations, leading to a factor of ~1.4 decrease in expected acetone photolysis rates in this region. From 320 to 335 nm, the near-constant Φ_{CH3CO} produces a J-value nine times faster than the recommendation. This contributes just 11% of the total J, as the absorption cross sections of acetone at those wavelengths are much smaller. Still, thermalized triplet dissociation is an interesting feature of the acetone photolysis mechanism and should be considered in the photolysis of other ketones as well. A parameterization of Φ_{CH3CO} from this study is provided for use in models of radical production rates throughout the troposphere.

CHAPTER 4: Cl_2^- CHEMICAL IONIZATION MASS SPECTROMETRY (Cl_2-CIMS) FOR MEASUREMENT OF ACYL PEROXY RADICALS

4.1 Abstract

Organic peroxy radicals (RO_2) are produced in the atmosphere by oxidation of volatile organic compounds (VOCs) and, in some cases, VOC photolysis. However, photolytic sources of RO_2 are often poorly understood, in part due to challenges in directly detecting RO_2 in both ambient and laboratory settings. We investigated Cl_2^- as a chemical ionization mass spectrometry reagent ion (Cl_2-CIMS) for measuring and speciating RO_2 in a laboratory setting. Cl_2-CIMS was more sensitive to the acetyl peroxy radical ($CH_3(O)O_2$; 2.30 ± 0.04 ncps/ppt) than iodide CIMS (1.54 ± 0.03 ncps/ppt), but high backgrounds in our setup resulted in a slightly higher detection limit of 5 ppt (1 second integration) for Cl_2-CIMS than I-CIMS (2 ppt). We demonstrate the application of Cl_2-CIMS by quantifying the quantum yields of two radical products, $CH_3C(O)$ and $C_2H_5C(O)$, from methyl ethyl ketone photolysis at 254 nm. We identified O_2^- and Cl^- as possible secondary reagent ions that created unintended product ions in our experiments and thus could complicate the interpretation of Cl_2-CIMS mass spectra for complex atmospheric samples. While several strategies may minimize these effects, Cl_2-CIMS is suitable for measuring RO_2 in controlled laboratory experiments.

4.2 Introduction

Organic peroxy radicals (RO_2) are key components of atmospheric oxidation chemistry but are challenging to measure due to their high reactivity and low ambient concentrations ($\sum RO_2 \leq 1\times10^9$ cm^{-3}).[84,85] RO_2 reactions control hydroxyl (OH) radical production and can contribute to radical termination reactions, thus influencing the lifetime of greenhouse gases and impacting air

quality.[86] RO_2 are primarily formed from the oxidation of volatile organic compounds, though certain moieties, such as aldehydes and ketones, can also undergo photolysis to produce RO_2.[3]

Photolytic sources of RO_2 become more important relative to oxidation reactions in the upper troposphere where oxidants (OH, O_3, NO_3, Cl) are scarce and the actinic flux is higher compared to the rest of the troposphere. For example, acetone photolysis is thought to produce HO_x (OH and HO_2) at a similar rate to the $O(^1D) + H_2O$ reaction in the upper troposphere.[16,17] However, the role of acetone in upper tropospheric HO_x production is poorly understood, as laboratory studies of acetone photolysis quantum yields are limited to indirect measurements of the dominant products: acetyl peroxy ($CH_3(O)O_2$) and methyl peroxy (CH_3O_2) radicals. This results in substantial uncertainties in acetone photolysis quantum yields.[9] Prior studies typically measure either minor photolysis product channels[22] or stable products (e.g., CO, CO_2, and PAN) of secondary reactions.[36,40,41] Photolysis quantum yields for larger and more complex ketones are even more limited, as few techniques can speciate $CH_3C(O)O_2$ and CH_3O_2 radicals from RO_2 of different structures with fast time resolution.[12]

There is a clear need for new analytical techniques to directly measure and speciate RO_2. This would improve laboratory data on acetone and other organic gas photolysis. Ambient measurements could also be improved through the development of a method that could detect individual RO_2 species in the field. Concentrations of RO_2 other than CH_3O_2 and HO_2 (HO_2 can be considered the smallest RO_2 species, given its analogous sources and sinks) are on the order of a few ppt or less.

Approaches to measuring peroxyl radicals are primarily spectroscopic, including ultraviolet[86] and infrared absorbance[87] measurements and cavity ring-down spectroscopy.[88] Laser-induced fluorescence measurements are possible following the conversion of peroxyl radicals to

OH through reaction with CO and NO[89] or chemical amplification.[90] However, these spectroscopic techniques typically cannot quantify speciated radicals and are often limited to measuring HO_2[12] in the lab or summed concentrations of many radical species in the field.[91] One technique that can provide fast, direct, and speciated detection of RO_2 is chemical ionization mass spectrometry (CIMS). CIMS has been used to measure RO_2 in both laboratory and ambient settings. Direct CIMS detection methods include measurements of HO_2 with Br^- reagent ions,[52,53] acyl peroxy radicals ($R(O)O_2$) and other RO_2 with I^- reagent ion measurements (I-CIMS),[55,57] and highly oxidized molecule RO_2 with NH_4^+ or acetate reagent ions.[67] Additional derivatization-aided detection methods exist for H_3O^+, NH_4^+,[92] and NO_3^-, but are typically labor-intensive.[93,94] We recently described the use of I-CIMS to measure ketone photolysis product quantum yields via direct detection of $RC(O)O_2$ produced from photolysis of methyl ethyl ketone (MEK) and 2,3-butadione.[57]

However, available CIMS reagent ions, including iodide, are often subject to interferences that impact RO_2 detection such as decreases in sensitivity due to small amounts of water vapor,[53] unintended production of radicals inside the instrument,[52] and secondary ion chemistry that prevents quantification.[95] The sensitivity of I-CIMS to the acetyl peroxy radical ($CH_3C(O)O_2$) is known to be temperature-sensitive as well.[96] Current detection limits for RO_2 at short integration times (~1 s) are often too high (>5 ppt) for ambient measurements. Laboratory measurements of ketone photodissociation quantum yields are also challenged by high detection limits. Investigation into alternate CIMS reagent ions to measure speciated RO_2 is warranted.

We describe a reagent ion system for CIMS with Cl_2^- as the primary reagent ion (Cl_2-CIMS). We investigate the ion-molecule chemistry and demonstrate the application of Cl_2-CIMS to measurements of $RC(O)O_2$ from photolysis of acetone and methyl ethyl ketone at 254 nm.

Through organic acid and woodsmoke sampling, we evaluate the potential and limitations of Cl_2-CIMS in ambient measurements.

4.3 Methods

4.3.1 The chemical ionization mass spectrometer

We used a time-of-flight chemical ionization mass spectrometer with atmospheric pressure interface (CIMS; Aerodyne Research, Inc.), which consists of an ion-molecule reaction region (IMR), ion optics, and a time-of-flight mass analyzer with a multi-channel plate detector.[49,72] In the IMR, sample air interacts with a flow of reagent ions, which ionize analyte molecules through clustering, proton transfer, charge transfer, or other reactions. We introduced reagent ion flow through the ionizer port on the IMR (Figure 4.i).

Cl_2-CIMS reagent ions were formed by flowing trace concentrations of Cl_2 through a sealed Po-210 α-particle source (Model P-2021; NRD, LLC). We used 12 L glass bulbs filled to 1250 mbar with 100 to 400 ppm Cl_2 in ultra-high purity N_2 (99.999%; Airgas) and calibration gas cylinders containing 10 or 40 ppm Cl_2 in N_2 (Gasco) as the reagent Cl_2 sources. A critical orifice limited Cl_2 flows at 10 sccm from the 12 L glass; flow from the Cl_2 cylinders was adjusted by a precision needle valve. We used N_2, mixtures of N_2 and O_2 (99.994%; Airgas), or ultra-zero air (UZA; 99.999%; Airgas) as carrier gases for the Cl_2 reagent mixture. Needle valves controlled total carrier gas flow at >1250 mL/min, which diluted Cl_2 mixing ratios to ≤ 1 ppm in the ionizer. Unless otherwise stated, we used ~100 ppb Cl_2 in UZA carrier gas for Cl_2-CIMS reagent ion generation.

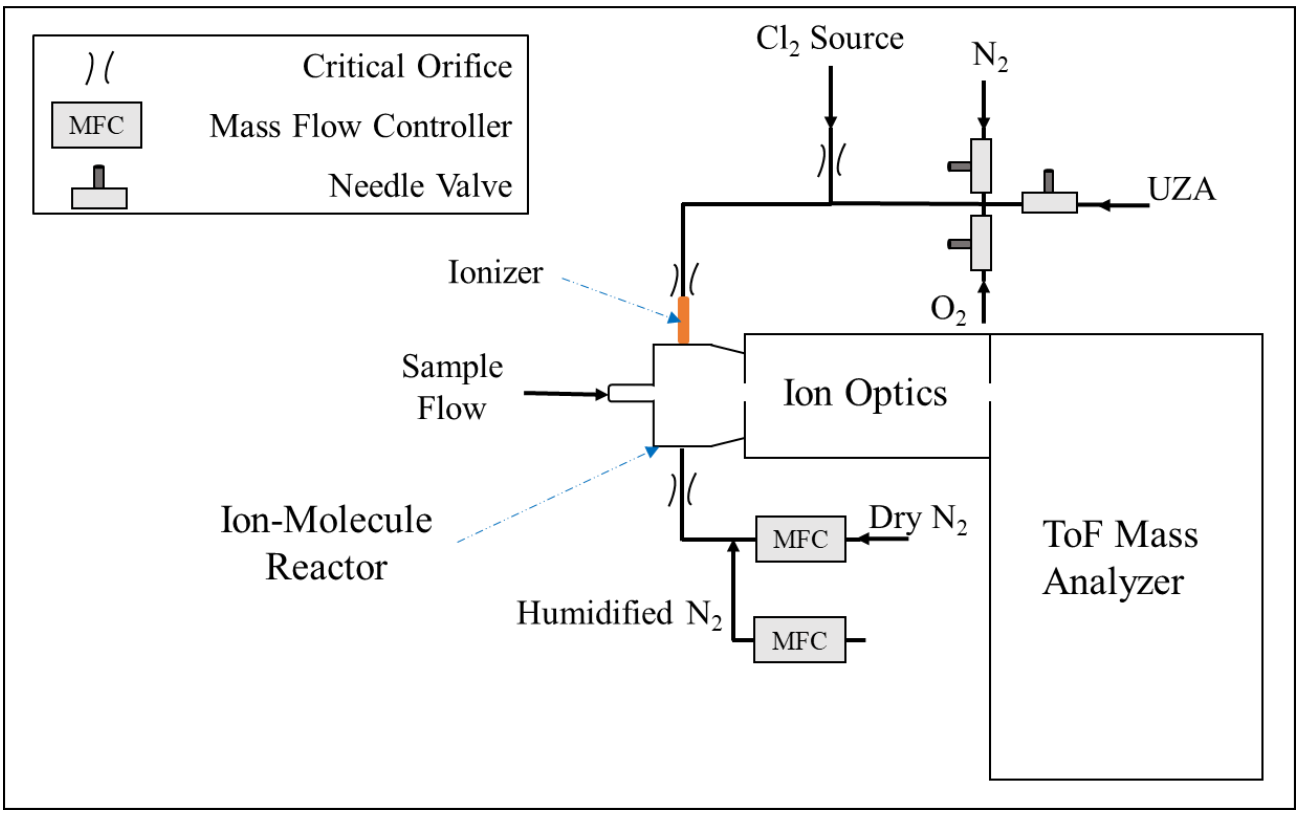

Figure 4.i Schematic of flows to introduce Cl_2^- reagent ions into the IMR of the CIMS. Describes the major CIMS components and the ionizer; flows of Cl_2, N_2, humidified N_2, zero air, and oxygen; and sample flow.

For I-CIMS, we generated I^- by passing a constant flow of N_2 over a CH_3I permeation tube heated to 40 °C through the ionizer. We control water vapor partial pressure in the IMR through an additional port by changing the ratio of dry and water-saturated N_2 while keeping total flow constant. The humidified line was typically maintained at 80% RH, providing ~0.5 mbar H_2O to the IMR. The ion optics consist of one small quadrupole and one large quadrupole, plus multiple skimmers and a segment of ion lenses, operated at increasing voltage (in this case, increasing negative voltages) as sample air moves from the high- to low-pressure regions. The ion optics maximize ion transport efficiency through the instrument as the total pressure reduces from 65 mbar in the IMR to 1×10^{-6} mbar in the time-of-flight region. The time-of-flight mass analyzer had a mass resolution of 3500 m/Δm (Δm = 0.04 at m/z 144.95, the m/z for $Cl_2(CH_3C(O)O_2)^-$),

adequate for determining the elemental composition of detected ions in the size range described here.

4.3.2 Calibrations

We calibrated the Cl_2-CIMS for ozone (O_3), formic, acetic, propanoic, and isobutyric acids, and $CH_3C(O)O_2$. A calibrated O_3 source (Model 306, 2B Technologies) generated O_3 between 25-200 (±2.0%) ppb in a 1600 mL/min flow of air, which we diluted with UZA to 2 L/min before sampling by the Cl_2-CIMS. Custom permeation tubes containing liquid organic acids were held at 40 °C and served as the acid calibration source. We used a PAN source[74] for CIMS calibration to $CH_3C(O)O_2$. The PAN calibration source photolyzes acetone in UZA to form $CH_3C(O)O_2$ and CH_3O_2. These radicals then react with NO to form NO_2, $CH_3C(O)O$ and CH_3O. The NO_2 reacts with the remaining $CH_3C(O)O_2$, producing a 60 mL/min flow containing 40 ppb of PAN. We diluted this PAN flow into 2 to 5 L/min N_2 and thermally decomposed peroxyacetyl nitrate (PAN) at 150 °C to produce $CH_3C(O)O_2$ mixing ratios from 0.48 to 0.96 ppb. A heating rope around a 0.25" O.D. glass sampling tube 1 cm from the CIMS inlet provided the necessary heating for PAN thermal decomposition.[57] We calibrated the Cl_2-CIMS to analytes at a Cl_2 reagent mixture concentration of 100 ppb. Sensitivities are reported for IMR water partial pressure of 0.5 mbar and a total pressure of 65 mbar. All calibration standards were measured by the Cl_2-CIMS as a function of (i) Cl_2 ionizer concentrations (0.1 to 1.5 ppm), (ii) ion-molecule reactor (IMR) pressure between 50 and 100 mbar, (iii) IMR water partial pressure between 0 and 0.8 mbar, and (iv) de-clustering potential[97] between the front of the second quadrupole and the adjacent (up-flow) skimmer plate (Appendix D.i).

Sensitivities were calculated as the slope of the line of detected ion signal versus input concentration and reported as normalized ion counts per second per part per trillion (ncps/ppt).

Unless indicated otherwise, Cl_2-CIMS signals are normalized to the sum of Cl^-, Cl_2^-, Cl_3^- , and O_2^- . Limits of detection (1 s integration) are calculated as three times the background signal-to-noise ratio and assuming a Poisson distribution for background count rates.[49,57]

4.3.3 Ketone photolysis product quantum yields

To evaluate whether Cl_2^- was a better reagent ion for laboratory radical measurements, we compared measurements of $CH_3C(O)O_2$ and propionyl peroxy radicals ($C_2H_5C(O)O_2$), generated from photolysis of acetone and methyl ethyl ketone (MEK), acquired with Cl_2-CIMS versus I-CIMS. In these experiments, ketone photolysis generated acyl peroxy radicals (R1a and R1b):

$$RC(O)CH_3 + hv \rightarrow RC(O) + CH_3 \qquad \text{R1a}$$

$$RC(O) + O_2 + M \rightarrow RC(O)O_2 \qquad \text{R1b}$$

We produced the MEK and acetone standards in 12 L glass bulbs containing percent-level ketone in N_2 taken from the headspace of purified liquid ketones. Ketone samples in vacuum storage flasks were purified by freezing the liquid and pumping out the headspace. Ketone bulb concentration was determined through absorbance of 254 nm light (Hg Pen-Ray lamp; Analytik Jena) in a 50 cm glass cell with quartz end windows. We measured absorbance by bulb contents relative to background intensity in dry N_2 in triplicate, using a lab-built photodiode detector.

The photolysis reactor was a 1” O.D. glass tube with three 0.25” O.D. ports for the addition of photolyte mixture and sampling by the CIMS and exhaust. A Hg Pen-Ray 254 nm lamp was inserted 3” into the reactor in a 0.5” O.D. quartz test tube. The CIMS sampled from the photolysis reactor 1 cm from the end of the Pen-Ray lamp through an inserted 0.25” glass tube.

During photolysis experiments, 10 mL/min of ketone in N_2 was mixed with 7 L/min of 21% O_2 in N_2 before entering the reactor adjacent to the Pen-Ray lamp housing. We measured the background flow of O_2 and N_2 before turning on the Pen-Ray Lamp for 100 sec and then adding

the ketone. After sampling during ketone photolysis for 5 min, we turned off the lamp, turned off the ketone flow, and sampled for at least one minute before turning the lamp on again. Experiments were run with both acetone and MEK. The Cl_2-CIMS detected $CH_3C(O)O_2$ primarily as the cluster $Cl_2(CH_3C(O)O_2)^-$ (R2).

$$CH_3C(O)O_2 + Cl_2^- \rightarrow Cl_2(CH_3C(O)O_2)^- \qquad \text{R2}$$

By maintaining constant photolysis reactor conditions over the course of the experiment, we determined MEK photolysis product quantum yields from the ratio of $Cl_2(RC(O)O_2)^-$ signals between the two photolysis steps without needing to consider the reaction time of photon flux components of the photolysis rate coefficient equation (E1).[57]

$$\Phi_{254}^{MEK,RC(O)O_2} = \frac{S_{Cl_2(CH_3C(O)O_2)^-}[Acetone]\sigma_{254}^{Acetone}\Phi_{254}^{Ac,CH_3C(O)}}{S_{Cl_2(RC(O)O_2)^-}[MEK]\sigma_{254}^{MEK}} \qquad \text{E1}$$

where S represents the Cl_2-acylperoxy radical cluster ion signals produced during photolysis steps (Hz), σ and φ are the terms for ketone 254 nm absorption cross section and RC(O) quantum yield, respectively, and [Acetone] and [MEK] are the ketone concentrations in the photolysis reactor.

4.3.4 Woodsmoke experiments

The Cl_2-CIMS sampled woodsmoke from a 1 m^3 Teflon chamber that had ports for air sampling, injection of smoke, and a constant flow of 3 L/min zero air (produced by zero air generator; Model 7000, Environics). Following the method described in Li et al.,[98] we burned ~1 g of Douglas fir woodchips in a Breville (BSM600SILUSC) cocktail smoker and injected the smoke directly into the chamber. This injection produced approximately 300 μg/m^3 of smoke aerosol along with concentrated gases that could be analyzed by the CIMS. We connected the CIMS to a sampling port through ~1 m of PFA tubing (0.25" O.D.) with a PTFE filter to remove particles. A manual three-way valve allowed zero air to bypass the chamber directly to the CIMS. During measurements, we first flowed only zero air into the chamber for a background

measurement before injecting smoke. The CIMS sampled smoke from the chamber for 2 hours with Cl_2-CIMS before switching to I-CIMS mode. For analysis of woodsmoke samples, we identified ions that increased during smoke sampling with m/z < 300 for Cl_2-CIMS and < 350 for I-CIMS.

4.4 Results and Discussion

4.4.1 Analyte detection

The Cl_2-CIMS produced ions through a variety of mechanisms including proton abstraction; adduct formation with Cl^-, Cl_2^-, and O_2^-; charge transfer; and secondary chemistry (Table 4.a; Appendix D.ii). Little fragmentation was observed. The dominant product ion varied by analyte. Cl_2^- cluster ions provided the largest sensitivity for formic acid and $CH_3C(O)O_2$, while product ions from secondary chemistry and O_2^- clustering provided the largest sensitivities for O_3 and C_2-C_4 organic acids, respectively. Though C_2-C_4 organic acids were detected as O_2^- clusters with sensitivities on the order of 1 to 2 ncps/ppt, Cl_2^- clusters produced much lower sensitivities at <0.02 ncps/ppt. C_2-C_4 organic acid clusters with Cl^- showed similar sensitivity to O_2^- at 1.2 ± 0.2 ncps/ppt for acetic acid, 0.215 ± 0.002 ncps/ppt for propanoic acid, and 0.142 ± 0.005 ncps/ppt for isobutyric acid.

Table 4.a Analyte product ion detection and sensitivities

Analyte	Molecular Formula	Product Ions	Primary Product Ion	Primary Ion Sens. (ncps/ppt)[a]	LOD (ppt)	Range (ppb)
Acetyl Peroxy Radical	$CH_3C(O)O_2$	$Cl_2CH_3C(O)O_2^-$	$Cl_2CH_3C(O)O_2^-$	2.30±0.04 3.19±0.05[b]	5	0.48 - 0.96
Ozone	O_3	O_3^-, CO_3^-	CO_3^-	0.78±0.02	291	18.4 - 147
Formic Acid	HC(O)OH	$ClRC(O)OH^-$, $Cl_2RC(O)OH^-$, $O_2RC(O)OH^-$, $RC(O)O^-$ [c]	$Cl_2HC(O)OH^-$	1.01±0.02	73	33 - 65
Acetic Acid	$CH_3C(O)OH$		$O_2CH_3C(O)OH^-$	1.6±0.2	50	23 - 46
Propanoic Acid	$C_2H_5C(O)OH$		$O_2C_2H_5C(O)OH^-$	2.00±0.01	9	8.7 - 17.2
Isobutyric Acid	$C_3H_7C(O)OH$		$O_2C_3H_7C(O)OH^-$	1.11±0.01	22	0.97 - 1.9

[a]Sensitivities normalized (per million ions) to sum of reagent ion signal (O_2^- + Cl^- + Cl_2^- + Cl_3^-).
[b]Sensitivity normalized (per million ions) to Cl_2^- signal.
[c]General formulas of observed product ions for all organic acids.

Sensitivities to all analytes were independent of IMR pressure within the range of 50-100 mbar (Appendix D.iii) but did vary with IMR water partial pressure (0-0.6 mbar; Appendix D.iv and D.v), and de-clustering voltage (Appendix D.vi). The largest water partial pressure impacts were observed for Cl^- and Cl_2^- clusters. Thus, we operated the Cl_2-CIMS optimized for $Cl_2(RC(O)O_2)^-$ (~0.5 mbar H_2O) and overall cluster ions production (dV = 1.4).

Sensitivity to $CH_3C(O)O_2$, detected as $Cl_2(CH_3C(O)O_2)^-$, was 2.30 ± 0.04 ncps/ppt when normalized to the total reagent ion signal, and 3.19 ± 0.05 ncps/ppt when normalized to the Cl_2^- reagent ion signal. In contrast to other analytes, alternate ion formation pathways were negligible for the acetyl peroxy radical. The sensitivity of Cl_2-CIMS was higher than that for I-CIMS (1.54 ± 0.03 ncps/ppt for $CH_3C(O)O_2$) under the same measurement conditions. However, the LOD for I-CIMS was lower (2 ppt) than we obtained for Cl_2-CIMS (5 ppt) due to larger backgrounds for Cl_2-CIMS.

We note that CIMS users employ various normalization techniques; either normalizing data to total ion counts to account for slight variations in instrument performance, or normalizing data to the relevant reagent ion signals acknowledging that variations in just those signals can modulate the sensitivity to an analyte.[96,99,100] Different approaches to normalization impact the calculated sensitivity and detection limit. For example, we add a second Cl_2-CIMS sensitivity to $CH_3C(O)O_2$ (normalized to the Cl_2^- counts only) in Table 4.a and Appendix D.vii, due to a consistent relationship between Cl_2^- and $Cl_2(CH_3C(O)O_2)^-$ observed during $CH_3C(O)O_2$ calibration and MEK photolysis (Appendix D.viii). This normalization method increased the normalized sensitivity, but the total sensitivity observed during the test remains the same. The Cl_2-normalized sensitivity serves as both the maximum possible sensitivity in a reagent ion spectrum of entirely Cl_2^- and the most accurate method of calculating sensitivity to $CH_3C(O)O_2$ between tests. The $CH_3C(O)O_2$ sensitivity normalized to the sum of Cl^-, Cl_2^-, Cl_3^-, and O_2^- did not reflect the difference of signal observed between Cl_2- and I-CIMS during MEK photolysis.

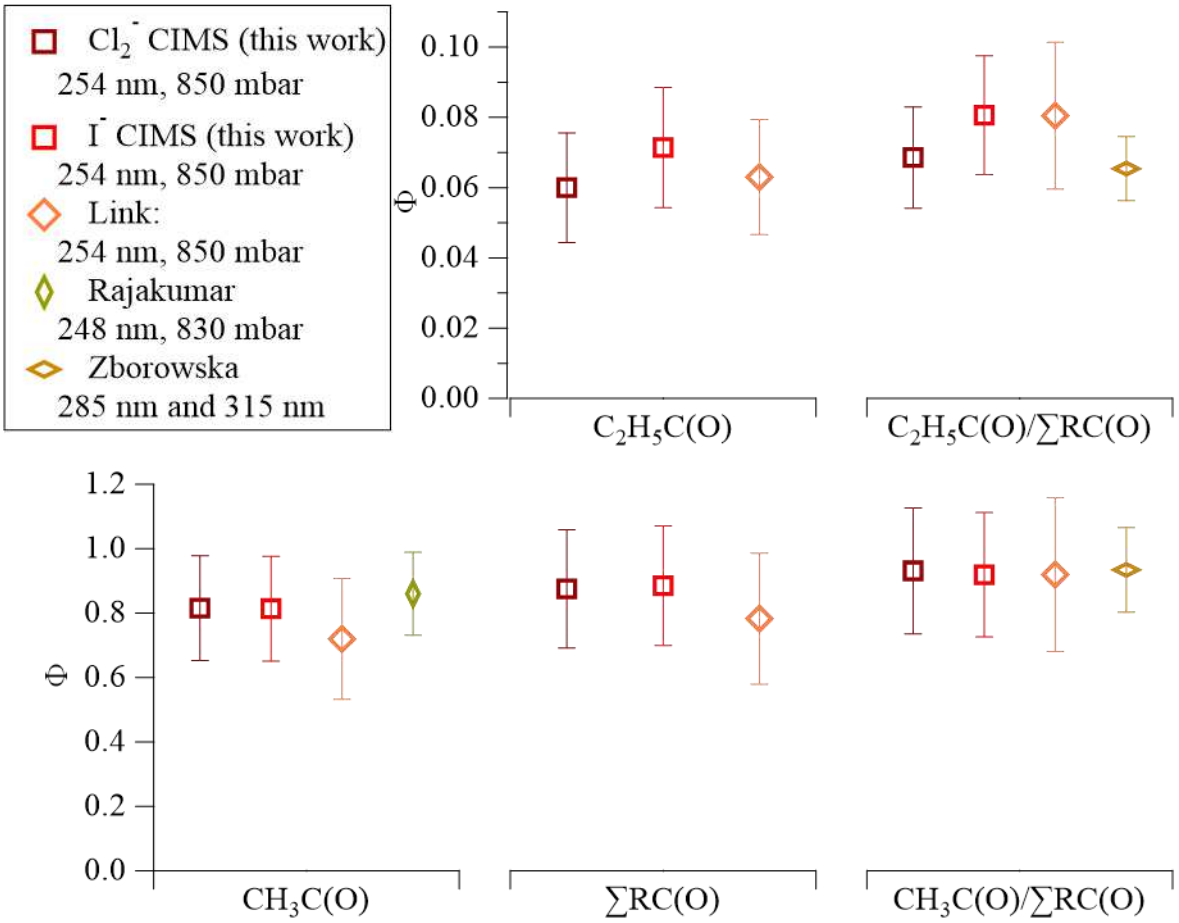

Figure 4.ii Comparison of MEK photolysis product quantum yield values from the Cl_2-CIMS (dark red) and I-CIMS (light red) from this study to recent literature values. The x-axis consists of segments for each MEK photolysis product: $CH_3C(O)$ on the bottom-left, $C_2H_5C(O)$ on top-center, ΣRC(O) on the bottom-center, and branching ratios on the right ($C_2H_5C(O)$/∑RC(O) top; ($CH_3C(O)$/∑RC(O) bottom) Orange diamonds represent values from Link et al.;[57] gold diamond represents the Rajakumar et al.[35] value for $\Phi_{CH_3C(O)}$; light-brown diamonds represent branching ratios derived from $C_2H_5C(O)$:$CH_3C(O)$ signal ratios in Zborowska et al.[41] Error bars represent experimental uncertainties.

4.4.2 MEK photolysis product quantum yield measurements at 254 nm

The Cl_2-CIMS detected both $CH_3C(O)O_2$ and $C_2H_5C(O)O_2$ from MEK photolysis as clusters with Cl_2^-. We assume that the Cl_2-CIMS sensitivity to $CH_3C(O)O_2$ and $C_2H_5C(O)O_2$ are equivalent based on voltage scanning data. Briefly, by changing the voltage difference between two components in the ion-focusing regions of the CIMS, we provide adequate energy to de-cluster reagent ion-analyte adducts.[97,101] The voltage difference that corresponds to a 50% loss in adduct

ion signal (dV50) correlates to the sensitivity of the instrument to the clustering mechanism.[73] The voltage scan provides a dV50 of 4.6 V for $Cl_2(CH_3C(O)O_2)^-$ and 4.2 V for $Cl_2(CH_3C(O)O_2)^-$ (Appendix D.ix). This is quite close to the 0.3 V difference in dV50 found with I-CIMS,[57] indicating that the sensitivities of Cl_2-CIMS to $CH_3C(O)O_2$ and $C_2H_5C(O)O_2$ are similar. This assumption is further supported by the agreement of quantum yields between Cl_2-CIMS and I-CIMS and with prior literature.

Cl_2-CIMS derived MEK photolysis quantum yields at 254 nm ($\Phi_{254}^{MEK,RC(O)}$) were consistent with previous measurements and with I-CIMS $\Phi_{254}^{MEK,RC(O)}$ obtained as part of this work. $\Phi_{254}^{MEK,CH_3C(O)}$ and $\Sigma\Phi_{254}^{MEK,RC(O)}$ from Cl_2-CIMS and I-CIMS (Figure 4.ii) agreed within the measurement precision of 3%, while $\Phi_{254}^{MEK,C_2H_5C(O)}$ agreed within the experimental uncertainties of 26% and 24% calculated for Cl_2-CIMS and I-CIMS, respectively. The experimental uncertainties were 20% for $\Phi_{254}^{MEK,CH_3C(O)}$ and 21% $\Sigma\Phi_{254}^{MEK,RC(O)}$ for both Cl_2-CIMS and I-CIMS. Signals for $Cl_2(CH_3C(O)O_2)^-$ and $Cl_2(C_2H_5C(O)O_2)^-$ obtained by Cl_2-CIMS during MEK photolysis were larger than the corresponding I^- cluster signals from I-CIMS (Appendix D.viii). Cl_2-CIMS measured radical signals normalized to only Cl_2^- were a factor of 2.1 ± 0.1 larger than I-CIMS (normalized to the sum of I^- and $I(H_2O)^-$), in agreement with the sensitivity ratio (2.07 ± 0.05) obtained during calibrations. This indicates that the total Cl_2-CIMS sensitivities to $RC(O)O_2$ were dependent on Cl_2^- and not related to the total reagent ion count.

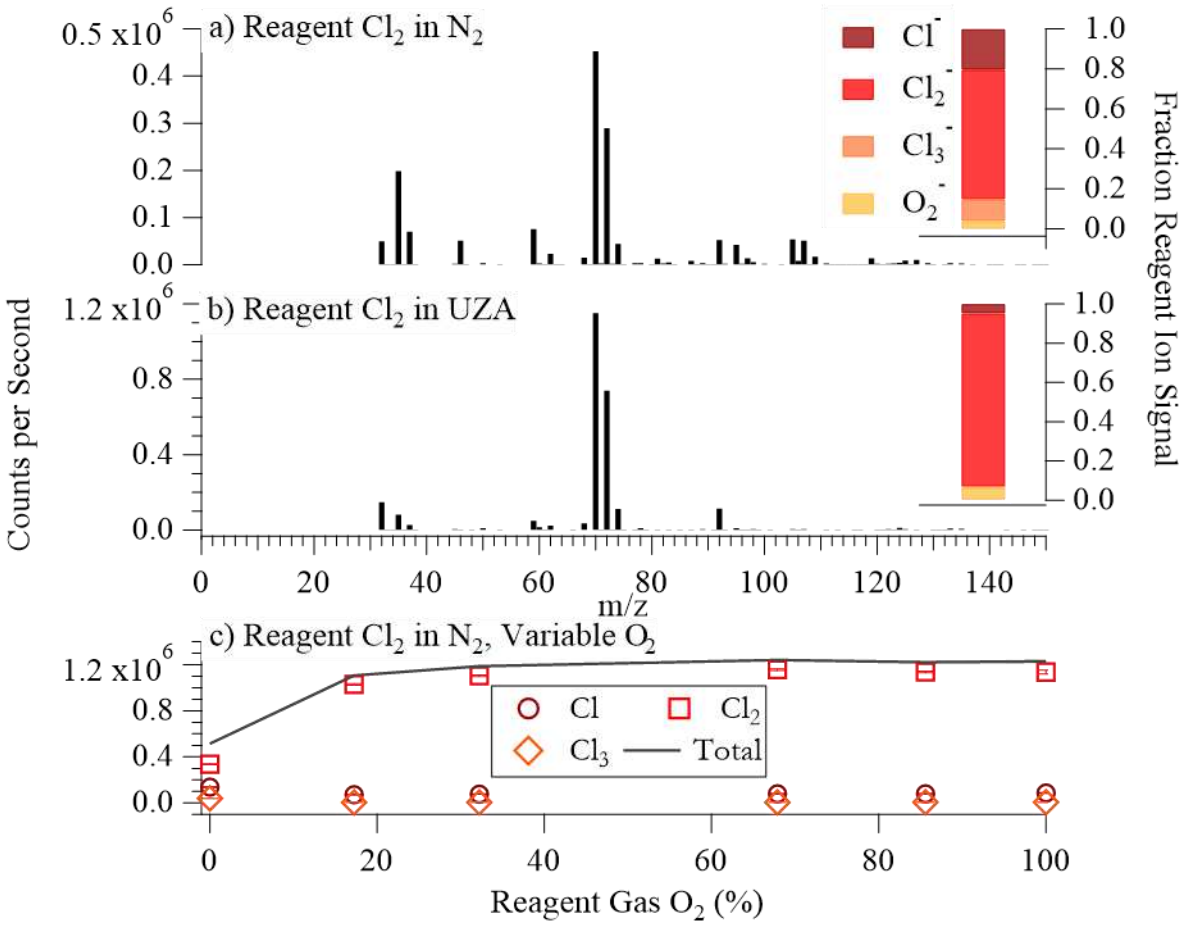

Figure 4.iii a) Mass spectrum for dry N_2 with a reagent ion flow of Cl_2 in N_2; fractional contributions of reagent ions (dark red: Cl^-, light red: Cl_2^-, orange: Cl_3^-, yellow: O_2^-) to total reagent ion counts in the right-hand inset. b) Mass spectrum for dry N_2 with reagent ion flow of Cl_2 in UZA and the respective fractional reagent ion contribution inset. c) Ion counts for Cl^-, Cl_2^- and Cl_3^- as a function of O_2 mixing ratio (%) in the reagent gas mixture (dry N_2 sampling). The black line represents the sum of these three ions.

4.4.3 Cl_2-CIMS reagent ion chemistry

Cl_2-CIMS reagent ion chemistry is a complex system of ionizing reactions involving Cl^-, Cl_2^-, Cl_3^-, and O_2^-, which is best described by first examining the ion chemistry of Cl_2 in N_2. In a reagent gas mixture with dry N_2, Cl_2 is the primary molecule that attaches free electrons within the ionizer flow (R3).

$$e^- + Cl_2 \rightarrow Cl_2^{-*} \qquad \text{R3}$$

Excited Cl_2^{-*} formed by electron attachment can decompose to Cl^- and Cl (R4a),[102] though the example reagent ion spectrum in N_2 (Figure 4.iii (a)) shows a significant portion of Cl_2^{-*} in our system is stabilized by collisions (R4b). Cl_2^{-*} is the source of both Cl^- and Cl_2^- in the reagent ion spectra through either decomposition or collisional stabilization.

$$Cl_2^{-*} \rightarrow Cl + Cl^- \quad \text{R4a}$$

$$Cl_2^{-*} + M \rightarrow Cl_2^- + M^* \quad \text{R4b}$$

$$Cl + Cl^- M \rightarrow Cl_2^- \quad \text{R5}$$

The recombination reaction (R5) is a significant source of Cl_2^- for liquid phase studies but is not expected to be important here.[103] Instead, Cl^- can go on to react with Cl_2, forming the observed Cl_3^- signal (R6a), with Cl_2^- + Cl_2 (R6b) and Cl_2^- + Cl (R6c) reactions also being possible sources of Cl_3^-.[104]

$$Cl^- + Cl_2 \rightarrow Cl_3^- \quad \text{R6a}$$

$$Cl_2^- + Cl \rightarrow Cl_3^- \quad \text{R6b}$$

$$Cl_2^- + Cl_2 \rightarrow Cl_3^- + Cl \quad \text{R6c}$$

We found an upper limit of 400 ppb Cl_2 in the reagent ion flow (Figure 4.iv (c)), above which point the Cl_2^- signal stopped increasing and Cl_3^- became the largest reagent ion signal. We were unable to isolate production of Cl_2^- through modulation of Cl_2 concentration in N_2 alone.

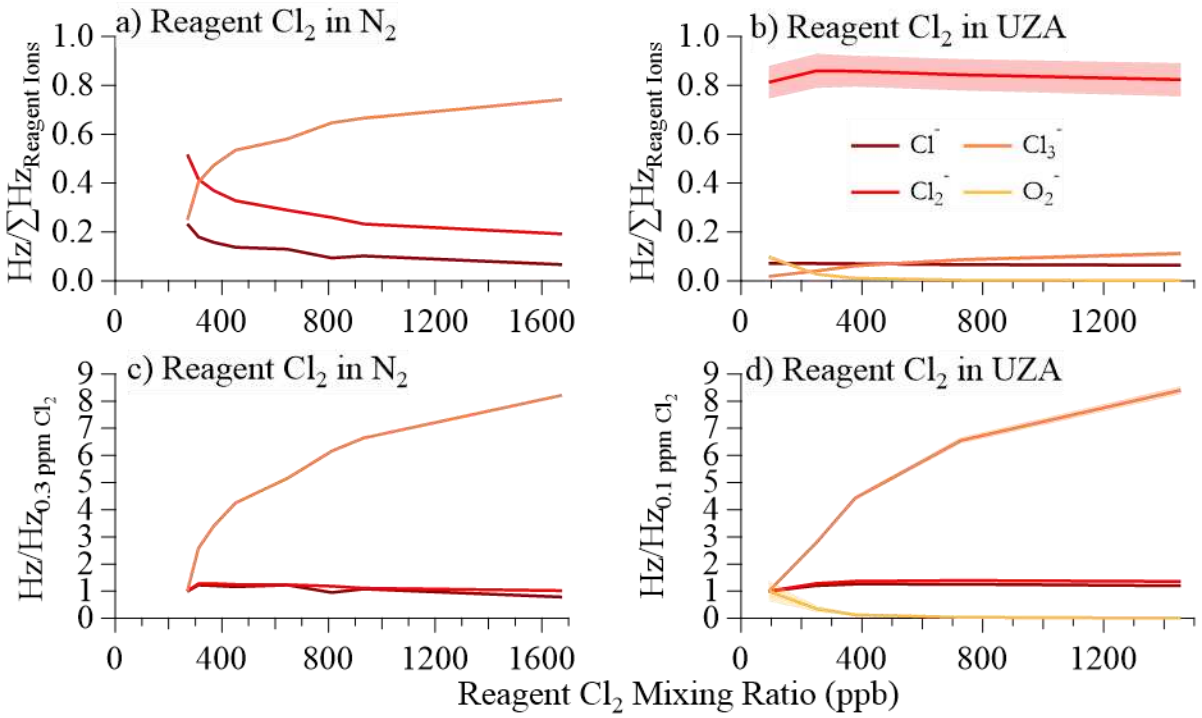

Figure 4.iv a) Fraction of total reagent ion signal for Cl^- (dark red), Cl_2^- (light red), and Cl_3^- (orange), as a function of reagent gas Cl_2 mixing ratio (ppb) in N_2. b) Fraction of total reagent ion counts for Cl^-, Cl_2^-, and Cl_3^-, and O_2^- (yellow) as a function of reagent gas Cl_2 mixing ratio in UZA. c) Reagent ion signal, relative to 300 ppb Cl_2, as a function of reagent gas Cl_2 mixing ratio in N_2. d) Reagent ion signal, relative to 100 ppb Cl_2, as a function of reagent gas Cl_2 mixing ratio in UZA. All reagent ion data was collected while sampling dry N_2 to the CIMS inlet.

4.4.4 Impacts of O_2 and Cl_2 concentrations

The reagent ion distribution changed with the addition of O_2 (Figure 4.iii (b and c)). Adding ~21% O_2 to the ionizer flow increased total ion counts by 58%, increased the fraction of Cl_2^- ions in the total reagent ion signal from 60 to 90%, reduced Cl^- and Cl_3^- signals, and increased O_2^-. Due to the direct dependence of $Cl_2(RC(O)O_2)^-$ on Cl_2^-, the net result of these changes was a factor of 2.4 increase in total sensitivity to $RC(O)O_2$. Addition of O_2 also caused a 32% decrease of non-reagent ions in background mass spectra, leading to overall improvements in LODs.

The differences we observed in the reagent ion spectrum upon addition of O_2 result from a change in the primary Cl_2 ionization mechanism. At percent-level concentrations in the reagent gas mixture, O_2 becomes the primary electron capturing molecule (R7).

$$e^- + O_2 \rightarrow O_2^- \quad \text{R7}$$

Cl_2^- is a known product of Cl_2 ionization by O_2-CIMS,[105] and we hypothesize Cl_2^- is primarily formed here in a multiple step process. Electrons formed by ionization in the Po-210 source may predominately attach to O_2 molecules present in the reagent gas mixture at atmospheric mixing ratios. The electron affinities of Cl_2 and O_2 are 2.38 eV[106] and 0.451 eV,[107] respectively, indicating the following favorable electron transfer reaction as the primary source of Cl_2^- with O_2 in the reagent gas mixture (R8).

$$O_2^- + Cl_2 \rightarrow O_2 + Cl_2^- \quad \text{R8}$$

The reagent ion distribution impacts the chemical ionization mechanisms and thus sensitivity. We found that modulation of Cl_2 reagent gas concentration in UZA produced a negative correlation between Cl_2^- and O_2^- (Figure 4.iv (d)). Analyte ions for the organic acids, O_3, and $CH_3C(O)O_2$ responded to either Cl_2^- or O_2^-, depending on which ion chemistry produced each ion. The sensitivity of these analyte ions to changes in the Cl_2 mixing ratio in the reagent gas mixture (in UZA) are shown in Figure 4.v, with the slopes and r^2 of the included linear least squares fits in Appendix D.x. Cl^- and Cl_2^- signals correlated well to both the Cl^- and Cl_2^- cluster analyte ions (r^2 > 0.73 for Cl^- and > 0.59 for Cl_2^-). The exceptions were $Cl_2(C_2H_5C(O)OH)^-$, which had low sensitivity, and $Cl_2(CH_3C(O)O_2)^-$ at Cl_2 concentrations above 400 ppb (Appendix D.xi). For Cl_2 reagent gas concentrations below 400 ppb, Cl_2^- correlated to $Cl_2(CH_3C(O)O_2)^-$ with slope = 0.53 and r^2 = 0.99. Fitting of O_2^- cluster and H^+ abstraction ion signals to Cl^- and Cl_2^- resulted in negative slopes for all sampled acids. We also observed negative Cl^- and Cl_2^- correlations for O_3^- and CO_3^- from O_3 and for $CH_3C(O)O^-$ and $CH_3C(O)O_2^-$ detected during $CH_3C(O)O_2$ sampling. The O_2^- clusters and H^+ abstraction products, instead, correlated strongly to O_2^- signal, as did O_3^-, CO_3^-

, and $CH_3C(O)O_2^-$ ($r^2 > 0.96$; slopes = 1.0). Changes in Cl_3^- signal did not correlate to any analyte ion, returning slopes between 0.09 and -0.15.

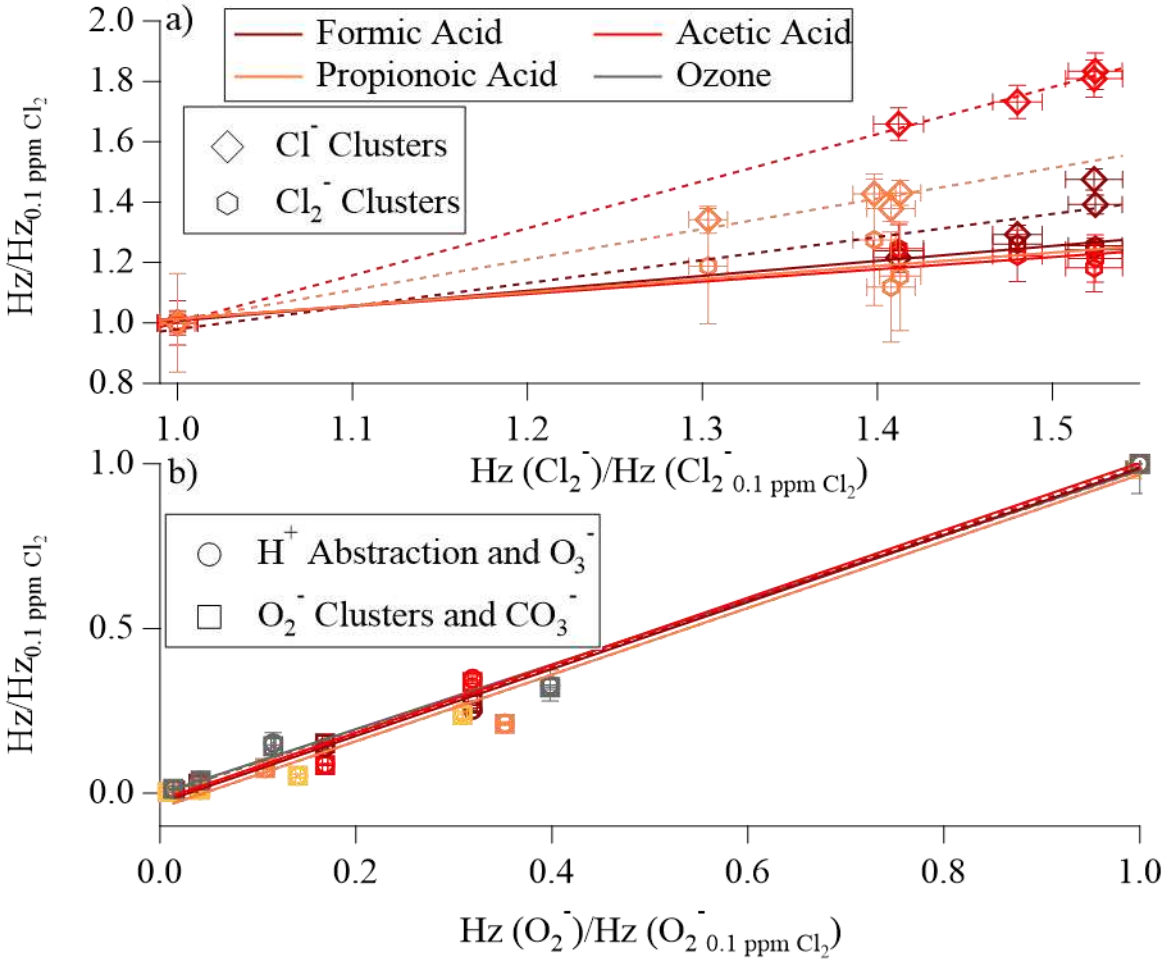

Figure 4.v a) Correlation plot of Cl^- (diamonds) and Cl_2^- (hexagons) cluster ion signals for formic (dark red), acetic (light red), and propionic (orange) acids against background signals of Cl_2^- over the Cl_2 concentration changes. Linear correlation fits shown with dashed (Cl^- clusters) and solid (Cl_2^- clusters) lines. b) Correlation plot of proton abstraction (circle) and O_2^- cluster (square) ion signals against background signals of O_2^- over the Cl_2 concentration changes. Acid signals are indicated by the same colors as (a), with gray markers for O_3 product ion correlations (squares for CO_3^- and circles for O_3^-). Linear fits are shown as dashed lines for proton abstraction and solid lines for O_2^- cluster. The y-axis represents ratios of the observed signal to the signal at the lowest Cl_2 concentration; all error bars represent propagated uncertainty of one standard deviation in signal at each Cl_2 concentration step. Isobutyric acid is left off to reduce graph clutter, as these signals had large uncertainty for Cl_2^- reactions. Fit information for isobutyric acid is provided in Appendix D.x and D.xii.

The formation of Cl^- clusters from Cl^- ionization is straightforward. However, Cl^- cluster formation from Cl_2^- is also possible, due to the instability Cl_2^-. Here, the reaction between Cl_2^- and an analyte would act more like a ligand exchange, producing Cl-analyte ion and a Cl atom (R9).

$$Cl_2^- + RC(O)OH \rightarrow Cl + (RC(O)OH)Cl^- \qquad \text{R9}$$

A similar ionization mechanism occurs with SF_6^- for some analytes.[47] Cl_3^- formation acts as a sink of sensitivity in the Cl_2-CIMS, as Cl_3^- signal did not show a positive correlation with any analyte ion. Cl_3^- is a cluster ion of Cl_2 and Cl^-, which has a high binding energy.[108] This binding energy was larger than that of the acid-Cl^- clusters (Appendix D.vi). In addition, Cl_3^- has an electron affinity ≥ 3.8 eV,[104] making electron transfer ionization unfavorable for most analytes.

4.4.5 Woodsmoke

While Cl_2-CIMS is an effective detection technique for peroxy radicals in controlled laboratory systems, woodsmoke demonstrates the problems of using Cl_2-CIMS for complex mixtures. We use ion mass defects (defined as the difference between the exact m/z of an ion and the nearest unit mass) to visualize the differences in ions that appear in the Cl_2-CIMS and I-CIMS mass spectra during woodsmoke experiments. Multiple reagent ions and potential reaction pathways produced more analyte ions with Cl_2-CIMS (>300 ions; Figure 4.vi (a)). The I-CIMS spectra contained about half as many ions, which were mostly produced from iodide adduct formation (177 ions; Figure 4.vi (b)). Though more peaks appeared for Cl_2-CIMS, these were not indicative of compounds unique to Cl_2-CIMS detection. Instead, the larger peak count in Cl_2-CIMS is a byproduct of multiple reagent ion chemistries, where a single analyte formula would appear in up to four product ions. We fit 103 Cl_2^- cluster analyte ions, which represented 39.8% of analyte ion signals measured with Cl_2-CIMS. 82 Cl^- clusters accounted for 21.6% of analyte ion signals, while 38.6% of analyte

signal was from 128 ions which did not contain Cl. In contrast, the 111 identified I^- containing ions accounted for 99.8% of analyte signals measured with I-CIMS.

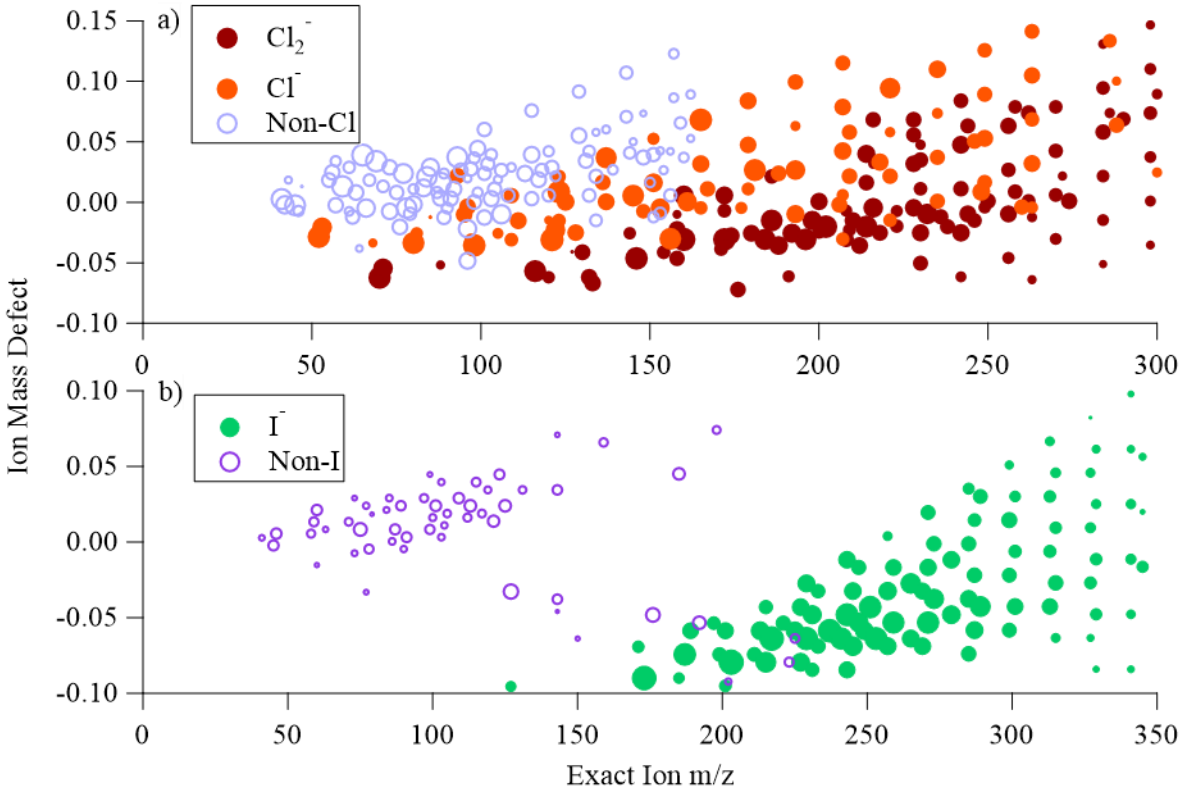

Figure 4.vi a) Mass defect plot for identified ions from woodsmoke sampling with Cl_2-CIMS. Blue circles indicate O_2^- cluster and non-clustered product ions, orange indicates Cl-containing, and red indicates Cl_2-containing formulas. b) Mass defect plot for detected ions during I-CIMS sampling of woodsmoke. Purple circles indicate peaks that did not contain iodide while green indicates I-containing formulas. Dot size represents the relative signal increase between background and smoke sampling steps.

The appearance of Cl_2^-, Cl^-, O_2^- clusters, and molecular ions (or H^+ abstraction products) led to an array of possible mass defects. Overlap of ions at the same mass-to-charge occurred more frequently for Cl_2-CIMS. I-CIMS provided I^- clusters with large mass defects and a lack of competing ion-molecule reactions. Thus, ions detected by I-CIMS were more often separated from interfering peaks than those detected by Cl_2-CIMS.

4.5 Conclusion

Direct measurement of RO_2 in both ambient and laboratory settings requires low limits of detection (1 ppt) and fast time resolution (≤ 1 s). Cl_2-CIMS is an effective reagent ion chemistry for laboratory measurement of $CH_3C(O)O_2$ and $C_2H_5C(O)O_2$ with better sensitivity than existing I-CIMS measurements – capable of producing quantum yields for MEK photolysis consistent with results obtained from other measurement techniques in the literature. The sensitivity of Cl_2-CIMS to $CH_3C(O)O_2$ and $C_2H_5C(O)O_2$ would be increased through isolation of Cl_2^- ionization chemistry, without the non-selective ionization of O_2^- or the potential for secondary chemistry of Cl atoms in the IMR. Such alterations to Cl_2-CIMS would also expand its applications. With the current instrumental design, the multiple reagent ion chemistries present in the Cl_2-CIMS system prevent the instrument from being useful for ambient studies, as evidenced by the woodsmoke measurements. Alternatively, this work highlights the utility of dual reagent ions (Cl_2^- and O_2^-) to provide a selective measurement of acyl peroxy radicals in such a way that the individual reagent ions could not.

CHAPTER 5: CONCLUSION

Following the first measurements of free troposphere OH concentrations in the 1990s, agreement between measured and modelled radical concentrations has improved. The models were improved by the inclusion of critical organic trace gas photolysis sources, including aldehydes, peroxides, and acetone. However, the uncertainty in these models is signficant (~40%), with persistent underestimation of radical concentrations near the tropopause. I believe the need for better techniques, like CIMS, for measurements of organic trace gas photolysis is defined well by the following quote from Brune et al.[10]

"For the past two decades, measurements and models of OH and HO2 have gone through cycles of field deployment, discovery, re-evaluation, and improvement. All the while, the understanding of atmospheric oxidation in the free troposphere has expanded and confidence in it has grown. At some time, model atmospheric chemistry mechanisms may be tested well enough that OH and HO_2 measurements will no longer be a critical component of field deployments, but now is not that time."

To better our understanding of the mechanisms that produce radicals throughout the troposphere will undoubtedly require study of molecules, which, like acetone, have complex photolysis mechanisms. The studies presented in this dissertation demonstrate that CIMS will be an invaluable tool in the study of complex photochemical systems. CIMS can be used to identify not only the photolysis rates of organic gases but also product rates and identities of the product radicals. The photolysis quantum yield and identity of radicals are critical to our understanding of the chemistry that occurs after photolysis. Without reliable measurements of $\Phi_{CH_3C(O)}$ from acetone photolysis, as those presented here, models may still be able to determine the total radical production but could say little about acetone's contributions to global PAN production, which is estimated at approximately 7%.[20]

The results of using I-CIMS methods in chapters 2 and 3 provide $\Phi_{CH_3C(O)}$ from acetone photolysis measured only over conditions applicable to the troposphere. The I-CIMS enabled measuring $CH_3C(O)O_2$, the primary radical product of acetone photolysis in the troposphere, without the need for relying on complex secondary chemistry or waiting for the radical reactions to form stable final products. In this way, the measurements provide greater information on acetone photolysis in the troposphere than prior methods. Our $\Phi_{CH_3C(O)}$ data suggest slower acetone photolysis in the upper troposphere than previously thought and a slightly lower contribution to radical production. Inclusion of this slower acetone photolysis rate into models would increase the disagreement with free troposphere radical measurements, indicating that more photolytic sources of radicals need to be evaluated or the concentrations of ketones in the upper troposphere need to be reassessed. The data also provide valuable insights into the photophysics of carbonyl photolysis. For example, it demonstrates a clear and impressive impact of thermalized triplet energy state photolysis in acetone, which maintains a finite value for $\Phi_{CH_3C(O)}$ much larger than previous recommended quantum yields as excitation wavelengths approach the photolysis threshold. The impact of this increase in $\Phi_{CH_3C(O)}$ from 315 to 338 nm is minor for acetone, but the mechanism behind it must be evaluated for other organic gases, specifically carbonyl compounds.

The greatest advantage provided by CIMS is one that is not as critical for acetone photolysis but would be for larger ketones: CIMS can detect multiple photolysis products in some photolysis systems. This is demonstrated in both the I-CIMS and Cl_2-CIMS measurements of $\Phi_{CH_3C(O)}$ and $\Phi_{C_2H_5C(O)}$ in MEK photolysis and further in Figure 5.i. Separation of the signals produced by RC(O) of different structures is difficult for other methods and few methods other than CIMS can do so in real time. The data presented in Figure 5.i represents the (once) largest dataset of MEK branching ratios in terms of wavelength, which was produced in less than a full

day of measurements. Soojin Lee worked with the Farmer Lab on further measurements of MEK photolysis quantum yields under atmospheric conditions, for an upcoming publication on the possible impacts of MEK photolysis production of radicals in the free troposphere.

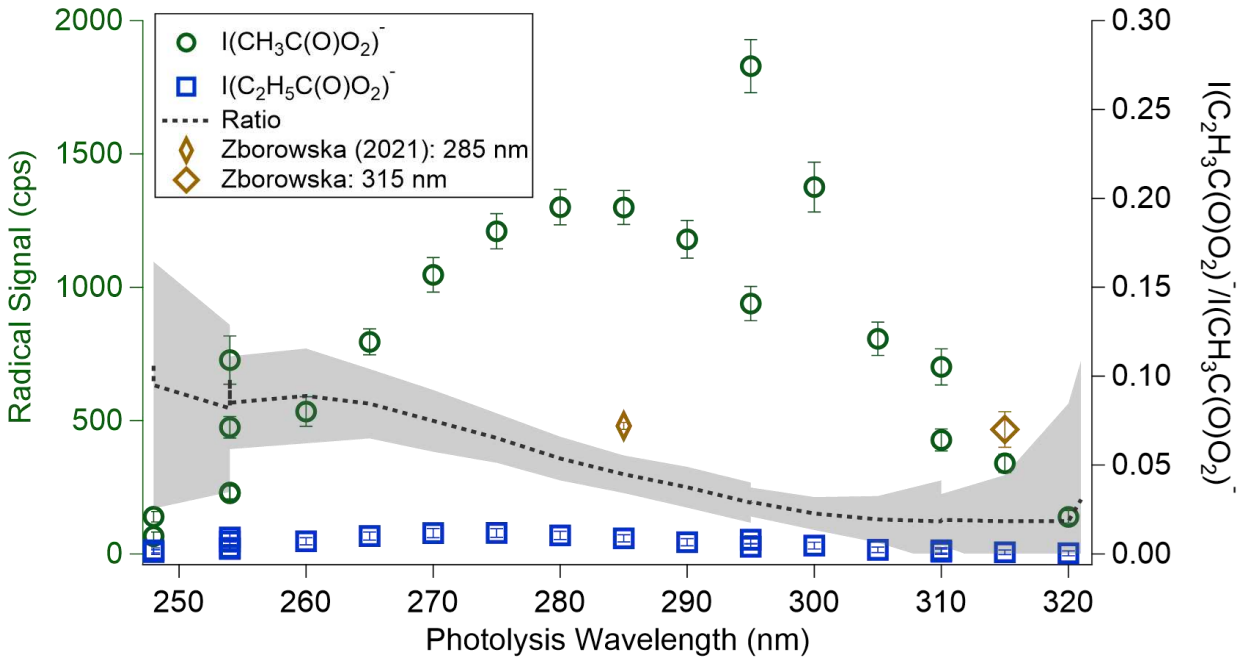

Figure 5.i Branching ratio for $I(C_2H_5C(O)O_2)^-/I(CH_3C(O)O_2)^-$ (gray dashed line, right axis) in the photolysis of MEK as a function of wavelength at 298 K and 850 mbar. This data was collected using the instrument design described in Chapter 2. Analyte ion signals are presented on the left axis for $I(CH_3C(O)O_2)^-$ (green circles) and $I(C_2H_5C(O)O_2)^-$ (blue squares) as 1-min averages of signal at each wavelength. Error bars for signals represent 1σ standard deviation. The shaded area for the branching ratio is the propagated signal uncertainty. Measurements taken at 2-3 MEK concentrations for 248, 254, 295, and 310 nm. Data is compared to limited wavelength branching ratios from Zborowska et al. (gold diamonds, right axis), measured under similar conditions.

The future uses for CIMS in photochemical measurements are not limited to trace gases that impact only free tropospheric photooxidation. The methods described here are well suited to study the ground-level photochemistry of α,β-diketones, such as biacetyl,[109,110] 2,3-pentadione, and 2,3-hexadione.[111] These are industrial emissions which are expected to photolyze quickly under visible wavelengths, but studies of their photolysis are limited. CIMS could be used for these

photochemical systems and others to address uncertainties in radical sources (and impacts on O_3 pollution) at the Earth's surface.

The work on Cl_2-CIMS demonstrates the possibilities of further CIMS development for measurements of photochemical properties and detection of organic peroxy radicals in the laboratory and ambient settings. Based upon the improved sensitivity provided by Cl_2-CIMS, this reagent ion system is likely better for measuring $CH_3C(O)O_2$, $C_2H_5C(O)O_2$, and possibly other small acyl peroxy radicals than I-CIMS. With the larger background interferences in Cl_2-CIMS and current uncertainties in the reagent ion chemistry, that would require further development of the system, which is outside the scope of the work described in Chapter 4. It is possible that use of an electron capturing gas other than O_2 would reduce background interferences for Cl_2-CIMS. However, implementation of pure air in place of N_2 for the reagent ion carrier is quite simple, and any other electron capturing species may come with its own reagent ion complexities, as with the mixture of O_2 and Cl_2. Instead, isolation of the Cl_2^- reagent ion chemistry may be achieved through modification of the ion-molecule reactor. Addition of a separate chamber for reaction of O_2^- and Cl_2 would allow this reaction to run to completion prior to sample introduction. This would also avoid passing Cl_2 through the ionizer, which may be the source of Cl^- and Cl_3^-. Other novel CIMS reagent ions may be investigated using the reagent ion source described in Chapter 4. For example, Br_2^- and I_2^- would be easily produced in the Cl_2-CIMS system by replacing Cl_2 with a source of either Br_2 or I_2. The multiple step ionization process opens the door for testing of new and possibly improved CIMS reagent ions for atmospheric studies. There remain ways to improve CIMS reagent ion techniques for both laboratory and ambient measurements of radicals.

The photolysis light source used in this study was a conventional CW light source. Replacing this light source with more intense narrow linewidth photon sources, such as LEDs and

lasers would allow studies at higher wavelength resolution. As shown earlier, even a simple mercury lamp was sufficient to measure quantum yields at 254 nm. With the advent of more narrow line width light sources and increasing the photon flux in the reactor would be a feasible step that can be undertaken in the coming years. Use of such light sources could also enable direct actinometry and avoid measuring only relative quantum yields.

Our studies demonstrate the power of using CIMS to detect peroxy radicals. This method can also be employed to study chemical processes in chambers that simulate the atmosphere. Furthermore, coupling this method with a flow tube reactor would allow studies of the kinetics of peroxy radicals.

In summary, we have shown that I-CIMS can be a powerful technique for studying peroxy radicals and has provided valuable information about the quantum yields in the photodissociation of acetone.

REFERENCES

(1) Atkinson, R.; Arey, J. Atmospheric Degradation of Volatile Organic Compounds. *Chem. Rev.* **2003**, *103* (12), 4605–4638. https://doi.org/10.1021/cr0206420.

(2) Heald, C. L.; Kroll, J. H. The Fuel of Atmospheric Chemistry: Toward a Complete Description of Reactive Organic Carbon. *Science* **2020**, *6.*

(3) Mellouki, A.; Wallington, T. J.; Chen, J. Atmospheric Chemistry of Oxygenated Volatile Organic Compounds: Impacts on Air Quality and Climate. *Chem. Rev.* **2015**, *115* (10), 3984–4014. https://doi.org/10.1021/cr500549n.

(4) Atkinson, R. Kinetics and Mechanisms of the Gas-Phase Reactions of the Hydroxyl Radical with Organic Compounds under Atmospheric Conditions. *Chem. Rev.* **1985**, *85*, 69–201.

(5) Atkinson, R. Atmospheric Chemistry of VOCs and NOx. *Atmos. Environ.* **2000**, No. 34, 2063–2101.

(6) Martins, D. K.; Stauffer, R. M.; Thompson, A. M.; Knepp, T. N.; Pippin, M. Surface Ozone at a Coastal Suburban Site in 2009 and 2010: Relationships to Chemical and Meteorological Processes. *J. Geophys. Res. Atmos.* **2012**, *117* (5), 1–16. https://doi.org/10.1029/2011JD016828.

(7) Shao, M.; Zhang, Y.; Zeng, L.; Tang, X.; Zhang, J.; Zhong, L.; Wang, B. Ground-Level Ozone in the Pearl River Delta and the Roles of VOC and NOx in Its Production. *J. Environ. Manage.* **2009**, *90* (1), 512–518. https://doi.org/10.1016/j.jenvman.2007.12.008.

(8) Liu, X.; Lyu, X.; Wang, Y.; Jiang, F.; Guo, H. Intercomparison of O_3 Formation and Radical Chemistry in the Past Decade at a Suburban Site in Hong Kong. *Atmos. Chem. Phys.* **2019**, *19* (7), 5127–5145. https://doi.org/10.5194/acp-19-5127-2019.

(9) Wennberg, P. O.; Hanisco, T. F.; Jaeglé, L.; Jacob, D. J.; Hintsa, E. J.; Lanzendorf, E. J.; Anderson, J. G.; Gao, R. S.; Keim, E. R.; Donnelly, S. G.; Del Negro, L. A.; Fahey, D. W.; McKeen, S. A.; Salawitch, R. J.; Webster, C. R.; May, R. D.; Herman, R. L.; Proffitt, M. H.; Margitan, J. J.; Atlas, E. L.; Schauffler, S. M.; Flocke, F.; McElroy, C. T.; Bui, T. P. Hydrogen Radicals, Nitrogen Radicals, and the Production of O_3 in the Upper Troposphere. *Science* **1998**, *279* (5347), 49–53. https://doi.org/10.1126/science.279.5347.49.

(10) Brune, W. H.; Miller, D. O.; Thames, A. B.; Allen, H. M.; Apel, E. C.; Blake, D. R.; Bui, T. P.; Commane, R.; Crounse, J. D.; Daube, B. C.; Diskin, G. S.; DiGangi, J. P.; Elkins, J. W.; Hall, S. R.; Hanisco, T. F.; Hannun, R. A.; Hintsa, E. J.; Hornbrook, R. S.; Kim, M. J.; McKain, K.; Moore, F. L.; Neuman, J. A.; Nicely, J. M.; Peischl, J.; Ryerson, T. B.; St. Clair, J. M.; Sweeney, C.; Teng, A. P.; Thompson, C.; Ullmann, K.; Veres, P. R.; Wennberg, P. O.; Wolfe, G. M. Exploring Oxidation in the Remote Free Troposphere: Insights From Atmospheric Tomography (ATom). *J. Geophys. Res. Atmos.* **2020**, *125* (1). https://doi.org/10.1029/2019JD031685.

(11) Gao, Y.; Lu, K.; Zhang, Y. Review of Technologies and Their Applications for the Speciated Detection of RO_2 Radicals. *J. Environ. Sci.* **2023**, *123*, 487–499. https://doi.org/10.1016/j.jes.2022.09.028.

(12) Orlando, J. J.; Tyndall, G. S. Laboratory Studies of Organic Peroxy Radical Chemistry: An Overview with Emphasis on Recent Issues of Atmospheric Significance. *Chem. Soc. Rev.* **2012**, *41* (19), 6294–6317. https://doi.org/10.1039/c2cs35166h.

(13) Singh, H. B.; Salas, L. J.; Chatfield, R. B.; Czech, E.; Fried, A.; Walega, J.; Evans, M. J.; Field, B. D.; Jacob, D. J.; Blake, D.; Heikes, B.; Talbot, R.; Sachse, G.; Crawford, J. H.; Avery, M. A.; Sandholm, S.; Fuelberg, H. Analysis of the Atmospheric Distribution,

Sources, and Sinks of Oxygenated Volatile Organic Chemicals Based on Measurements over the Pacific during TRACE-P. *J. Geophys. Res. D Atmos.* **2004**, *109* (15). https://doi.org/10.1029/2003JD003883.

(14) Singh, H. B.; Kanakidou, M.; Crutzen, P. J.; Jacob, D. J. High Concentrations and Photochemical Fate of Oxygenated Hydrocarbons in the Global Troposphere. *Nature* **1995**, *378* (6552), 50–54. https://doi.org/10.1038/378050a0.

(15) Haas, Y. Photochemical α-Cleavage of Ketones: Revisiting Acetone. *Photochem. Photobiol. Sci.* **2004**, *3* (1), 6–16. https://doi.org/10.1039/b307997j.

(16) McKeen, S. A.; Gierczak, T.; Burkholder, J. B.; Wennberg, P. O.; Hanisco, T. F.; Keim, E. R.; Gao, R.-S.; Liu, S. C.; Ravishankara, A. R.; Fahey, D. W. The Photochemistry of Acetone in the Upper Troposphere: A Source of Odd-Hydrogen Radicals. *Geophys. Res. Lett.* **1997**, *24* (24), 3177–3180.

(17) Neumaier, M.; Ruhnke, R.; Kirner, O.; Ziereis, H.; Stratmann, G.; Brenninkmeijer, C. A. M.; Zahn, A. Impact of Acetone (Photo)Oxidation on HOx Production in the UT/LMS Based on CARIBIC Passenger Aircraft Observations and EMAC Simulations. *Geophys. Res. Lett.* **2014**, *41*, 3289–3297. https://doi.org/10.1002/2014GL061184.

(18) Arnold, S. R.; Chipperfield, M. P.; Blitz, M. A.; Heard, D. E.; Pilling, M. J. Photodissociation of Acetone: Atmospheric Implications of Temperature-Dependent Quantum Yields. *Geophys. Res. Lett.* **2004**, *31*, L07110. https://doi.org/10.1029/2003GL019099.

(19) Larson, C. W.; O'neall, H. E. Gas Phase Photolysis of Acetone. *J. Phys. Chem.* 1966, 8 (70), 2475–2486.

(20) Fischer, E. V.; Jacob, D. J.; Yantosca, R. M.; Sulprizio, M. P.; Millet, D. B.; Mao, J.; Paulot,

F.; Singh, H. B.; Roiger, A.; Ries, L.; Talbot, R. W.; Dzepina, K.; Pandey Deolal, S. Atmospheric Peroxyacetyl Nitrate (PAN): A Global Budget and Source Attribution. *Atmos. Chem. Phys.* **2014**, *14* (5), 2679–2698. https://doi.org/10.5194/acp-14-2679-2014.

(21) Moxim, W. J. Simulated Global Tropospheric PAN: Its Transport and Impact on NOx. *J. Geophys. Res. Atmos.* **1996**, *101* (D7), 12621–12638. https://doi.org/10.1029/96JD00338.

(22) Blitz, M. A.; Heard, D. E.; Pilling, M. J.; Arnold, S. R.; Chipperfield, M. P. Pressure and Temperature-Dependent Quantum Yields for the Photodissociation of Acetone between 279 and 327.5 nm. *Geophys. Res. Lett.* **2004**, *31* (6), 1–5. https://doi.org/10.1029/2003gl018793.

(23) Jacob, L. S. D.; Lee, K. L. K.; Schmidt, T. W.; Nauta, K.; Kable, S. H. The Dynamics of CO Production from the Photolysis of Acetone across the Whole $S_1 \leftarrow S_0$ absorption Spectrum: Roaming and Triple Fragmentation Pathways. *J. Chem. Phys.* **2022**, *156* (9), 094303. https://doi.org/10.1063/5.0080904.

(24) Aloisio, S.; Francisco, J. S. The Photochemistry of Acetone in the Presence of Water. *Chem. Phys. Lett.* **2000**, *329* (3–4), 179–184. https://doi.org/10.1016/S0009-2614(00)01001-0.

(25) Barker, J. R. New Light on Acetone: A Master Equation Model for Gas Phase Photophysics and Photochemistry. *Mol. Phys.* **2021**. https://doi.org/10.1080/00268976.2021.1958018.

(26) Somnitz, H.; Ufer, T.; Zellner, R. Acetone Photolysis at 248 nm Revisited: Pressure Dependence of the CO and CO_2 Quantum Yields. *Phys. Chem. Chem. Phys.* **2009**, *11* (38), 8522–8531. https://doi.org/10.1039/b906751e.

(27) Somnitz, H.; Fida, M.; Ufer, T.; Zellner, R. Pressure Dependence for the CO Quantum Yield in the Photolysis of Acetone at 248 nm: A Combined Experimental and Theoretical Study. *Phys. Chem. Chem. Phys.* **2005**, *7* (18), 3342–3352. https://doi.org/10.1039/b506738c.

(28) Horowitz, A. Wavelength Dependence of the Primary Photodissociation Processes in

Acetone Photolysis. *J. Phys. Chem.* **1991**, *95*, 10816–10823.

(29) Gandini, A.; Hackett, P. A. Electronic Relaxation Processes In-Trifluoroacetone Vapor and the Gas Phase Recombination of the Acetyl Radical at 22 °C.

(30) Saheb, V.; Zokaie, M. Multichannel Gas-Phase Unimolecular Decomposition of Acetone: Theoretical Kinetic Studies. *J. Phys. Chem. A* **2018**, *122* (28), 5895–5904. https://doi.org/10.1021/acs.jpca.8b02423.

(31) Macdonald, M. J.; Roscoe, J. M. The Photolysis of Acetone at 308 nm. *J. Photochem. Photobiol. A: Chem.* **1991**, 57. 441-451.

(32) Khamaganov, V. G.; Crowley, J. N. Pressure Dependent Photolysis Quantum Yields for $CH_3C(O)CH_3$ at 300 and 308 nm and at 298 and 228 K. *Phys. Chem. Chem. Phys.* **2013**, *15* (25), 10500–10509. https://doi.org/10.1039/c3cp50291k.

(33) Khamaganov, V. G.; Karunanandan, R.; Horowitz, A.; Dillon, T. J.; Crowley, J. N. Photolysis of $CH_3C(O)CH_3$ at 248 and 266 nm: Pressure and Temperature Dependent Overall Quantum Yields. *Phys. Chem. Chem. Phys.* **2009**, *11* (29), 6173–6181. https://doi.org/10.1039/b904130c.

(34) Lee, K. L. K.; Nauta, K.; Kable, S. H. Photodissociation of Acetone from 266 to 312 nm: Dynamics of CH_3 + CH_3CO Channels on the S_0 and T_1 States. *J. Chem. Phys.* **2017**, *146* (4), 044304. https://doi.org/10.1063/1.4974035.

(35) Rajakumar, B.; Gierczak, T.; Flad, J. E.; Ravishankara, A. R.; Burkholder, J. B. The CH_3CO Quantum Yield in the 248 nm Photolysis of Acetone, Methyl Ethyl Ketone, and Biacetyl. *J. Photochem. Photobiol. A Chem.* **2008**, *199*, 336–344. https://doi.org/10.1016/j.jphotochem.2008.06.015.

(36) Gierczak, T.; Burkholder, J. B.; Bauerle, S.; Ravishankara, A. R. Photochemistry of

Acetone under Tropospheric Conditions. *Chem. Phys.* **1998**, *231* (6), 229–244. https://doi.org/10.1016/S0301-0104(98)00006-8.

(37) Meyrahn, H.; Pauly, J.; Schneider, W.; Warneck, P. Quantum Yields for the Photodissociation of Acetone in Air and an Estimate for the Life Time of Acetone in the Lower Troposphere. *J. Atmos. Chem.* **1986**, 4, 277–291.

(38) Nádasdi, R.; Kovács, G.; Szilágyi, I.; Demeter, A.; Dóbé, S.; Bérces, T.; Márta, F. Exciplex Laser Photolysis Study of Acetone with Relevance to Tropospheric Chemistry. *Chem. Phys. Lett.* **2007**, *440* (1–3), 31–35. https://doi.org/10.1016/j.cplett.2007.04.014.

(39) Zuckermann, H.; Schmitz, B.; Haas, Y. Dissociation Energy of an Isolated Triplet Acetone Molecule. *J. Phys. Chem.* **1988**, 92, 4835–4837.

(40) Emrich, M.; Warneck, P. Erratum: Photodissociation of Acetone in Air: Dependence on Pressure and Wavelength, Behavior of the Excited Singlet State. *J. Phys. Chem. A* **2000**, *104* (42), 9436–9442. https://doi.org/10.1021/jp0407627.

(41) Zborowska, A. G.; MacInnis, C. Y.; Ye, C. Z.; Osthoff, H. D. On the Photolysis Branching Ratio of Methyl Ethyl Ketone. *Atmos. Environ.* **2021**, *254*, 118383. https://doi.org/10.1016/j.atmosenv.2021.118383.

(42) Allen, G.; Remedios, J. J.; Newnham, D. A.; Smith, K. M.; Monks, P. S. Improved Mid-Infrared Cross-Sections for Peroxyacetyl Nitrate (PAN) Vapour. *Atmos. Chem. Phys.* **2005**, *5* (1), 47–56. https://doi.org/10.5194/acp-5-47-2005.

(43) Blitz, M. A.; Heard, D. E.; Pilling, M. J. Study of Acetone Photodissociation over the Wavelength Range 248-330 Nm: Evidence of a Mechanism Involving Both the Singlet and Triplet Excited States. *J. Phys. Chem. A* **2006**, *110* (21), 6742–6756. https://doi.org/10.1021/jp056276g.

(44) Groß, C. B. M.; Dillon, T. J.; Crowley, J. N. Pressure Dependent OH Yields in the Reactions of CH_3CO and $HOCH_2CO$ with O_2. *Phys. Chem. Chem. Phys.* **2014**, *16* (22), 10990–10998. https://doi.org/10.1039/c4cp01108b.

(45) Maranzana, A.; Barker, J. R.; Tonachini, G. Master Equation Simulations of Competing Unimolecular and Bimolecular Reactions: Application to OH Production in the Reaction of Acetyl Radical with O_2. *Phys. Chem. Chem. Phys.* **2007**, *9* (31), 4129–4141. https://doi.org/10.1039/b705116f.

(46) Blitz, M. A.; Heard, D. E.; Pilling, M. J. OH Formation from $CH_3CO + O_2$: A Convenient Experimental Marker for the Acetyl Radical. *Chem. Phys. Lett.* **2002**, *365* (5–6), 374–379. https://doi.org/10.1016/S0009-2614(02)01484-7.

(47) Huey, L. G.; Hanson, D. R.; Howard, C. J. Reactions of SF_6^- and I^- with Atmospheric Trace Gases. *J. Phys. Chem.* **1995**, *99* (14), 5001–5008. https://doi.org/10.1021/j100014a021.

(48) Lee, B. H.; Lopez-Hilfiker, F. D.; Veres, P. R.; McDuffie, E. E.; Fibiger, D. L.; Sparks, T. L.; Ebben, C. J.; Green, J. R.; Schroder, J. C.; Campuzano-Jost, P.; Iyer, S.; D'Ambro, E. L.; Schobesberger, S.; Brown, S. S.; Wooldridge, P. J.; Cohen, R. C.; Fiddler, M. N.; Bililign, S.; Jimenez, J. L.; Kurtén, T.; Weinheimer, A. J.; Jaegle, L.; Thornton, J. A. Flight Deployment of a High-Resolution Time-of-Flight Chemical Ionization Mass Spectrometer: Observations of Reactive Halogen and Nitrogen Oxide Species. *J. Geophys. Res. Atmos.* **2018**, *123* (14), 7670–7686. https://doi.org/10.1029/2017JD028082.

(49) Bertram, T. H.; Kimmel, J. R.; Crisp, T. A.; Ryder, O. S.; Yatavelli, R. L. N.; Thornton, J. A.; Cubison, M. J.; Gonin, M.; Worsnop, D. R. A Field-Deployable, Chemical Ionization Time-of-Flight Mass Spectrometer. *Atmos. Meas. Tech.* **2011**, *4* (7), 1471–1479. https://doi.org/10.5194/amt-4-1471-2011.

(50) Pu, W.; Zou, Z.; Wang, W.; Tanner, D.; Wang, Z.; Wang, T. Development of a Chemical Ionization Mass Spectrometry System for Measurement of Atmospheric OH Radical. *Atmos. Meas. Tech.* **2020**, https://doi.org/10.5194/amt-2020-252.

(51) Muller, J. B. A.; Elste, T.; Plass-dülmer, C.; Stange, G.; Holla, R.; Claude, A.; Englert, J.; Gilge, S.; Kubistin, D.; Hohenpeissenberg, M. O.; Dwd, D. W. A Novel Semi-Direct Method to Measure OH Reactivity by Chemical Ionization Mass Spectrometry (CIMS). *Atmos. Meas. Tech.* **2018**, 11, 4413–4433.

(52) Albrecht, S. R.; Novelli, A.; Hofzumahaus, A.; Kang, S.; Baker, Y.; Mentel, T.; Wahner, A.; Fuchs, H. Measurements of Hydroperoxy Radicals (HO_2) at Atmospheric Concentrations Using Bromide Chemical Ionisation Mass Spectrometry. *Atmos. Meas. Tech.* **2019**, *12* (2), 891–902. https://doi.org/10.5194/amt-12-891-2019.

(53) Sanchez, J.; Tanner, D. J.; Chen, D.; Huey, L. G.; Ng, N. L. A New Technique for the Direct Detection of HO_2 Radicals Using Bromide Chemical Ionization Mass Spectrometry (Br-CIMS): Initial Characterization. *Atmos. Meas. Tech.* **2016**, *9* (8), 3851–3861. https://doi.org/10.5194/amt-9-3851-2016.

(54) Zaytsev, A.; Breitenlechner, M.; Novelli, A.; Fuchs, H.; Knopf, D.; Kroll, J.; Keutsch, F. Application of Chemical Derivatization Techniques Combined with Chemical Ionization Mass Spectrometry to Detect Stabilized Criegee Intermediates and Peroxy Radicals in the Gas Phase. *Atmos. Meas. Tech. Discuss.* **2020**, 335, 1–20. https://doi.org/10.5194/amt-2020-335.

(55) Iyer, S.; He, X.; Hyttinen, N.; Kurtén, T.; Rissanen, M. P. Computational and Experimental Investigation of the Detection of HO_2 Radical and the Products of Its Reaction with Cyclohexene Ozonolysis Derived RO_2 Radicals by an Iodide-Based Chemical Ionization

Mass Spectrometer. *J. Phys. Chem. A* **2017**, *121* (36), 6778–6789. https://doi.org/10.1021/acs.jpca.7b01588.

(56) Leather, K. E.; Bacak, A.; Wamsley, R.; Archibald, A. T.; Husk, A.; Shallcross, D. E.; Percival, C. J. Temperature and Pressure Dependence of the Rate Coefficient for the Reaction between ClO and CH_3O_2 in the Gas-Phase. *Phys. Chem. Chem. Phys.* **2012**, *14* (10), 3425–3434. https://doi.org/10.1039/c2cp22834c.

(57) Link, M. F.; Farmer, D. K.; Berg, T.; Flocke, F.; Ravishankara, A. R. Measuring Photodissociation Product Quantum Yields Using Chemical Ionization Mass Spectrometry: A Case Study with Ketones. *J. Phys. Chem. A* **2021**, *125*, 6836–6844. https://doi.org/10.1021/acs.jpca.1c03140.

(58) North, S. W.; Blank, D. A.; Daniel Gezelter, J.; Longfellow, C. A.; Lee, Y. T. Evidence for Stepwise Dissociation Dynamics in Acetone at 248 and 193 nm. *J. Chem. Phys.* **1995**, *102* (11), 4447–4460. https://doi.org/10.1063/1.469493.

(59) Toulson, B. W.; Fishman, D. A.; Murray, C. Photodissociation Dynamics of Acetone Studied by Time-Resolved Ion Imaging and Photofragment Excitation Spectroscopy. *Phys. Chem. Chem. Phys.* **2018**, *20* (4), 2454–2469. https://doi.org/10.1039/c7cp07320h.

(60) Hu, L.; Millet, D. B.; Kim, S. Y.; Wells, K. C.; Griffis, T. J.; Fischer, E. V.; Helmig, D.; Hueber, J.; Curtis, A. J. North American Acetone Sources Determined from Tall Tower Measurements and Inverse Modeling. *Atmos. Chem. Phys.* **2013**, *13* (6), 3379–3392. https://doi.org/10.5194/acp-13-3379-2013.

(61) Wang, S.; Apel, E. C.; Schwantes, R. H.; Bates, K. H.; Jacob, D. J.; Fischer, E. V.; Hornbrook, R. S.; Hills, A. J.; Emmons, L. K.; Pan, L. L.; Honomichl, S.; Tilmes, S.; Lamarque, J. F.; Yang, M.; Marandino, C. A.; Saltzman, E. S.; de Bruyn, W.; Kameyama,

S.; Tanimoto, H.; Omori, Y.; Hall, S. R.; Ullmann, K.; Ryerson, T. B.; Thompson, C. R.; Peischl, J.; Daube, B. C.; Commane, R.; McKain, K.; Sweeney, C.; Thames, A. B.; Miller, D. O.; Brune, W. H.; Diskin, G. S.; DiGangi, J. P.; Wofsy, S. C. Global Atmospheric Budget of Acetone: Air-Sea Exchange and the Contribution to Hydroxyl Radicals. *J. Geophys. Res. Atmos.* **2020**, *125* (15), 1–23. https://doi.org/10.1029/2020JD032553.

(62) Brewer, J. F.; Papanastasiou, D. K.; Burkholder, J. B.; Fischer, E. V.; Ren, Y.; Mellouki, A.; Ravishankara, A. R. Atmospheric Photolysis of Methyl Ethyl, Diethyl, and Propyl Ethyl Ketones: Temperature-Dependent UV Absorption Cross Sections. *J. Geophys. Res. Atmos.* **2019**, *124* (11), 5906–5918. https://doi.org/10.1029/2019JD030391.

(63) Jaeglé, L.; Jacob, D. J.; Brune, W. H.; Wennberg, P. O. Chemistry of HO(x) Radicals in the Upper Troposphere. *Atmos. Environ.* **2001**, *35* (3), 469–489. https://doi.org/10.1016/S1352-2310(00)00376-9.

(64) Sander, S. P.; Friedl, R. R.; Golden, D. M.; Kurylo, M. J.; Moortgat, G. K.; Wine, P. H.; Ravishankara, a R.; Kolb, C. E.; Molina, M. J.; Diego, S.; Jolla, L.; Huie, R. E.; Orkin, V. L. Chemical Kinetics and Photochemical Data for Use in Atmospheric Studies Evaluation Number 19; 2020.

(65) Chattopadhyay, A.; Chatterjee, P.; Chakraborty, T. Photo-Oxidation of Acetone to Formic Acid in Synthetic Air and Its Atmospheric Implication. *J. Phys. Chem. A* **2015**, *119* (29), 8146–8155. https://doi.org/10.1021/acs.jpca.5b04905.

(66) Rissanen, M. P.; Mikkilä, J.; Iyer, S.; Hakala, J. Multi-Scheme Chemical Ionization Inlet (MION) for Fast Switching of Reagent Ion Chemistry in Atmospheric Pressure Chemical Ionization Mass Spectrometry (CIMS) Applications. *Atmos. Meas. Tech.* **2019**, *12* (12), 6635–6646. https://doi.org/10.5194/amt-12-6635-2019.

(67) Hansel, A.; Scholz, W.; Mentler, B.; Fischer, L.; Berndt, T. Detection of RO_2 Radicals and Other Products from Cyclohexene Ozonolysis with NH_4^+ and Acetate Chemical Ionization Mass Spectrometry. *Atmos. Environ.* **2018**, *186*, 248–255. https://doi.org/10.1016/j.atmosenv.2018.04.023.

(68) Slusher, D. L.; Huey, L. G.; Tanner, D. J.; Flocke, F. M.; Roberts, J. M. A Thermal Dissociation - Chemical Ionization Mass Spectrometry (TD-CIMS) Technique for the Simultaneous Measurement of Peroxyacyl Nitrates and Dinitrogen Pentoxide. *J. Geophys. Res. D Atmos.* **2004**, *109* (19), 1–13. https://doi.org/10.1029/2004JD004670.

(69) Veres, P.; Roberts, J. M.; Warneke, C.; Welsh-Bon, D.; Zahniser, M.; Herndon, S.; Fall, R.; de Gouw, J. Development of Negative-Ion Proton-Transfer Chemical-Ionization Mass Spectrometry (NI-PT-CIMS) for the Measurement of Gas-Phase Organic Acids in the Atmosphere. *Int. J. Mass Spectrom.* **2008**, *274* (1–3), 48–55. https://doi.org/10.1016/j.ijms.2008.04.032.

(70) Fulgham, S. R.; Brophy, P.; Link, M.; Ortega, J.; Pollack, I.; Farmer, D. K. Seasonal Flux Measurements over a Colorado Pine Forest Demonstrate a Persistent Source of Organic Acids. *ACS Earth Sp. Chem.* **2019**, *3* (9), 2017–2032. https://doi.org/10.1021/acsearthspacechem.9b00182.

(71) Rajakumar, B.; Flad, J. E.; Gierczak, T.; Ravishankara, A. R.; Burkholder, J. B. Visible Absorption Spectrum of the CH_3CO Radical. *J. Phys. Chem. A* **2007**, *111* (37), 8950–8958. https://doi.org/10.1021/jp073339h.

(72) Brophy, P.; Farmer, D. K. A Switchable Reagent Ion High Resolution Time-of-Flight Chemical Ionization Mass Spectrometer for Real-Time Measurement of Gas Phase Oxidized Species: Characterization from the 2013 Southern Oxidant and Aerosol Study.

Atmos. Meas. Tech. **2015**, *8* (7), 2945–2959. https://doi.org/10.5194/amt-8-2945-2015.

(73) Lopez-Hilfiker, F. D.; Iyer, S.; Mohr, C.; Lee, B. H.; D'ambro, E. L.; Kurtén, T.; Thornton, J. A. Constraining the Sensitivity of Iodide Adduct Chemical Ionization Mass Spectrometry to Multifunctional Organic Molecules Using the Collision Limit and Thermodynamic Stability of Iodide Ion Adducts. *Atmos. Meas. Tech.* **2016**, *9* (4), 1505–1512. https://doi.org/10.5194/amt-9-1505-2016.

(74) Flocke, F. M.; Weinheimer, A. J.; Swanson, A. L.; Roberts, J. M.; Schmitt, R.; Shertz, S. On the Measurement of PANs by Gas Chromatography and Electron Capture Detection. *J. Atmos. Chem.* **2005**, *52* (1), 19–43. https://doi.org/10.1007/s10874-005-6772-0.

(75) Gandini, A.; Hackett, P. A. Electronic Relaxation Processes In-Trifluoroacetone Vapor and the Gas Phase Recombination of the Acetyl Radical at 22 °C. *J. Am. Chem. Soc.* **1977**, *99* (19), 6195–6205.

(76) Khamaganov, V.; Karunanandan, A.; Rodriguez, A.; Crowley, J. N. Photolysis of CH3C(O)CH3 (248 Nm, 266 Nm), CH3C(O)C2H5 (248 Nm) and CH3C(O)Br (248 Nm): Pressure Dependent Quantum Yields of CH3 Formation. *Phys. Chem. Chem. Phys.* **2007**, *9* (31), 4098–4113. https://doi.org/10.1039/b701382e.

(77) Greenblatt, G. D.; Ruhman, S.; Haas, Y. Flourescence Decay Kinetics of Acetone Vapour at Low Pressures, **1984**, 112.

(78) Papadimitriou, V. C.; Karafas, E. S.; Gierczak, T.; Burkholder, J. B. $CH_3CO + O_2 + M$ (M = He, N_2) Reaction Rate Coefficient Measurements and Implications for the OH Radical Product Yield. *J. Phys. Chem. A* **2015**, *119* (28), 7481–7497. https://doi.org/10.1021/acs.jpca.5b00762.

(79) Tyndall, G. S.; Orlando, J. J.; Wallington, T. J.; Hurley, M. D. Pressure Dependence of the

Rate Coefficients and Product Yields for the Reaction of CH_3CO Radicals with O_2. *Int. J. Chem. Kinet.* **1997**, *29* (9), 655–663. https://doi.org/10.1002/(SICI)1097-4601(1997)29:9<655::AID-KIN2>3.0.CO;2-T.

(80) Saxena, S.; Kiefer, J. H.; Klippenstein, S. J. A Shock-Tube and Theory Study of the Dissociation of Acetone and Subsequent Recombination of Methyl Radicals. *Proc. Combust. Inst.* **2009**, *32* (1), 123–130.

(81) Berg, T. C.; Farmer, D. K.; Link, M. F.; Lee, S.; Ravishankara, A. R. The Quantum Yields for Thermalized $CH_3C(O)$ from Acetone Photodissociation as a Function of Wavelength and Pressure. *in prep.*

(82) Link, M. F.; Blitz, M. A.; Wan, Y.; Brewer, J. F.; Farmer, D. K.; Ravishankara, A. R. Constraining the Acetone Photolysis Quantum Yield: Current Insights and Atmospheric Chemistry Implications. *in review.*

(83) Kovács, G.; Zádor, J.; Farkas, E.; Nádasdi, R.; Szilágyi, I.; Dóbé, S.; Bérces, T.; Márta, F.; Lendvay, G. Kinetics and Mechanism of the Reactions of CH_3CO and $CH_3C(O)CH_2$ Radicals with O_2. Low-Pressure Discharge Flow Experiments and Quantum Chemical Computations. *Phys. Chem. Chem. Phys.* **2007**, *9* (31), 4142–4154. https://doi.org/10.1039/b706216h.

(84) Cantrell, C. A.; Shetter, R. E.; Calvert, J. G. Comparison of Perxoy Radical Concentrations at Several Contrasting Sites. *J. Atmos. Sci.* **1995**, *52* (19), 3408–3412.

(85) Tan, Z.; Hofzumahaus, A.; Lu, K.; Brown, S. S.; Holland, F.; Huey, L. G.; Kiendler-Scharr, A.; Li, X.; Liu, X.; Ma, N.; Min, K. E.; Rohrer, F.; Shao, M.; Wahner, A.; Wang, Y.; Wiedensohler, A.; Wu, Y.; Wu, Z.; Zeng, L.; Zhang, Y.; Fuchs, H. No Evidence for a Significant Impact of Heterogeneous Chemistry on Radical Concentrations in the North

China Plain in Summer 2014. *Environ. Sci. Technol.* **2020**, *54* (10), 5973–5979. https://doi.org/10.1021/acs.est.0c00525.

(86) Tyndall, G. S.; Cox, R. A.; Granier, C.; Lesclaux, R.; Moortgat, G. K.; Pilling, M. J.; Ravishankara, A. R.; Wallington, T. J. Atmospheric Chemistry of Small Organic Peroxy Radicals. *J. Geophys. Res. Atmos.* **2001**, *106* (D11), 12157–12182. https://doi.org/10.1029/2000JD900746.

(87) Chen, S. Y.; Lee, Y. P. Transient Infrared Absorption of t-$CH_3C(O)OO$, c-$CH_3C(O)OO$, and α-Lactone Recorded in Gaseous Reactions of CH_3CO and O_2. *J. Chem. Phys.* **2010**, *132* (11). https://doi.org/10.1063/1.3352315.

(88) George, M.; Dolores Andrés Hernández, M.; Nenakhov, V.; Liu, Y.; Philip Burrows, J. Airborne Measurement of Peroxy Radicals Using Chemical Amplification Coupled with Cavity Ring-down Spectroscopy: The PeRCEAS Instrument. *Atmos. Meas. Tech.* **2020**, *13* (5), 2577–2600. https://doi.org/10.5194/amt-13-2577-2020.

(89) Fuchs, H.; Holland, F.; Hofzumahaus, A. Measurement of Tropospheric RO_2 and HO_2 Radicals by a Laser-Induced Fluorescence Instrument. *Rev. Sci. Instrum.* **2008**, *79* (8), 084104. https://doi.org/10.1063/1.2968712.

(90) Kundu, S.; Deming, B. L.; Lew, M. M.; Bottorff, B. P.; Rickly, P.; Stevens, P. S.; Dusanter, S.; Sklaveniti, S.; Leonardis, T.; Locoge, N.; Wood, E. C. Peroxy Radical Measurements by Ethane-Nitric Oxide Chemical Amplification and Laser-Induced Fluorescence during the IRRONIC Field Campaign in a Forest in Indiana. *Atmos. Chem. Phys.* **2019**, *19* (14), 9563–9579. https://doi.org/10.5194/acp-19-9563-2019.

(91) Tan, Z.; Fuchs, H.; Lu, K.; Hofzumahaus, A.; Bohn, B.; Broch, S.; Dong, H.; Gomm, S.; Häseler, R.; He, L.; Holland, F.; Li, X.; Liu, Y.; Lu, S.; Rohrer, F.; Shao, M.; Wang, B.;

Wang, M.; Wu, Y.; Zeng, L.; Zhang, Y.; Wahner, A.; Zhang, Y. Radical Chemistry at a Rural Site (Wangdu) in the North China Plain: Observation and Model Calculations of OH, HO_2 and RO_2 Radicals. *Atmos. Chem. Phys.* **2017**, *17* (1), 663–690. https://doi.org/10.5194/acp-17-663-2017.

(92) Zaytsev, A.; Breitenlechner, M.; Novelli, A.; Fuchs, H.; A. Knopf, D.; H. Kroll, J.; N. Keutsch, F. Application of Chemical Derivatization Techniques Combined with Chemical Ionization Mass Spectrometry to Detect Stabilized Criegee Intermediates and Peroxy Radicals in the Gas Phase. *Atmos. Meas. Tech.* **2021**, *14* (3), 2501–2513. https://doi.org/10.5194/amt-14-2501-2021.

(93) Hornbrook, R. S.; Crawford, J. H.; Edwards, G. D.; Goyea, O.; Mauldin, R. L.; Olson, J. S.; Cantrell, C. A. Measurements of Tropospheric HO_2 and RO_2 by Oxygen Dilution Modulation and Chemical Ionization Mass Spectrometry. *Atmos. Meas. Tech.* **2011**, *4* (4), 735–756. https://doi.org/10.5194/amt-4-735-2011.

(94) Edwards, G. D.; Cantrell, C. A.; Stephens, S.; Hill, B.; Goyea, O.; Shetter, R. E.; Mauldin, R. L.; Kosciuch, E.; Tanner, D. J.; Eisele, F. L. Chemical Ionization Mass Spectrometer Instrument for the Measurement of Tropospheric HO_2 and RO_2. *Anal. Chem.* **2003**, *75* (20), 5317–5327. https://doi.org/10.1021/ac034402b.

(95) Zhang, W.; Zhang, H. Secondary Ion Chemistry Mediated by Ozone and Acidic Organic Molecules in Iodide-Adduct Chemical Ionization Mass Spectrometry. *Anal. Chem.* **2021**, No. 93, 8595–8602. https://doi.org/10.1021/acs.analchem.1c01486.

(96) Robinson, M. A.; Andrew Neuman, J.; Huey, L. G.; Roberts, J. M.; Brown, S. S.; Veres, P. R. Temperature-Dependent Sensitivity of Iodide Chemical Ionization Mass Spectrometers. *Atmos. Meas. Tech.* **2022**, *15* (14), 4295–4305. https://doi.org/10.5194/amt-15-4295-2022.

(97) Brophy, P.; Farmer, D. K. Clustering, Methodology, and Mechanistic Insights into Acetate Chemical Ionization Using High-Resolution Time-of-Flight Mass Spectrometry. *Atmos. Meas. Tech.* **2016**, *9* (8), 3969–3986. https://doi.org/10.5194/amt-9-3969-2016.

(98) Li, J.; Link, M. F.; Pandit, S.; Webb, M. H.; Mayer, K. J.; Garofalo, L. A.; Rediger, K. L.; Poppendieck, D. G.; Zimmerman, S. M.; Vance, M. E.; Grassian, V. H.; Morrison, G. C.; Turpin, B. J.; Farmer, D. K. The Persistence of Smoke VOCs Indoors: Partitioning, Surface Cleaning, and Air Cleaning in a Smoke-Contaminated House. *Sci. Adv.* **2023**, 9, eadh8263.

(99) Wang, M.; He, X.-C.; Finkenzeller, H.; Iyer, S.; Chen, D.; Shen, J.; Simon, M.; Hofbauer, V.; Kirkby, J.; Curtius, J.; Maier, N.; Kurtén, T.; Worsnop, D.; Kulmala, M.; Rissanen, M.; Volkamer, R.; Tham, Y. J.; Donahue, N.; Sipilä, M. Measurement of Iodine Species and Sulfuric Acid Using Bromide Chemical Ionization Mass Spectrometers. *Atmos. Meas. Tech. Discuss.* **2020**, 1–23. https://doi.org/10.5194/amt-2020-494.

(100) Xu, L.; Coggon, M. M.; Stockwell, C. E.; Gilman, J. B.; Robinson, M. A.; Breitenlechner, M.; Lamplugh, A.; Crounse, J. D.; Wennberg, P. O.; Neuman, J. A.; Novak, G. A.; Veres, P. R.; Brown, S. S.; Warneke, C. Chemical Ionization Mass Spectrometry Utilizing Ammonium Ions (NH_4^+ CIMS) for Measurements of Organic Compounds in the Atmosphere. *Atmos. Meas. Tech.* **2022**, *15* (24), 7353–7373. https://doi.org/10.5194/amt-15-7353-2022.

(101) Mattila, J. M.; Lakey, P. S. J.; Shiraiwa, M.; Wang, C.; Abbatt, J. P. D.; Arata, C.; Goldstein, A. H.; Ampollini, L.; Katz, E. F.; Decarlo, P. F.; Zhou, S.; Kahan, T. F.; Cardoso-Saldaña, F. J.; Ruiz, L. H.; Abeleira, A.; Boedicker, E. K.; Vance, M. E.; Farmer, D. K. Multiphase Chemistry Controls Inorganic Chlorinated and Nitrogenated Compounds in Indoor Air during Bleach Cleaning. *Environ. Sci. Technol.* **2020**, *54* (3), 1730–1739.

https://doi.org/10.1021/acs.est.9b05767.

(102) Christophorou, L. G.; Olthoff, J. K. Electron Interactions With Cl_2. *J. Phys. Chem. Ref. Data* **1999**, *28* (1), 131–169. https://doi.org/10.1063/1.556036.

(103) Han, J. C.; Suto, M.; Lee, J. C.; Petrović, Z. L. Transient Signals Induced by Laser Irradiation of Negative Ions in Hollow Electrode Discharges of Cl_2 and HCl in N_2. *J. Appl. Phys.* **1990**, *68* (6), 2649–2656. https://doi.org/10.1063/1.346490.

(104) Babcock, L. M.; Streit, G. E. Ion–Molecule Reactions of Cl_2 with Cl^- and F^-. **1982**, *76* (5), 2407–2411.

(105) Finley, B. D.; Saltzman, E. S. Observations of Cl_2, Br_2, and I_2 in Coastal Marine Air. *J. Geophys. Res. Atmos.* **2008**, *113*, D21301. https://doi.org/10.1029/2008JD010269.

(106) Chupka, W. A.; Berkowitz, J.; Gutman, D. Electron Affinities of Halogen Diatomic Molecules as Determined by Endoergic Charge Transfer. *J. Chem. Phys.* **1971**, *55* (6), 2724–2733. https://doi.org/10.1063/1.1676487.

(107) Travers, M. J.; Cowles, D. C.; Ellison, G. B. Reinvestigation of the Electron Affinities of 95 O2 and NO. Chem. Phys. Lett. 1989, 164 (5), 450–455.

(108) Amelynck, C.; Arijs, E.; Schoon, N.; Van Bavel, A.-M. Gas Phase Reactions of HNO_3 with Cl^-, Cl^-H_2O, and Cl^-HCl, of Cl_2 with Cl^-H_2O and Cl^-HCl, and of HCl with Cl^-H_2O. *Int. J. Mass Spectrom.* **1998**, *181*, 113–121. https://doi.org/10.1116/1.579503.

(109) Klotz, B.; Graedler, F.; Sørensen, S.; Barnes, I.; Becker, K. H. A Kinetic Study of the Atmospheric Photolysis of α-Dicarbonyls. *Int. J. Chem. Kinet.* **2001**, *33* (1), 9–20. https://doi.org/10.1002/1097-4601(20010101)33:1<9::AID-KIN2>3.0.CO;2-V.

(110) Horowitz, A.; Meller, R.; Moortgat, G. K. The UV-VIS Absorption Cross Sections of the α-Dicarbonyl Compounds: Pyruvic Acid, Biacetyl and Glyoxal. *J. Photochem. Photobiol.*

A Chem. **2001**, *146* (1–2), 19–27. https://doi.org/10.1016/S1010-6030(01)00601-3.

(111) Bouzidi, H.; Fittschen, C.; Coddeville, P.; Tomas, A. Photolysis of 2,3-Pentanedione and 2,3-Hexanedione: Kinetics, Quantum Yields, and Product Study in a Simulation Chamber. *Atmos. Environ.* **2014**, *82*, 250–257. https://doi.org/10.1016/j.atmosenv.2013.10.039.

APPENDIX A

SUPPORTING INFORMATION FOR CH. 1: THE QUANTUM YIELDS FOR THERMALIZED $CH_3C(O)$ FROM ACETONE PHOTODISSOCIATION AS A FUNCTION OF WAVELENGTH AND PRESSURE

Contents

A.1 0-D Model Calculations to Examine Secondary Loss of $CH_3C(O)$ and $CH_3C(O)O_2$

We used the Framework for 0-D Atmospheric Modeling (F0AM) for 0-D calculation of $CH_3C(O)O_2$ loss to radical-radical reactions as a function of radical concentration formed during photolysis. The reactor parameters used for model calculations are provided as part of Figure A.i, with a complete reaction time of 0.20 seconds. The full reaction mechanism used in the model is tabulated in Appendix B. We performed model calculations for several conditions, including temperatures from 223 to 303 K, pressures from 150 to 850 mbar, and $CH_3O_2/CH_3C(O)O_2$ ratios between 1 and 2.25. The model calculated for $CH_3C(O)O_2$ changes were compared to our experiments to characterize $CH_3C(O)O_2$ and $CH_3C(O)$ quantum yield as a function of $CH_3C(O)O_2$ production.

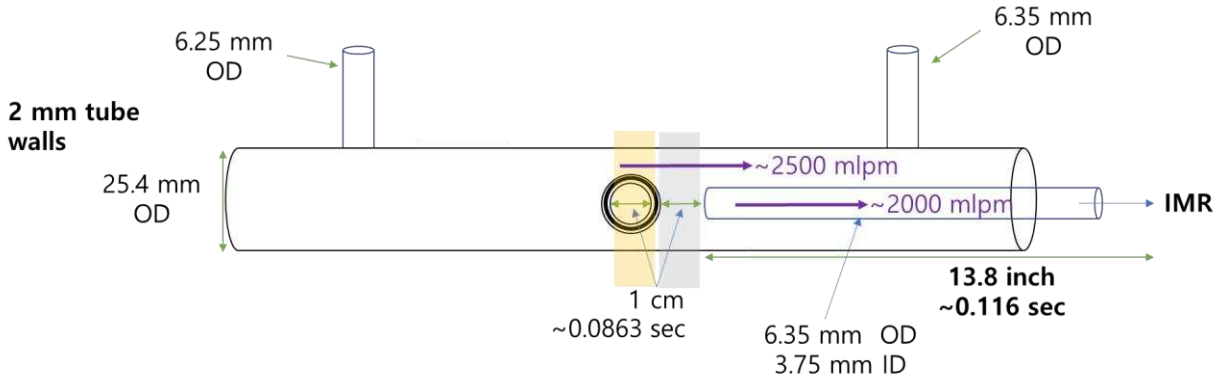

Figure A.i A schematic of the photolysis reactor, including dimensions, flow rates, and reaction times used for 0-D modeling of radical concentrations. We used the Framework for 0-D atmospheric modeling for all calculations of $CH_3C(O)O_2$ loss in the reactor. Model reactions are provided in Appendix-C.

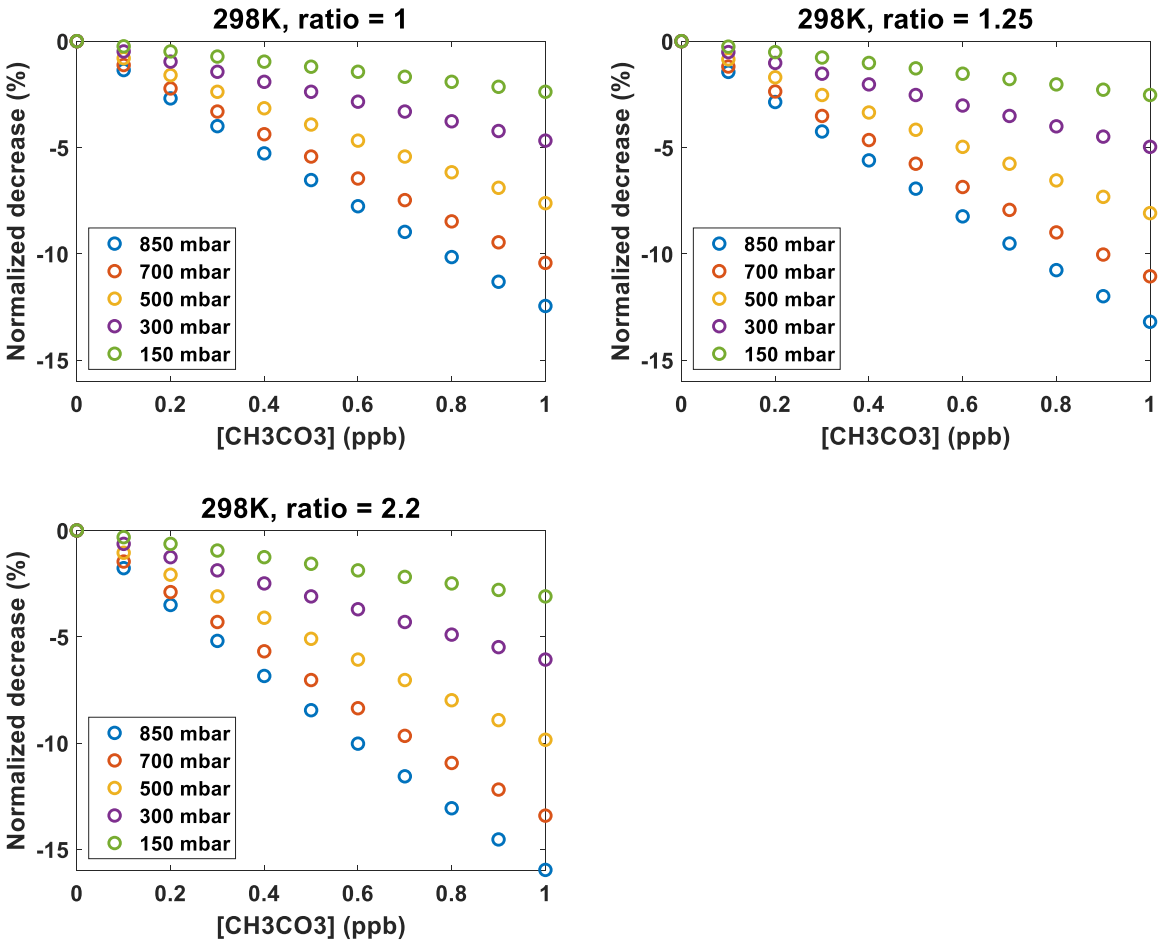

Figure A.ii F0AM results for the expected loss of $CH_3C(O)O_2$ before CIMS sampling, as a function initial of $CH_3C(O)O_2$ concentration. The ratio indicates the modeled value for CH_3O_2/$CH_3C(O)O_2$ formed following photolysis. Ratios between 1 and 1.25 show possible values based on Blitz parameterization of photolysis following 280 to 330 nm photolysis. 2.2 is the highest possible ratio of CH_3O_2 and $CH_3C(O)O_2$ at 254 nm (150 mbar). As stated in Ch. 2 and shown in Figure A.viii, losses of $CH_3C(O)O_2$ were not observed for up to 400 ppt, and quantum yields are not corrected for model expected loss.

A.2 Wavelength Calibration and Relative Photolysis Flux Measurements

The Ocean Optics HR2000-CG-UV-NIR spectrometer required two data adjustments prior to use: calibration of the spectrometer for wavelength scale and intensity response function over the studied wavelength range.

We calibrated the spectrometer using the Hg lines at 254, 313, and 365 nm from a Hg Pen-Ray lamp. We used the wavelength from our calibrated spectrometer for measurements of Φ_{CH_3CO}. Interpolation between just three known wavelengths may introduce some error to this calculation, but the target wavelength range of 280 to 335 nm for quantum yield measurements is centered nearly around 313 nm and the measured offset of the KiloArc emission at 254 should be nearly equal to the offset measured for the 254 nm Hg line. Uncertainty (1σ) in the measured central wavelength at 313 nm was 2%, while the 254 and 365 nm uncertainties were ≤ 0.2%.

To identify the spectrometer's response function for intensity, we used a SL-3 Deuterium lamp calibrated by the manufacturer (StellarNet). The lamp calibration was traceable to the NIST standard. For response function calibration, the cosine corrector on the end of the spectrometer fiber optic cable was placed within the exit aperture of the SL-3. We first adjusted the measured intensities at each pixel in the spectrum using the wavelength offset calculation described above. We identified the intensity in photons cm^{-2} at the wavelength of each pixel by interpolating from the wavelengths provided in the SL-3 calibration data. The response function of the spectrometer was the measured intensity per photon cm^{-2} at each pixel. The results of the response function calibration between 200 and 450 nm, developed from the average of 50 SL-3 spectra, are shown below (Figure A.iii). 1σ uncertainty in the response function between 254 and 335 nm is ≤ 3%.

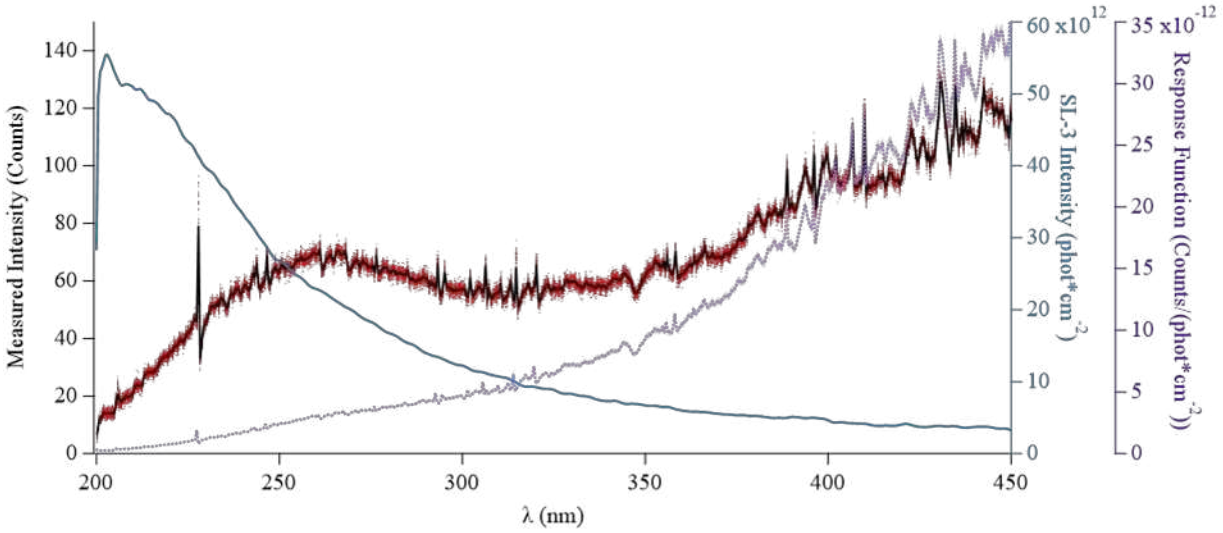

Figure A.iii HR2000-CG-UV-NIR response function data. Measured (red dots) and average (black line) intensity of SL-3 emission on the left axis, with calibrated SL-3 intensity (blue line) and resulting HR2000-CG-UV-NIR response function (purple line) on the inner and outer right axes, respectively.

Following the quantum yield measurements described in Ch. 2, we used an algorithm for rapid calculation of the quantum yields from each measurement. The algorithm used user-defined time inputs for the start of each automated quantum yield measurement to extract and process $I(CH_3C(O)O_2)^-$ data from the CIMS and coinciding spectra recorded from the HR2000-CG-UV-NIR. Using another time series provided by the OceanOptics OceanView software, the algorithm identified an approximate central wavelength for the KiloArc emission at each wavelength setting, and then extracted signals from every pixel within 7 nm on either side of that wavelength. Pixel intensities were then averaged across all the measured spectra in each step of the automated quantum yield measurement. The averaged pixel intensities were adjusted by the algorithm for pixel wavelength offset and response function. The absorption cross-section at each true pixel wavelength was found by interpolation of available cross-section data. Intensities at each pixel multiplied by the calculated absorption cross sections returned effective peak wavelength for acetone absorbance of the KiloArc emission. An example of this convolution of the intensity and

absorption cross section is shown in Figure A.iv. The algorithm was used to calculate the effective center wavelengths for these new peak shapes, to assign the wavelength for calculation of quantum yield. The ratio of the new peak integral at 254 to that at the wavelength of interest (again adjusted for the response function) provided $F_{254}\sigma_{254}/F_{\lambda}\sigma_{\lambda}$ for calculation of quantum yields.

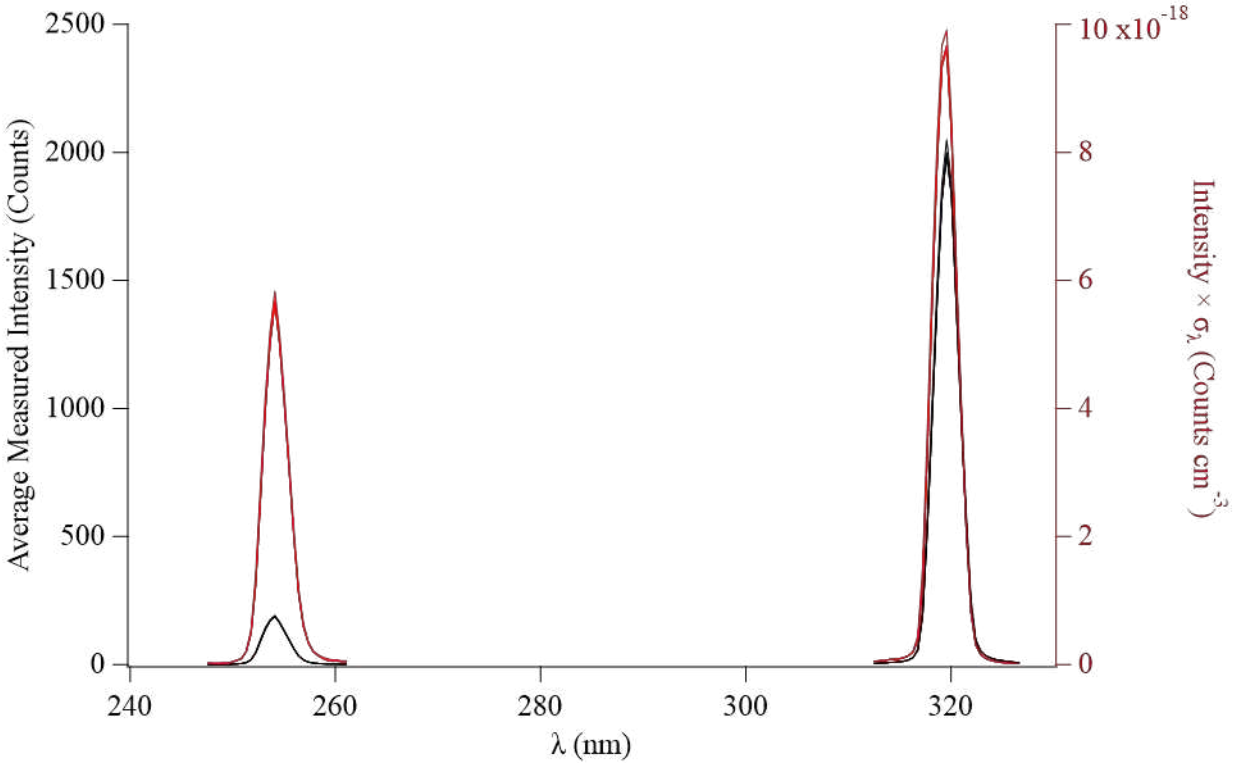

Figure A.iv Measured intensity and absorption cross section convoluted data for the KiloArc emission from five automated quantum yield tests performed at 320 nm. Black lines represent the average measured intensity. Red lines are the intensity convoluted with absorption cross section (σ). Note the slight right shift (higher wavelength) of the peak center for 254 nm after convolution, while convolution shifts the peak left (lower wavelength) at 320 nm.

A.3 Calibration of CIMS for detection of $CH_3C(O)O_2$

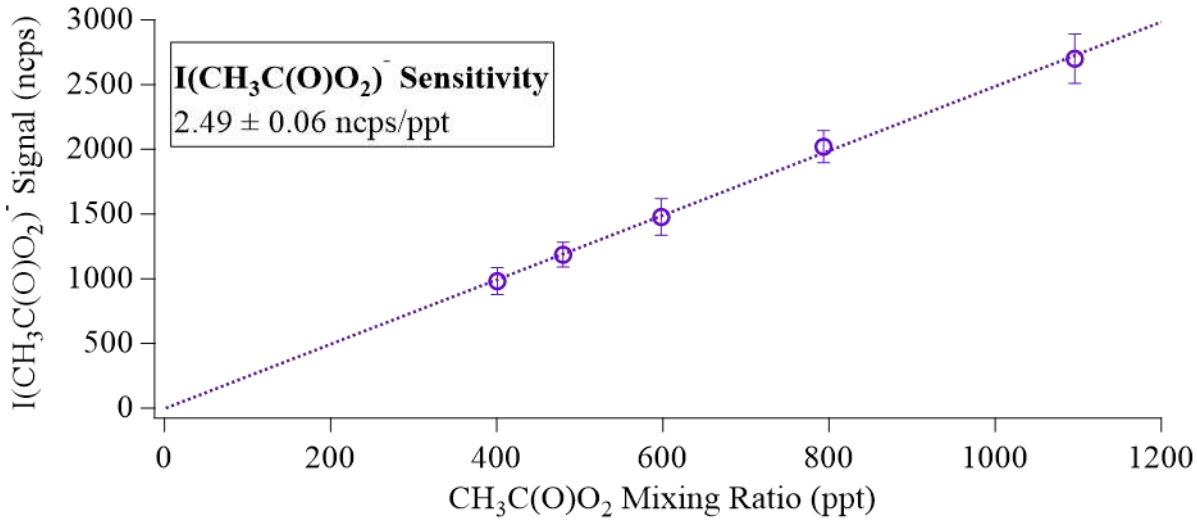

Figure A.v An example calibration of the I-CIMS response to $CH_3C(O)O_2$ mixing ratio produced by PAN thermal decomposition. Signal is normalized to I-CIMS reagent ion counts ($[I^- + IH_2O^-]/1\times10^6$). We used a peroxy acetyl nitrate (PAN) source developed by Dr. Frank Flocke to produce known concentrations of PAN. Pan was thermally dissociated to produce known concentration of $CH_3C(O)O_2$ (references included in Ch. 2). The PAN source produces 40 ppb of PAN through photolysis of acetone (2% in air; Scott Marin) in the presence of NO. We obtained NO compressed gas standards of 20 ppm in N_2 (Airgas). Prior to use, we diluted the NO standard to 2 ppm in N_2 in a 12 L glass bulb. The PAN source photolyzes excess acetone in the presence of NO to produce NO_2, which reacts with remaining $CH_3C(O)O_2$ to produce PAN. For $CH_3C(O)O_2$ calibrations, we mixed the output flow of the PAN source with ultra-zero air prior to the reactor entrance, to produce 400 to 1200 ppt PAN in the sample flow to between (400 and 1200 ppt). A heating rope wrapped around the CIMS sampling tube heated the PAN sample to 150 °C ~1" from the CIMS inletto completely thermally decompose of PAN into $CH_3C(O)O_2$.

A.4 Detection of Acetone and Photolysis Products

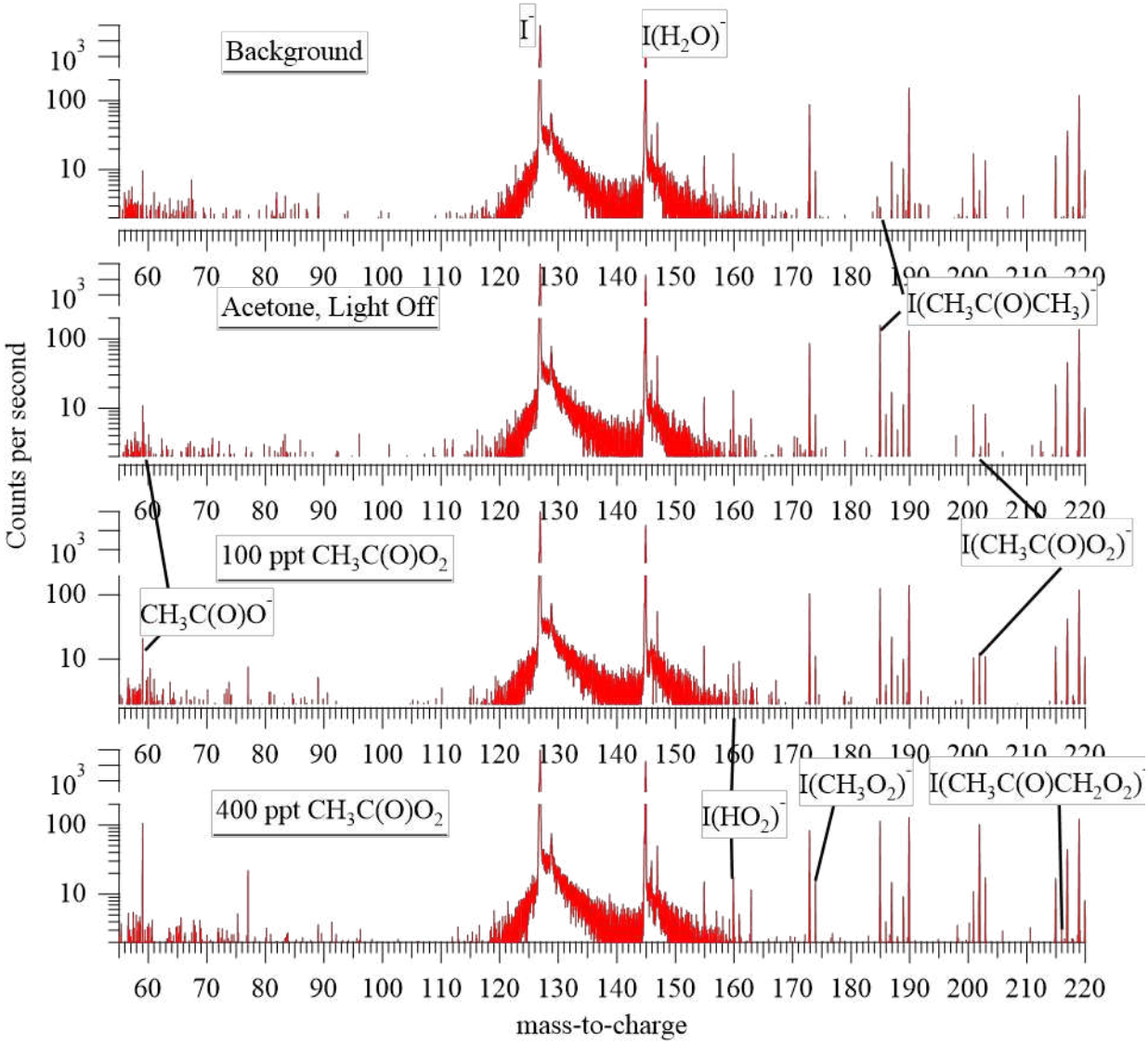

Figure A.vi Example mass spectra for various steps in acetone photolysis measurements. The condition of each spectrum is listed (underlined) in each portion of the graph. Product ions from acetone and its photolysis are listed as they begin to appear. $I(CH_3C(O)CH_3)^-$ was formed in small amounts upon addition of ~1 ppm acetone and did not perturb reagent ion concentrations. $I(CH_3C(O)O_2)^-$ and $CH_3C(O)O^-$ were the primary ions observed during acetone photolysis, but $CH_3C(O)O^-$ has higher background and more possible interferences. $I(HO_2)^-$, a possible sign of $CH_3C(O)O_2$ loss, is produced in low amounts (20-30 Hz^{-1}) at 400 ppt $CH_3C(O)O_2$. $I(CH_3O_2)^-$ and $I(CH_3C(O)CH_2O_2)^-$ are included to highlight the lack of their appearance in the high-resolution fitting. CH_3O_2 is another product of acetone photolysis which may be measured by a different reagent ion chemistry. $CH_3C(O)H_2O_2$ is a possible product of both acetone oxidation by OH and the reaction of excited state acetone with O_2, which was not observed.

A.5 Determination of the Effective Acetone Absorption Cross Sections

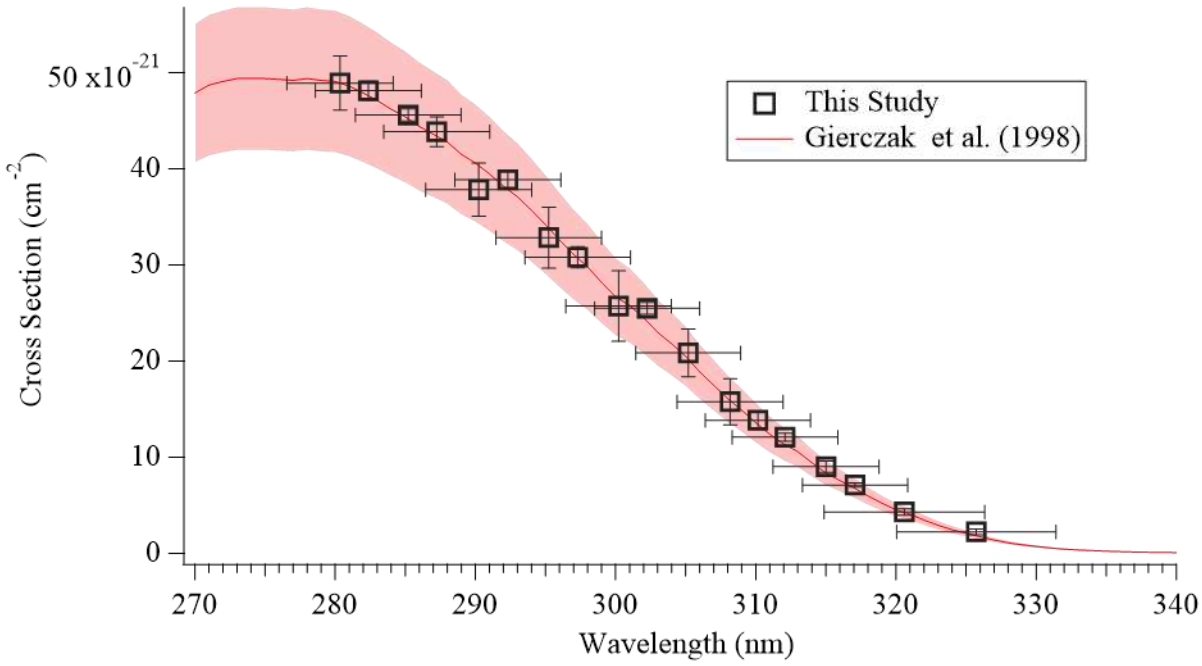

Figure A.vii Absorption cross sections for acetone measured for this study (black markers), superimposed with those measured by Gierczak et al. (red line) over a similar wavelength range. Vertical bars represent the 1σ standard deviation of the mean for triplicate measurements made at each wavelength. Horizontal bars are the full-width half-maximum resolution of the monochromator output detected by the Ocean Insight spectrometer. Shading for the red line represents uncertainty in the Gierczak et al. data.

We measured acetone absorption cross sections using the custom differential absorption setup. The system consisted of two ½" O.D. Pyrex absorption cells with ends capped by 1/8" thick fused silica windows. The absorption cells were connected by PFA tubing to two mass flow controllers, one for introduction of acetone mixtures directly from gas bulbs (>20 mL/min flowrate) and another for cleaning the cells with N_2 (>100 mL/min flowrate). The test cell (length = 10.79 cm) was positioned at the monochromator exit of the KiloArc illumination system. The reference cell (length = 10.49) we set up nearby with a Pen-Ray lamp light source, providing 254 nm reference absorbance. The OI Spectrometer measured light intensity from the KiloArc, and we used two photodiodes – a signal photodiode placed after the reference cell and a reference

photodiode placed directly behind to the Pen-Ray Lamp – to monitor absorbance in the reference cell. The reference cell design was identical to that used for acetone bulb concentration measurements. Our data agrees well with the larger dataset of Gierczak et al.

A.6 Measured $CH_3C(O)O_2$ Variation with Acetone Concentration and Photolysis Light Flux

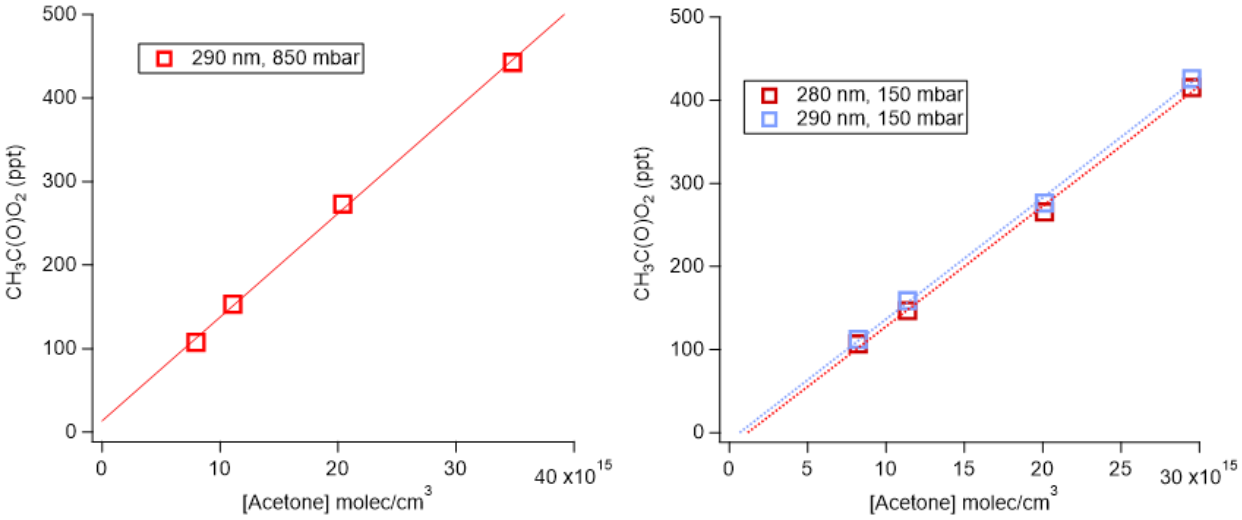

Figure A.viii Demonstration of linear response of $CH_3C(O)O_2$ concentration to reduction in acetone concentration for $CH_3C(O)O_2$ < 500 ppt. To achieve the lower $CH_3C(O)O_2$ concentrations, acetone concentration was reduced from 3.5×10^{16} cm^3 to 8×10^{15} cm^3, with light intensity was maintained at $1/8^{th}$ of maximum. These tests show that impacts of $CH_3C(O)O_2$ loss prior to CIMS sampling should be negligible for all quantum yield measurements below 320 nm, where $CH_3C(O)O_2$ were maintained at or below 400 ppt.

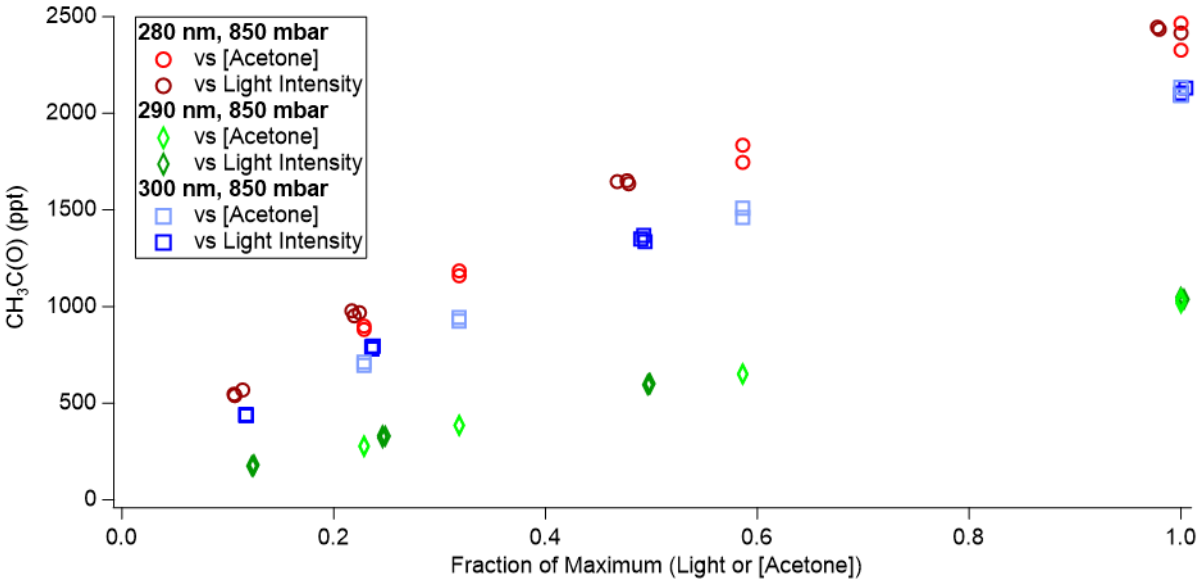

Figure A.ix Demonstration of non-linear response of $CH_3C(O)O_2$ concentration with reductions in acetone concentration and light. Acetone concentration was reduced from 3.5×10^{16} cm^3 to 8×10^{15} cm^3, while light intensity was reduced to $1/8^{th}$ of maximum through combination of 0.3 OD and 0.6 OD neutral density filters. Similar trends in $CH_3C(O)O_2$ concentration with acetone concentration and light intensity suggest that the non-linear change is due to reactive loss of $CH_3C(O)O_2$ at high concentrations. The observation of $CH_3C(O)O_2$ loss between photolysis and detection agrees with reactor models, which indicate > 25% $CH_3C(O)O_2$ loss for the highest concentrations of $CH_3C(O)O_2$ (~2500 ppt).

A.7 Stern-Volmer Analyses of Measured Quantum Yields in Air

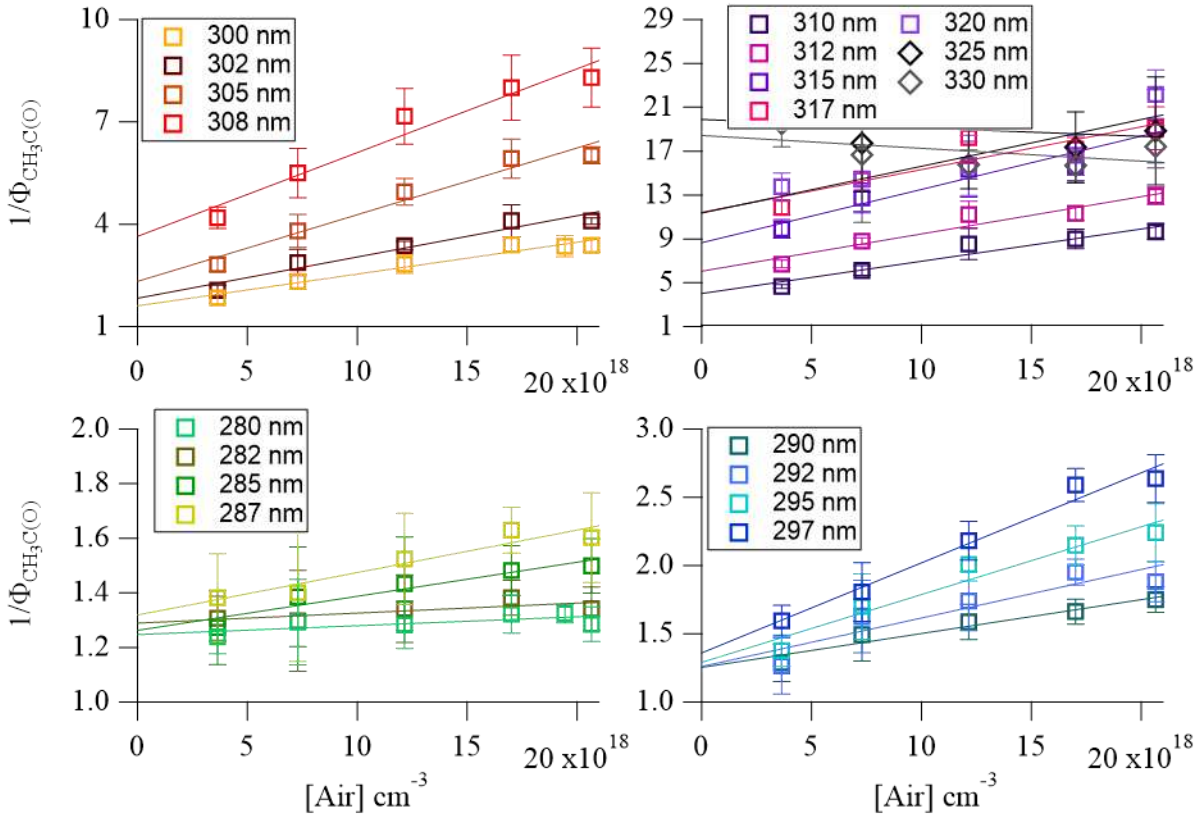

Figure A.x $1/\Phi_{CH_3CO}$ full dataset for Stern-Volmer analysis for the variation of Φ_{CH_3CO} with [Air]. Lines represent linear regressions of $1/\Phi_{CH_3CO}$ vs. air molecule number density. Error bars represent 1σ standard deviation.

APPENDIX B

The room temperature Φ_{CH_3CO} dataset temperature-dependent Φ_{CH_3CO} dataset and full reaction and rate list for the F0AM kinetic model data are publicly available at: osf.io/8uvwd

APPENDIX C

SUPPLEMENTAL INFORMATION FOR CH. 2: PARAMETERIZATION OF $CH_3C(O)$ QUANTUM YIELDS IN ACETONE PHOTOLYSIS THROUGHOUT THE TROPOSPHERE AS A FUNCTION OF TEMPERATURE, PRESSURE, AND WAVELENGTH

Contents

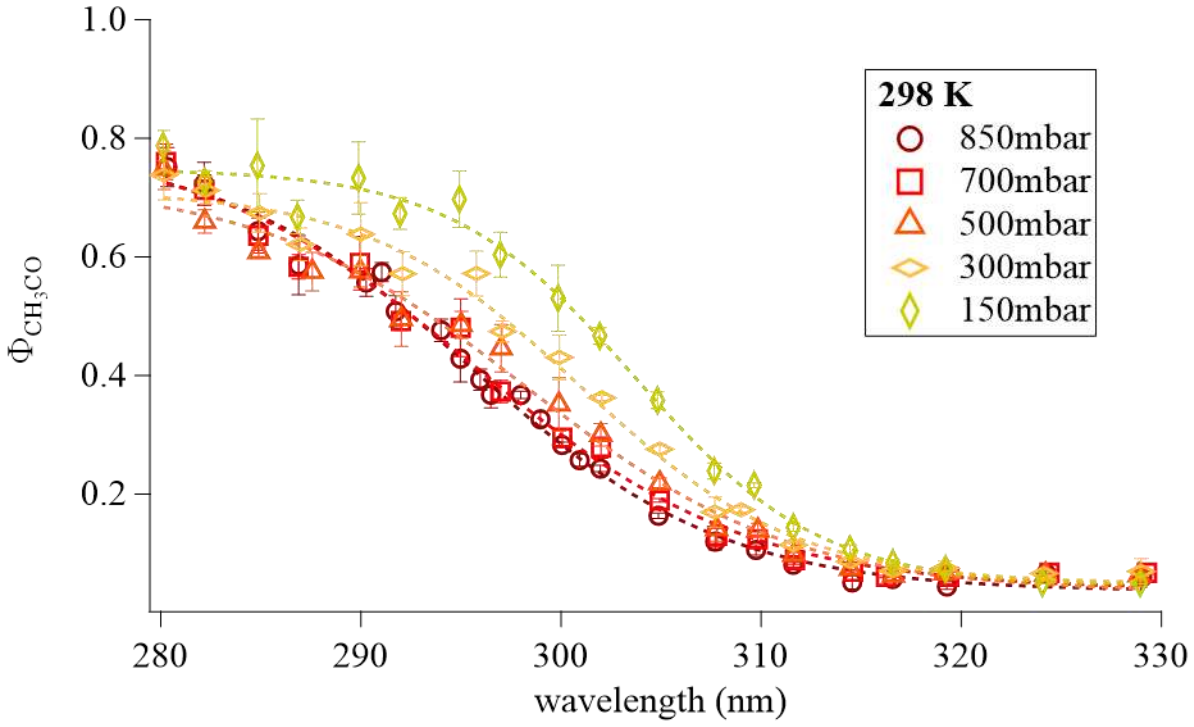
298 K
850mbar
700mbar
500mbar
300mbar
150mbar
Φ_{CH_3CO}
1.0
0.8
0.6
0.4
0.2
280
290
300
310
320
330
wavelength (nm)

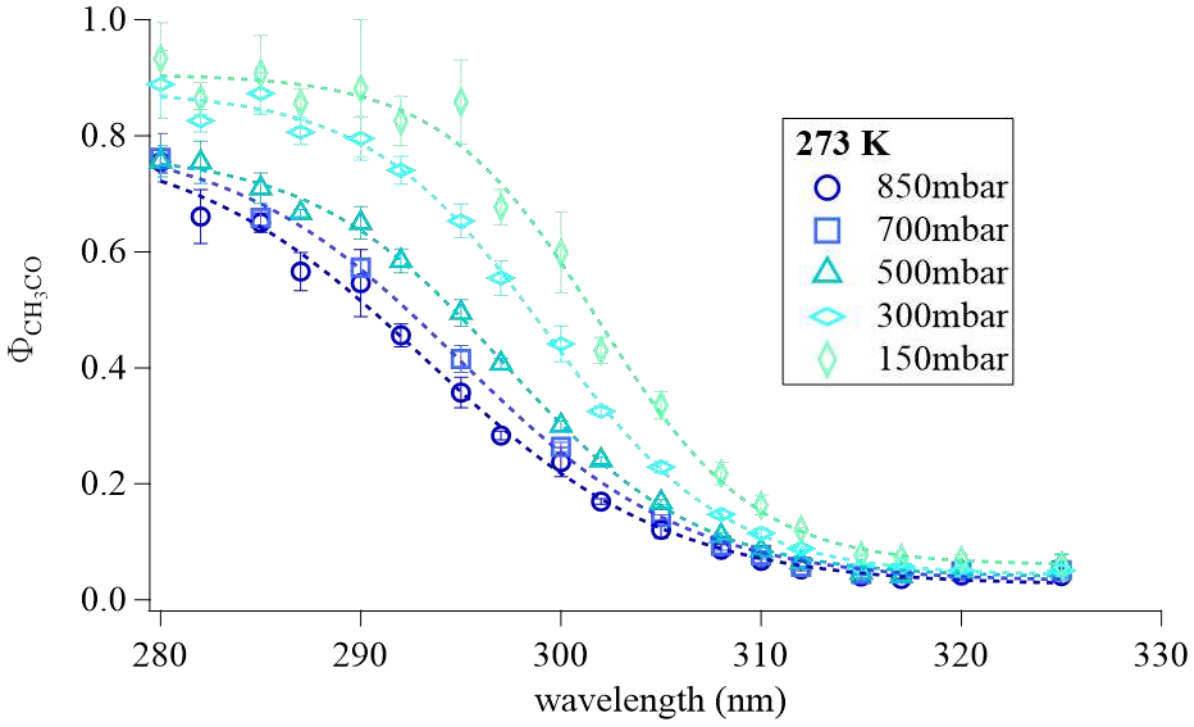
273 K
850mbar
700mbar
500mbar
300mbar
150mbar
Φ_{CH_3CO}
1.0
0.8
0.6
0.4
0.2
0.0
280
290
300
310
320
330
wavelength (nm)

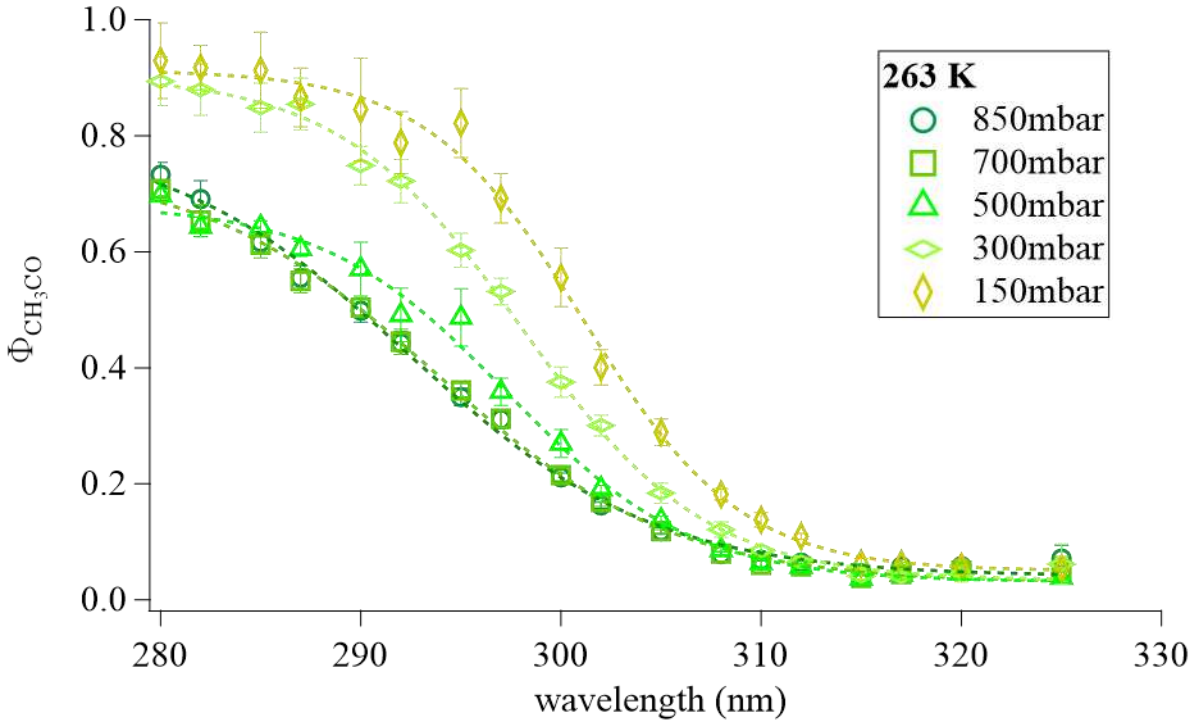
263 K
850mbar
700mbar
500mbar
300mbar
150mbar
Φ_{CH_3CO}
wavelength (nm)

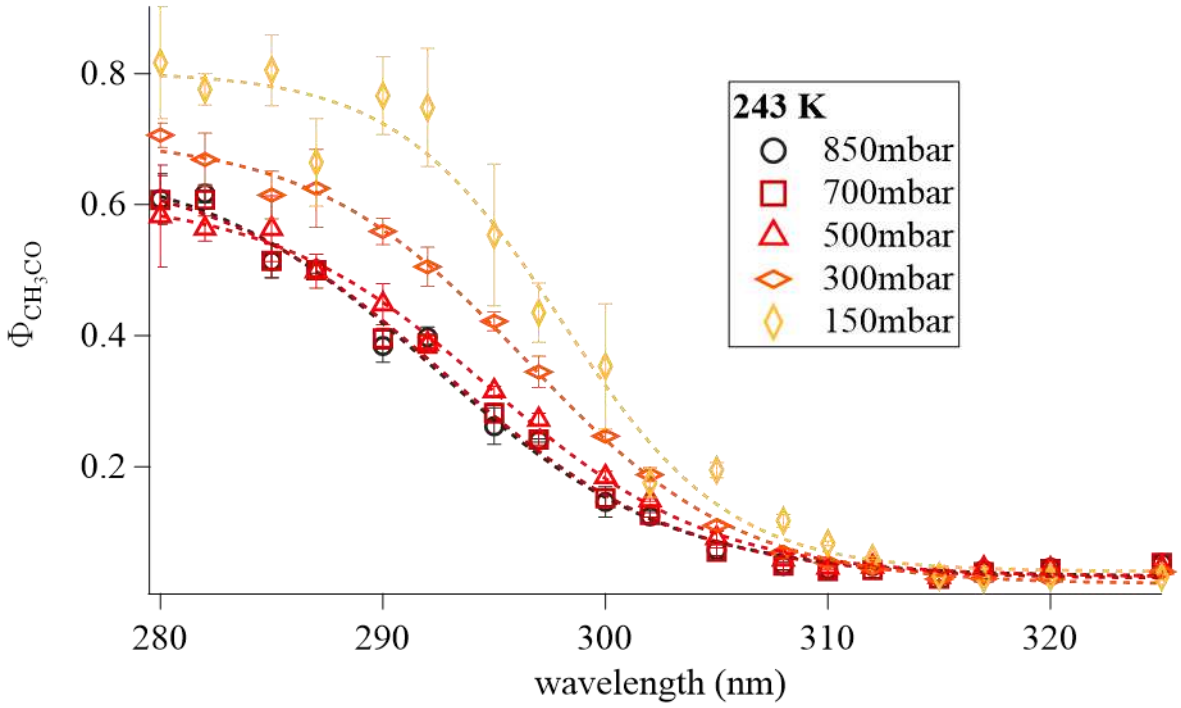
243 K
850mbar
700mbar
500mbar
300mbar
150mbar
Φ_{CH_3CO}
wavelength (nm)

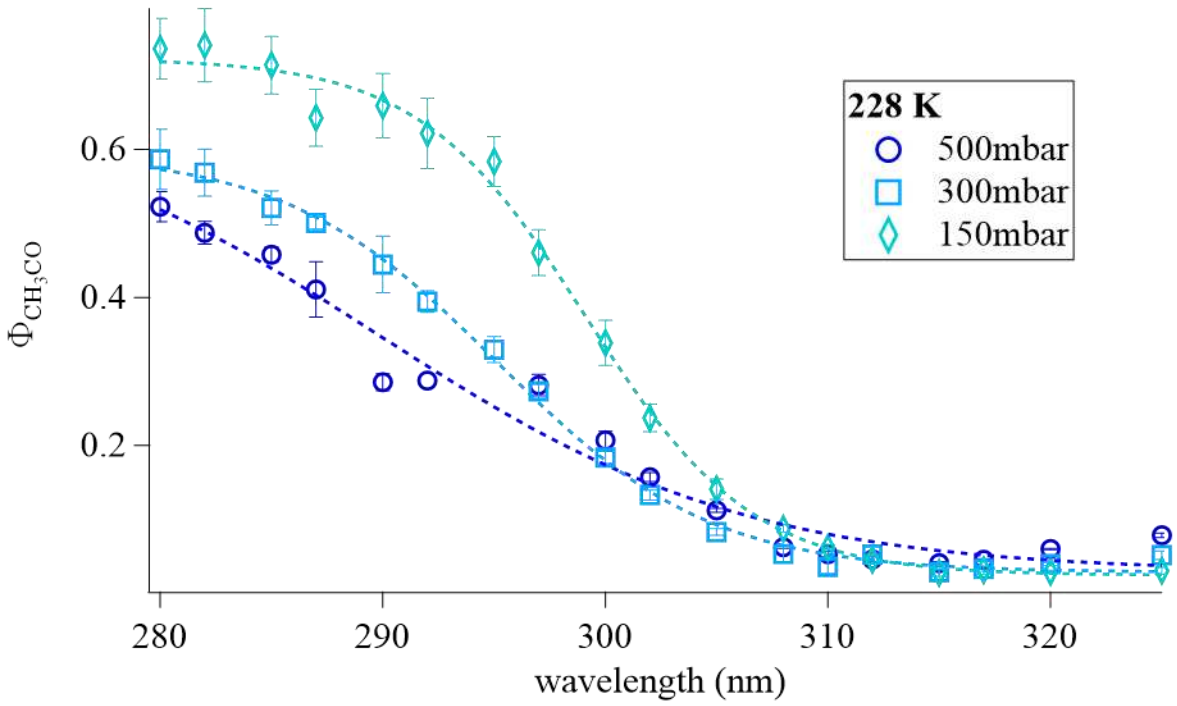

Figure C.i Quantum yields for all tested conditions between 298 K and 228 K as a function of wavelength. Sigmoid fits for each temperature and pressure setting are included as dashed lines. Parameters derived from these sigmoidal fits were used to develop the quantum yield parameterization in Ch 3.

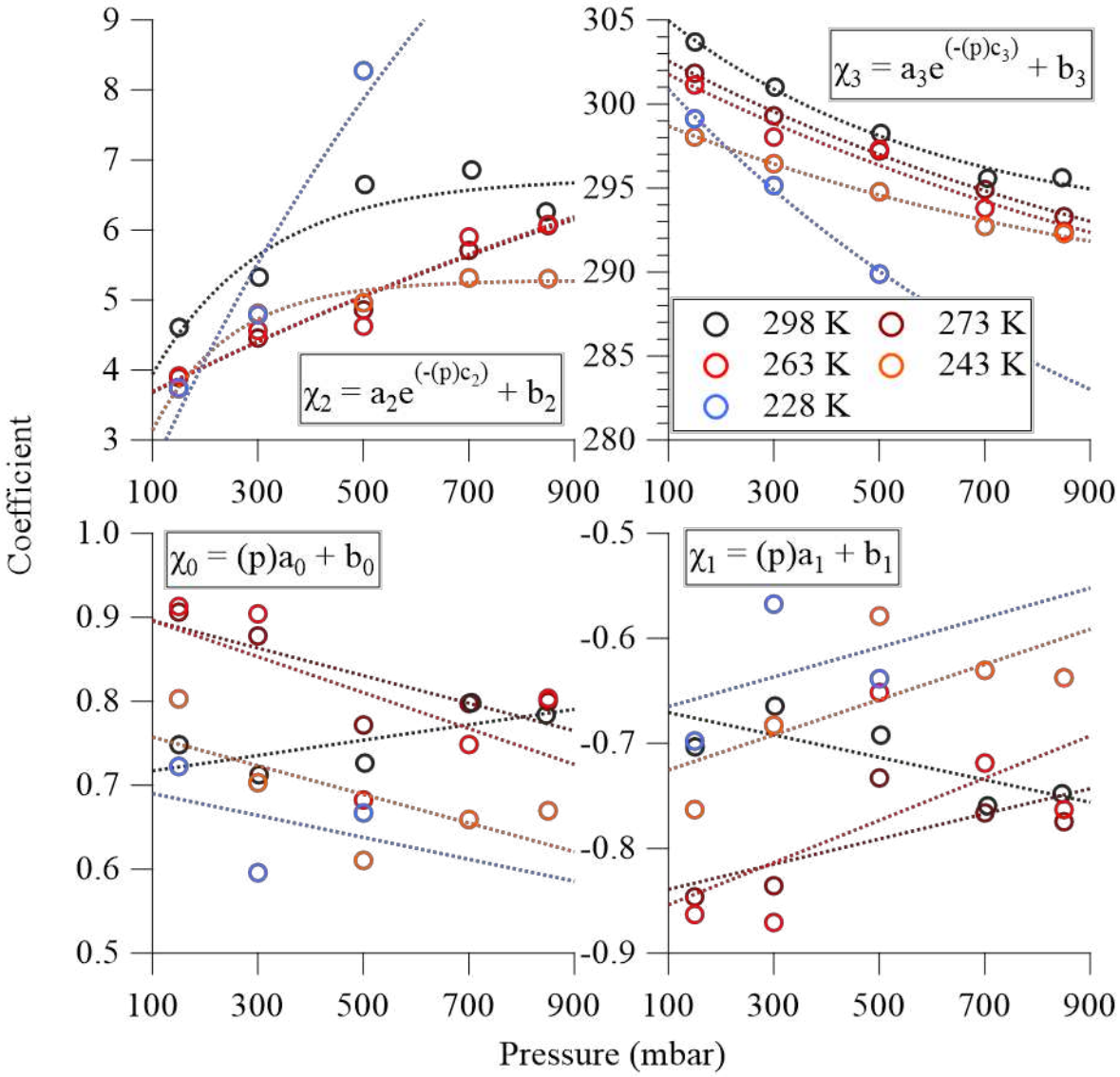

Figure C.ii Fits of sigmoid fit coefficients ($\chi_{0\text{-}3}$) as a function of pressure at temperatures from 228 to 298 K. Equations used for fits of each coefficient are displayed on the corresponding section of the figure. Coefficients from these fits (a, b, and c) were fit against temperature to develop the final equations of the parameterization in Ch. 3.

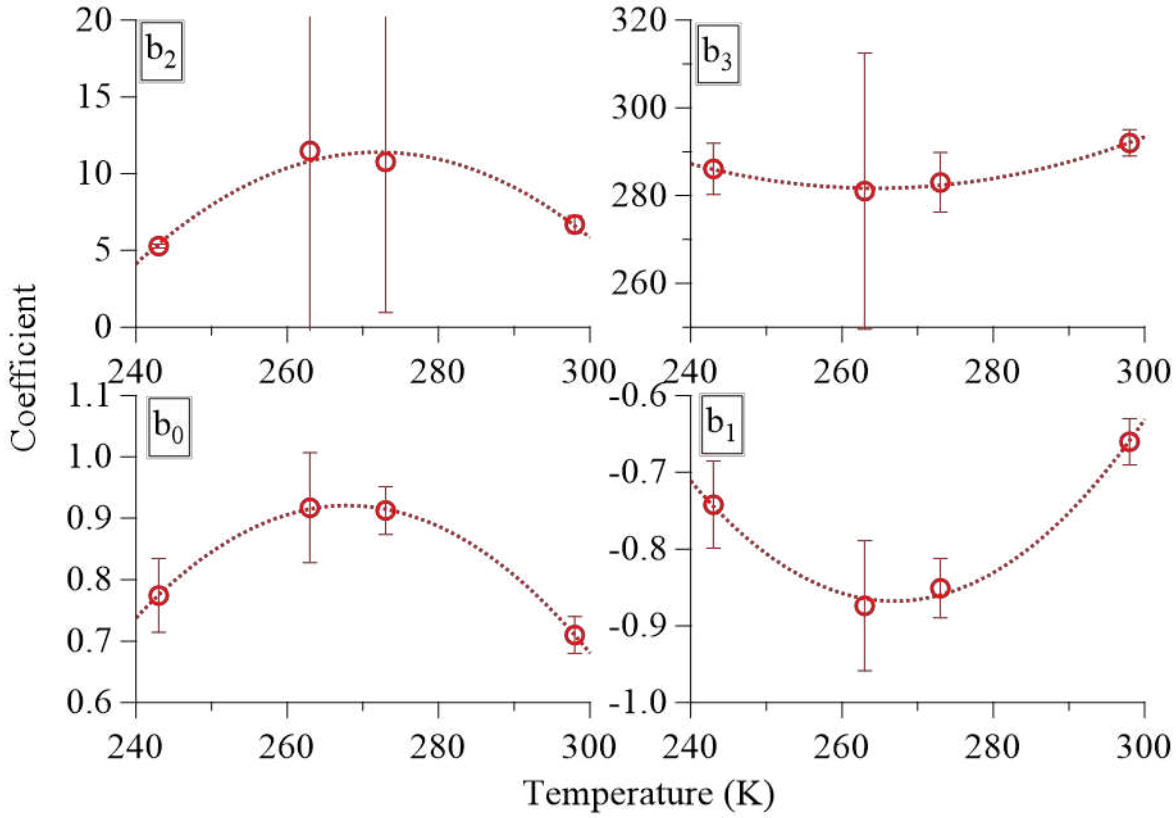

Figure C.iii Polynomial fits of all four b (intercept terms) as a function of temperature. All terms fit for change with temperature were fit to polynomial functions of the form $y = A_0 + A_1x + A_2x^2$. Equations and coefficients for these fits are given in Ch. 3.

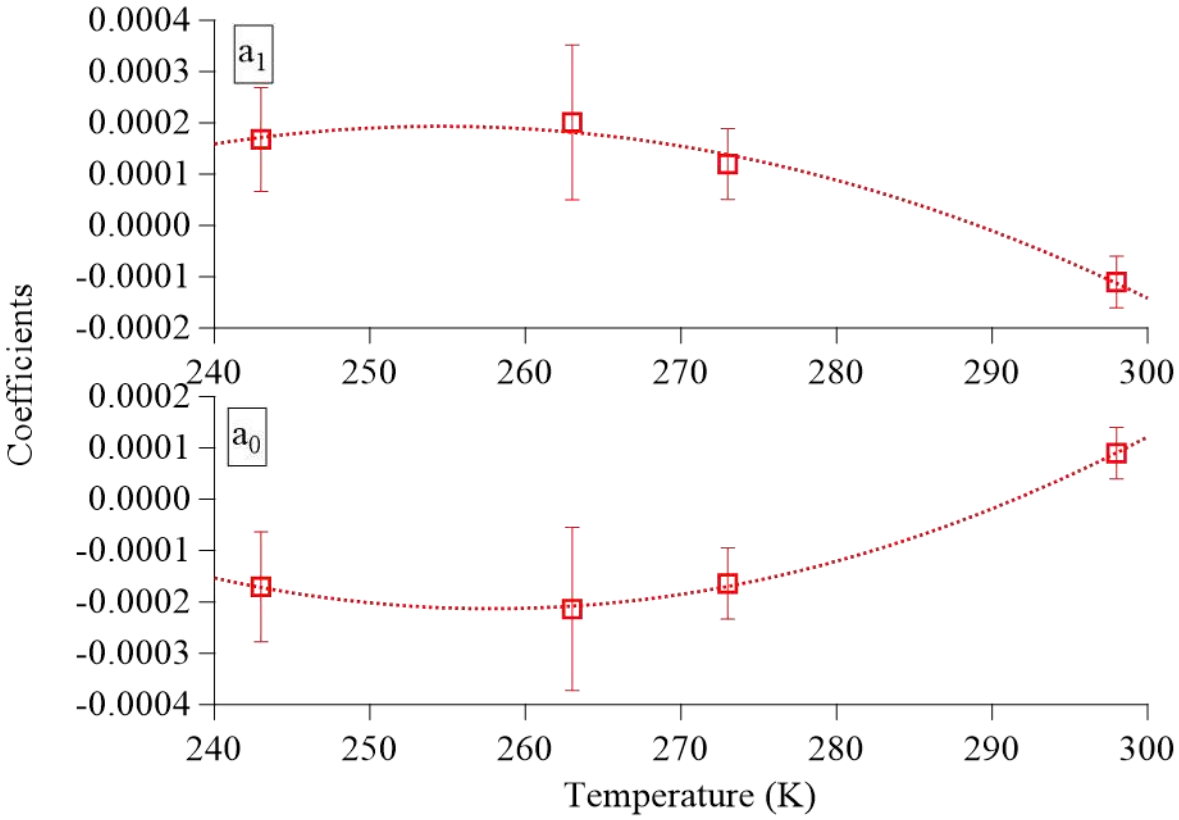

Figure C.iv Polynomial fits of $a_{0\text{-}1}$ terms for $\chi_{0\text{-}1}$ (slope terms) as a function of temperature.

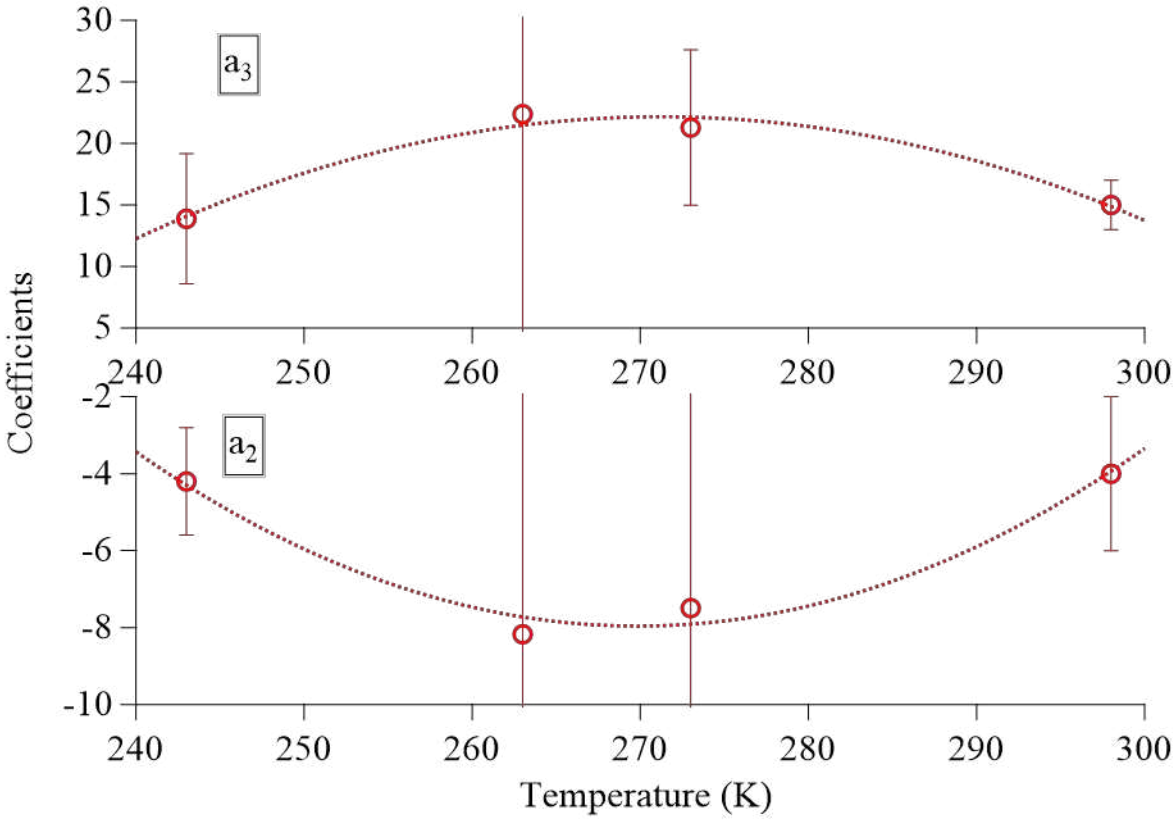

Figure C.v Polynomial fits of $a_{2\text{-}3}$ terms for $\chi^{2\text{-}3}$ (factor terms) as a function of temperature.

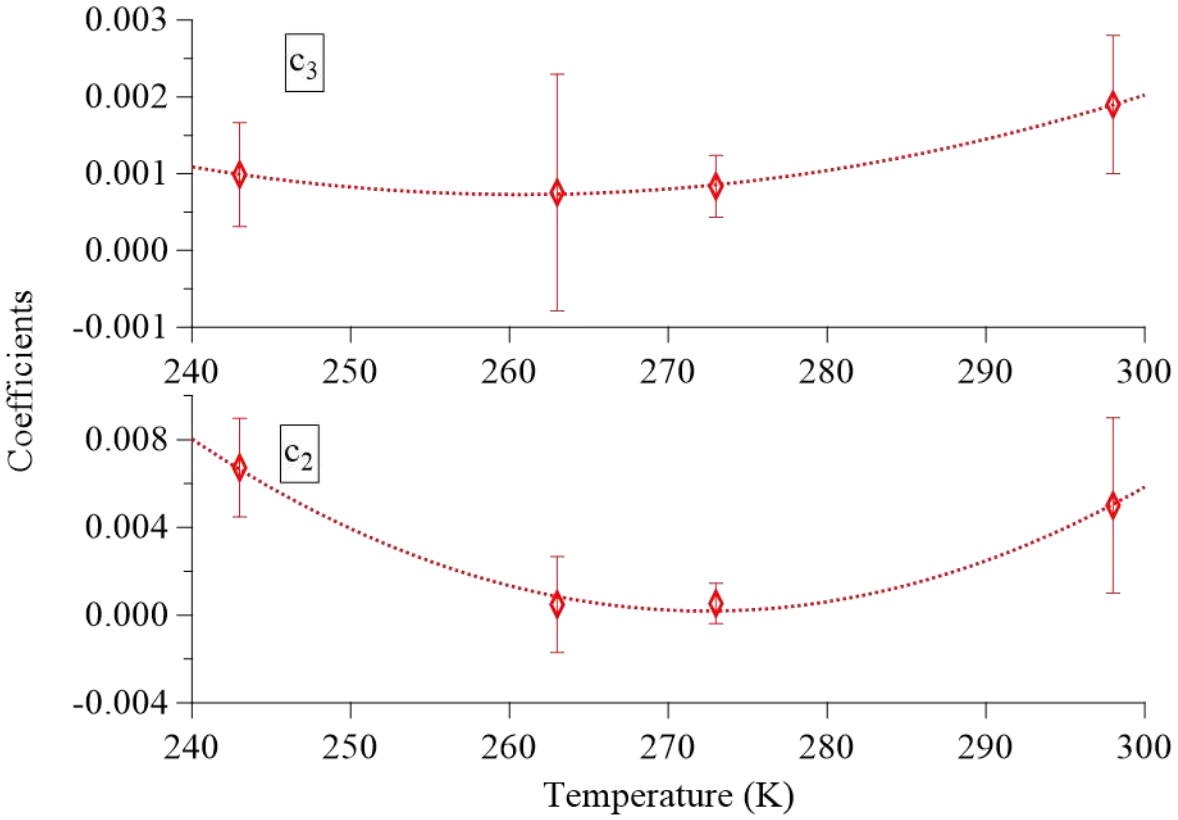

Figure C.vi Polynomial fits of $c_{2\text{-}3}$ terms for $\chi_{2\text{-}3}$ (exponent terms) as a function of temperature.

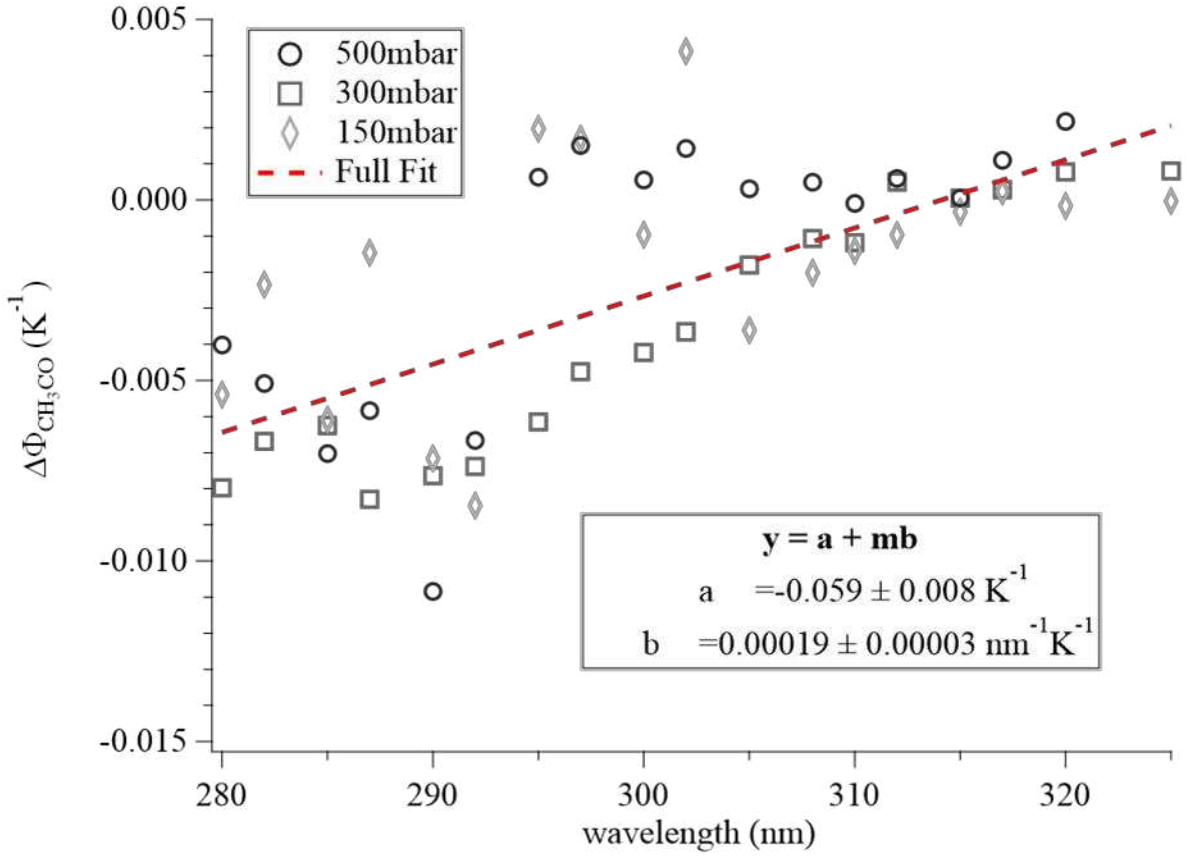

Figure C.vii Change in quantum yield with temperature ($\Delta\Phi_{CH_3CO}$) plotted as a function of wavelength for all pressures tested at 228 K. As described in the Ch. 3, our equations for calculating Φ_{CH_3CO} break down below 243 K, but Φ_{CH_3CO} can be calculated using a flat decrease of -0.4% K^{-1} for K = 243 – T. Application of a wavelength dependent $\Delta\Phi_{CH_3CO}$ was also attempted but produced poorer agreement with measurements than the wavelength-independent decrease. The data and fit for $\Delta\Phi_{CH_3CO}$ from 243 to 228 K as a function of wavelength are included here, along with the parameters for applying a wavelength-dependent $\Delta\Phi_{CH_3CO}$ for low temperatures.

APPENDIX D

SUPPORTING INFORMATION FOR CH. 3: Cl_2^- CHEMICAL IONIZATION MASS SPECTROMETRY (Cl_2-CIMS) FOR MEASUREMENT OF ACYL PEROXY RADICALS

Contents

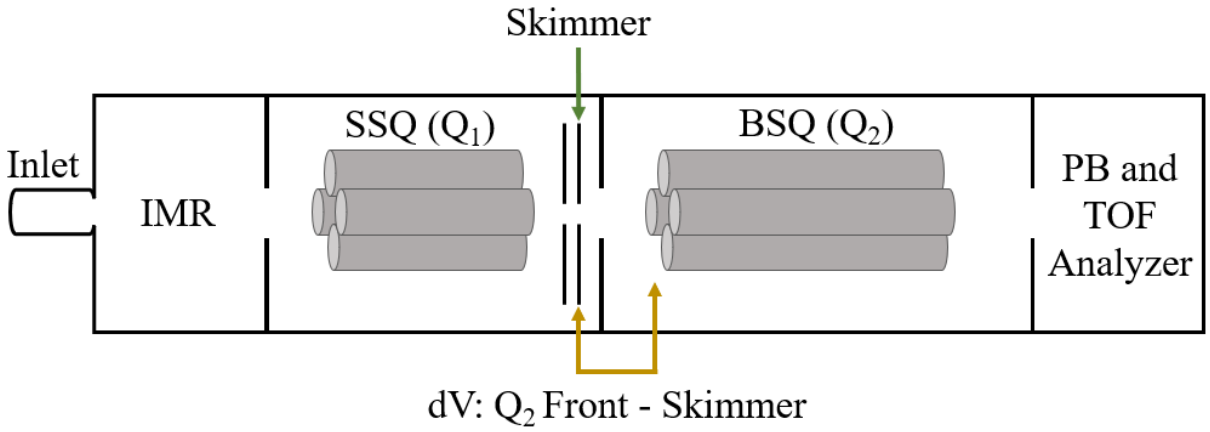

Figure D.i. Simplified diagram of the CIMS ion optics, including the ion-molecule reactor (IMR), short-segment quadrupole (SSQ), big-segment quadrupole (BSQ), primary beam (PB) and time-of-flight (TOF) mass analyzer segments (with PB and TOF segments combined for simplicity). During voltage scanning experiments, we altered the voltage difference (dV) between the front of the BSQ and the up-flow skimmer plate. For each voltage step, the skimmer plate voltage and the voltage settings of up-flow components were altered by the same amount to maintain constant dVs between adjacent components. The Q_2 Front and down-flow components remained unchanged across the dV scan steps. We maintained IMR total pressure of 65 mbar and water vapor pressure of 0.5 mbar for dV scan experiments. Normal operating dV was 1.4 V.

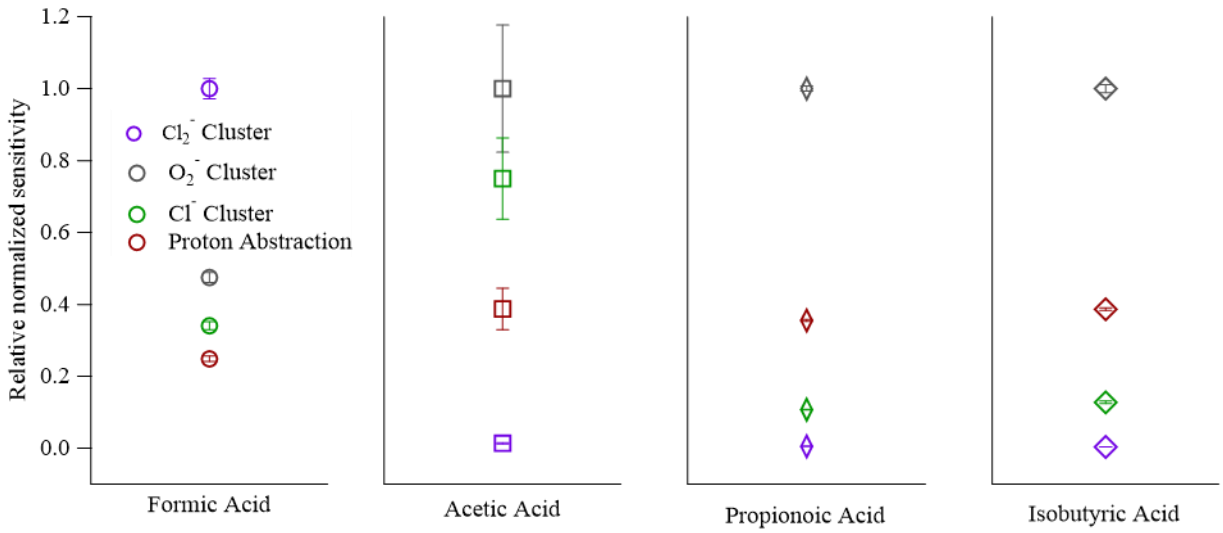

Figure D.ii Cl_2-CIMS sensitivities to examined organic acids. Sensitivities to various product ions at set relative to the most sensitive ion.

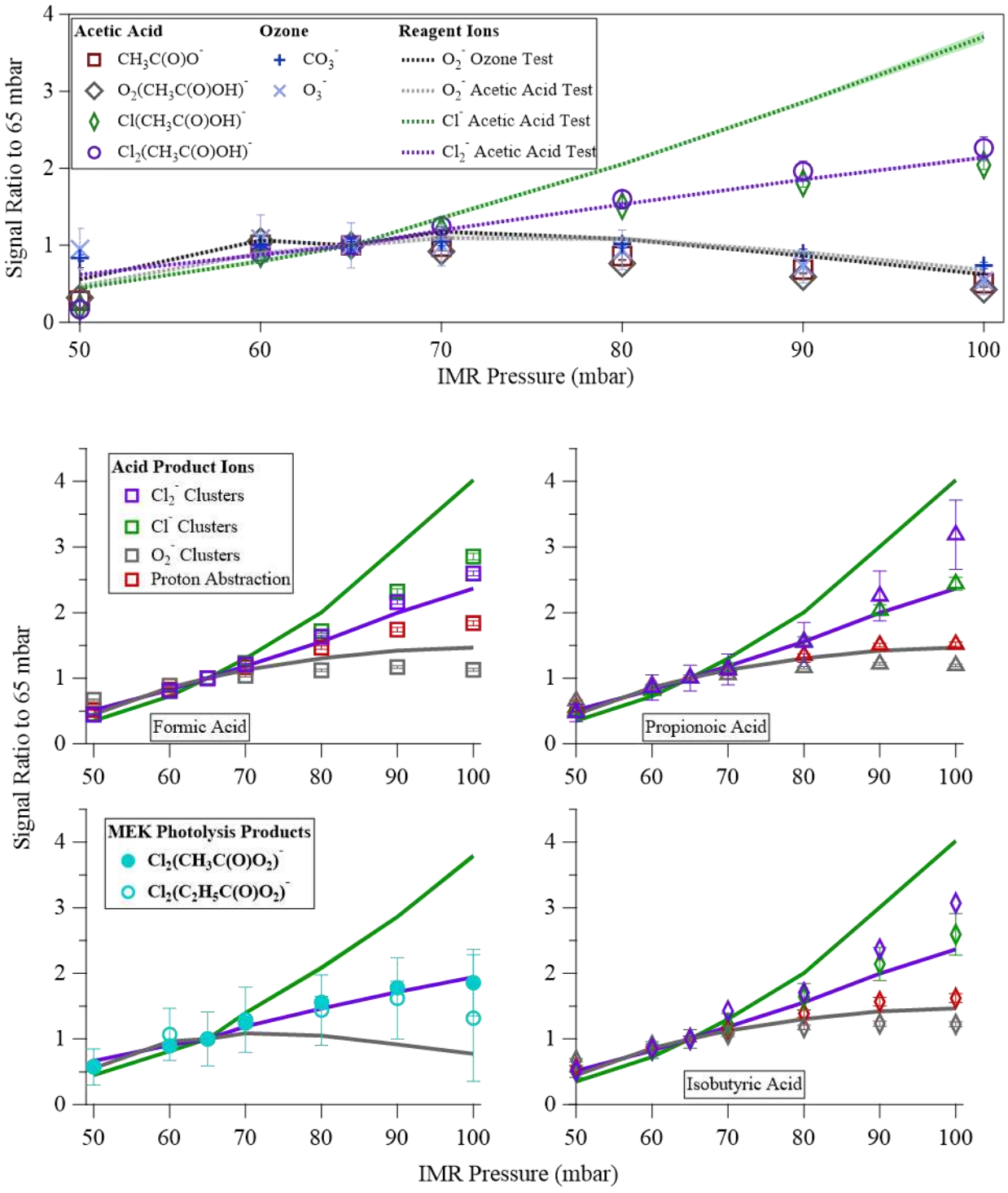

Figure D.iii Analyte ion signal responses to IMR pressure change (50 to 100 mbar), with background reagent ion counts at each pressure setting included (lines). During pressure change tests, we maintained IMR water vapor pressures of ca. 0.5 mbar and dV = 1.4 V between the skimmer and BSQ front. Error bars represent standard deviation of the signal average at each step. $Cl_2(C_3H_7C(O)OH)^-$ error bars not included for ease of visualization.

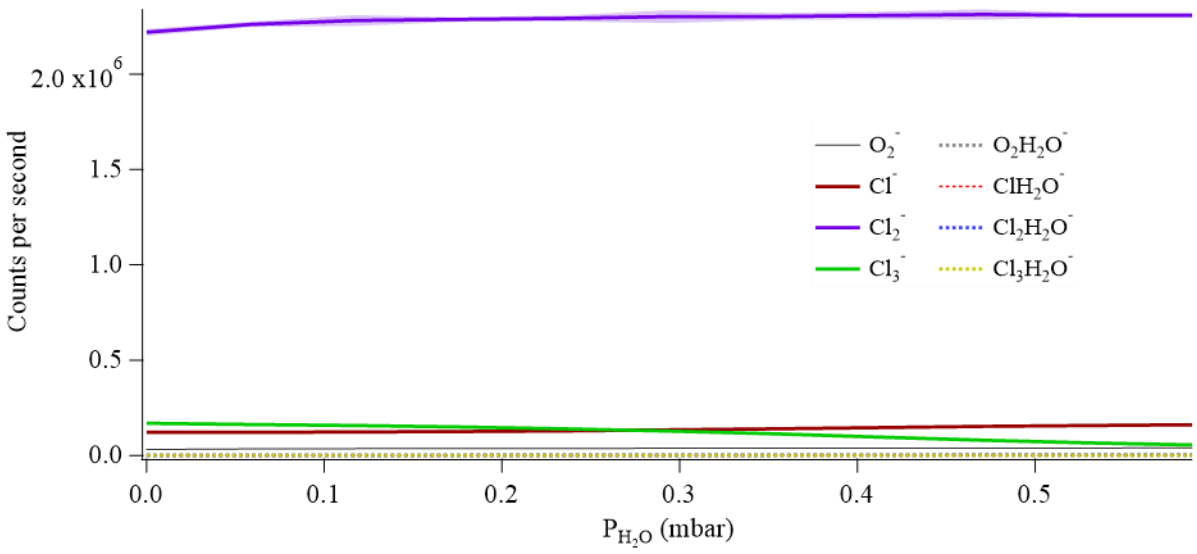

Figure D.iv Reagent ion response to changes in the ion-molecule reactor water vapor pressure. During water vapor pressure modulation, we maintained IMR pressure of 65 mbar and dV = 1.4 V between the skimmer and BSQ front.

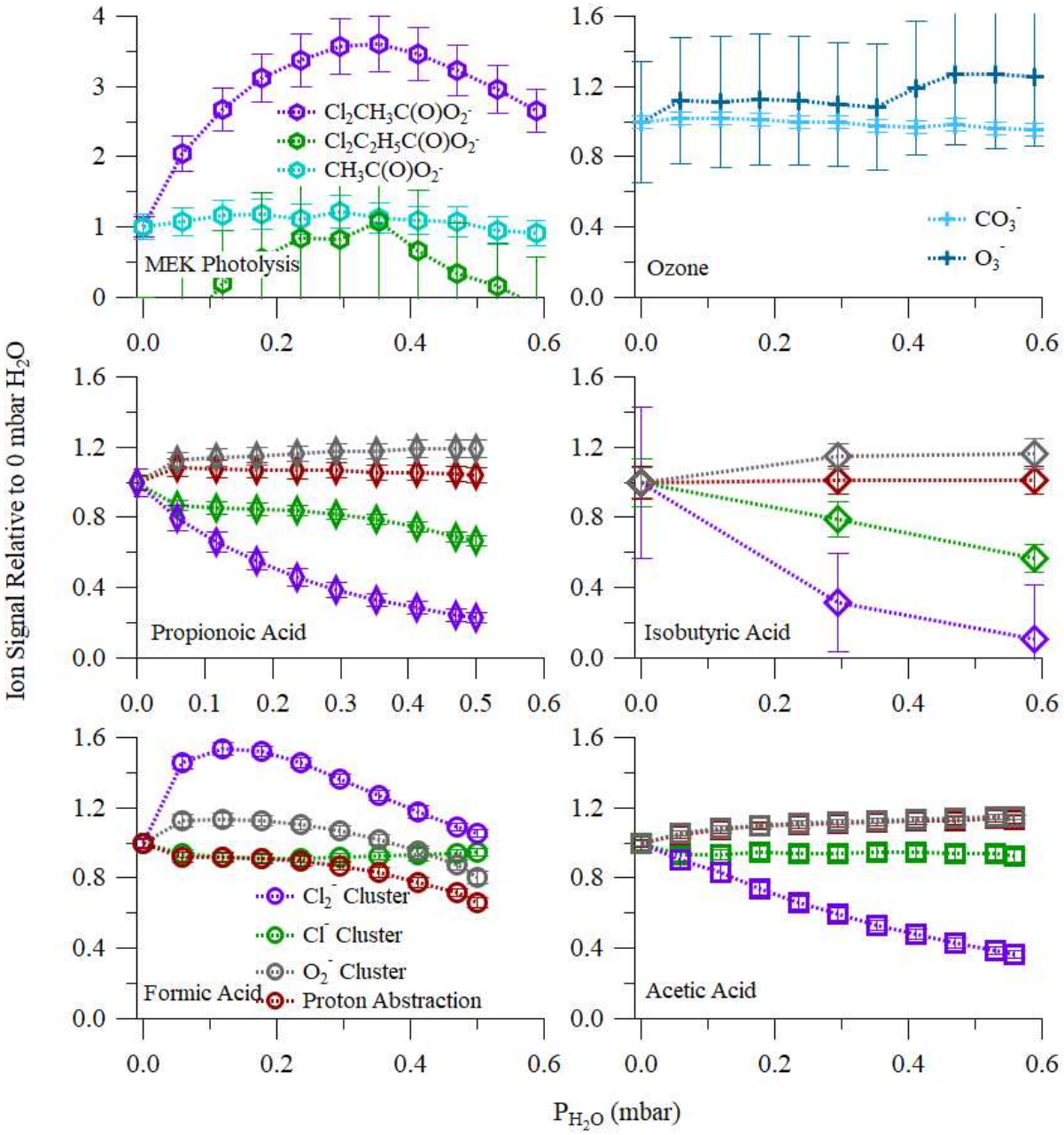

Figure D.v Data for ion-molecule reactor water vapor pressure impacts on analyte ion signal. Ion signal for each vapor pressure setting relative to signal from dry ion-molecule reactor. The influence of water vapor pressure on analyte detection was much larger than the observed impact on reagent ion signals. These impacts were also largest for Cl_2^- clusters and generally small (±20%) for ions that resulted from reaction with O_2^-.

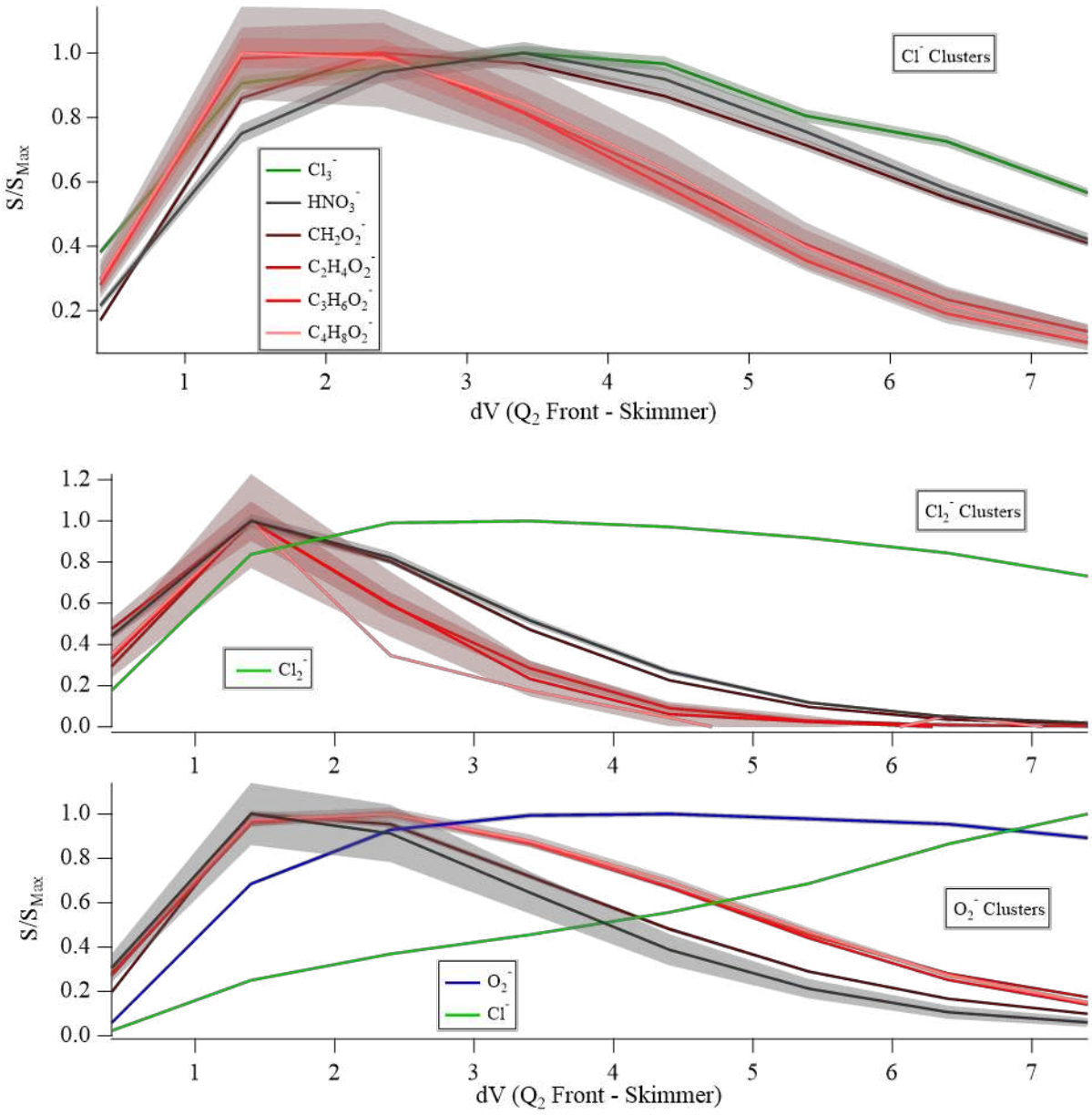

Figure D.vi dV scan data for the examined organic acids and HNO_3. (Upper) During dV scan tests of select standards, the dV_{50} for all Cl^- clusters was achieved at or below dV=~7.5, while the Cl_3^- dV_{50} exists somewhere slightly above this. This result suggests that Cl_3^- has a greater binding energy than Cl^- cluster binding energy with observed analyte ions and Cl^- transfer from Cl_3^- to any of the analytes studied here is unlikely. Included in middle and lower graphs are the Cl_2^- and O_2^- clusters signals across the same set of dV scan tests. Cl^- background signal change is included in with the O_2^- clusters and behaves similarly to the non-cluster analyte ions (H^+ abstraction products; not shown). Shading represents the 1σ SDs for each ion signal but is not shown for $Cl_2(C_4H_8O_2)^-$ for ease of visualization (less than 10 cps at any dV for this ion leads to large relative signal error).

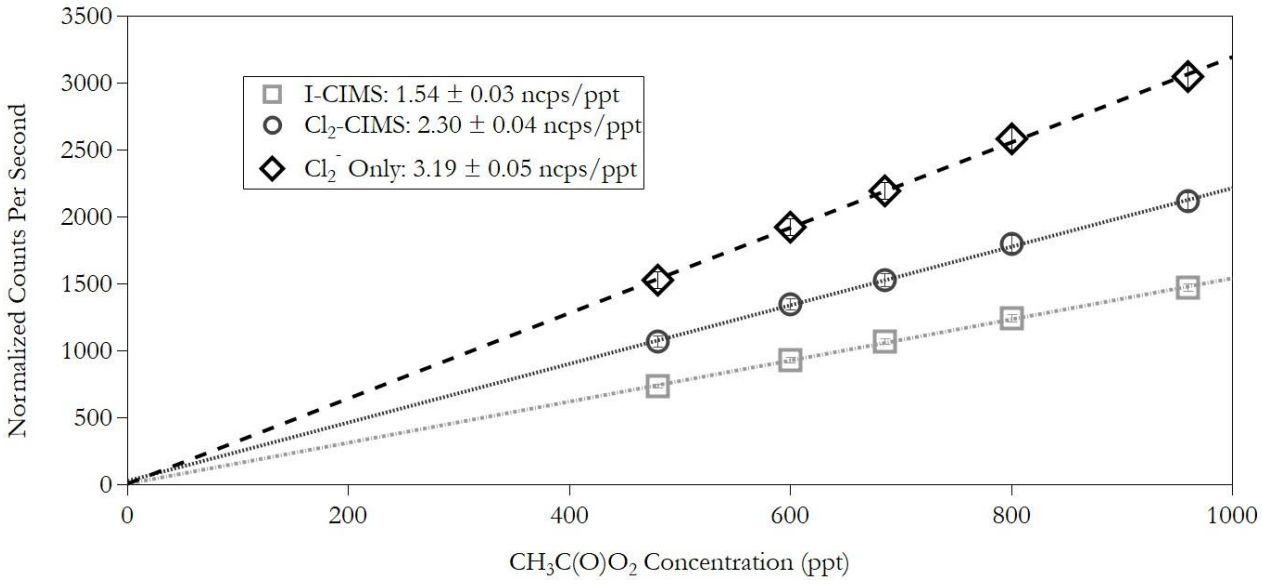

Figure D.vii 1-minute average signal (normalized per million reagent ions) for $X(CH_3C(O)O_2)^-$ (X = I or Cl_2) during $CH_3C(O)O_2$ calibrations. Light-gray squares represent $I(CH_3C(O)O_2)^-$ from the I-CIMS. Gray circles show $Cl_2(CH_3C(O)O_2)^-$ from the Cl_2-CIMS normalized to the sum of O_2^-, Cl^-, Cl_2^-, and Cl_3^-. Black diamonds also represent $Cl_2(CH_3C(O)O_2)^-$ but normalized to Cl_2^- only.

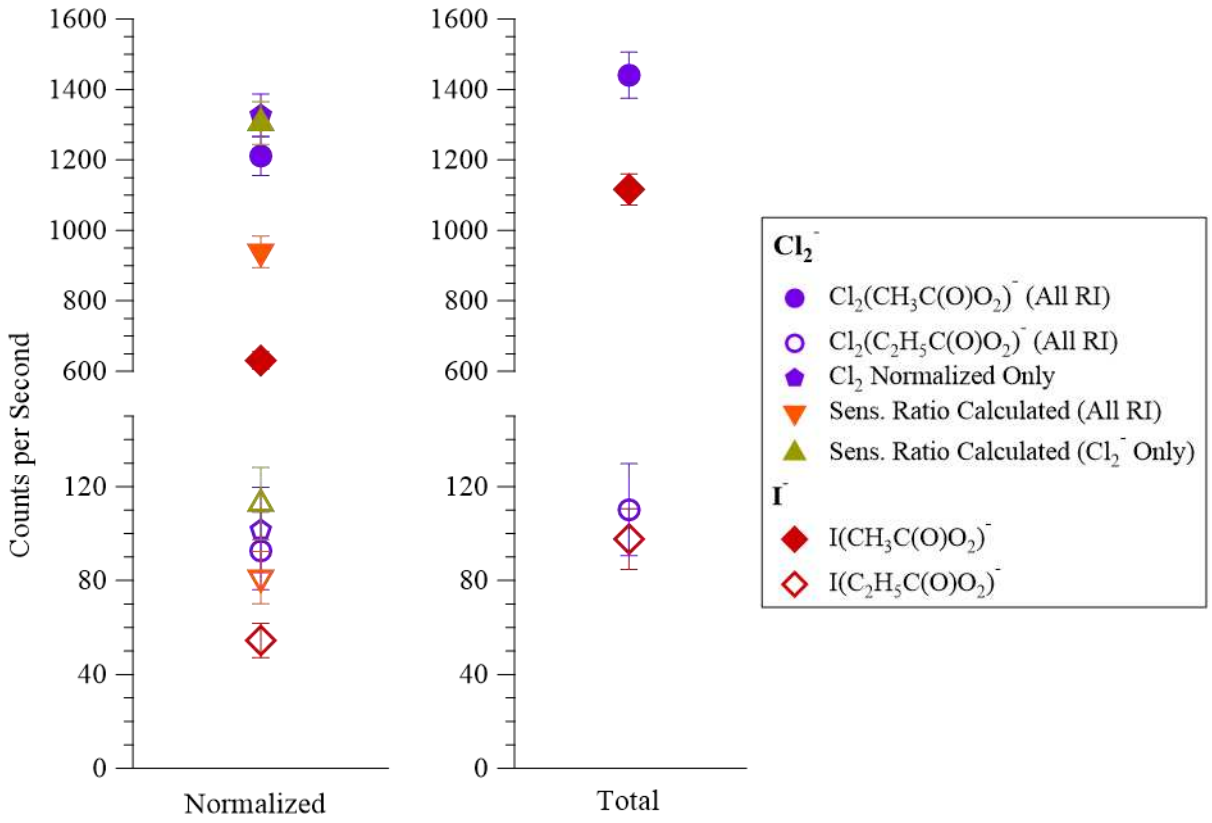

Figure D.viii Total (right) and normalized (left) signals from the MEK quantum yield tests (filled markers for $CH_3C(O)O_2$ and open markers for $C_2H_5C(O)O_2$). Cl_2-CIMS signals are shown normalized to total reagent ion signal (All RI; circles on left) and Cl_2^- only (pentagons). We produced expected Cl_2-CIMS signals (Sens. Ratio Calculated) by multiplying the I-CIMS normalized signal and the sensitivity ratios from PAN calibrations (Figure D.vii). Comparison of actual and expected counts normalized to Cl_2^- shows close agreement, while the expected signal from normalization to all reagent Cl_2-CIMS reagent ions is below the observed signal. This agreement of Cl_2^- normalized $RC(O)O_2$ signal ratios between the MEK photolysis tests and the $CH_3C(O)O_2$ calibrations occurs despite differences in the Cl_2 bulb concentration and age and resulting differences in Cl_2^- contribution to total reagent ion signal. This suggests a direct relationship between Cl_2^- background counts and $Cl_2(RC(O)O_2)^-$ signal across the two tests.

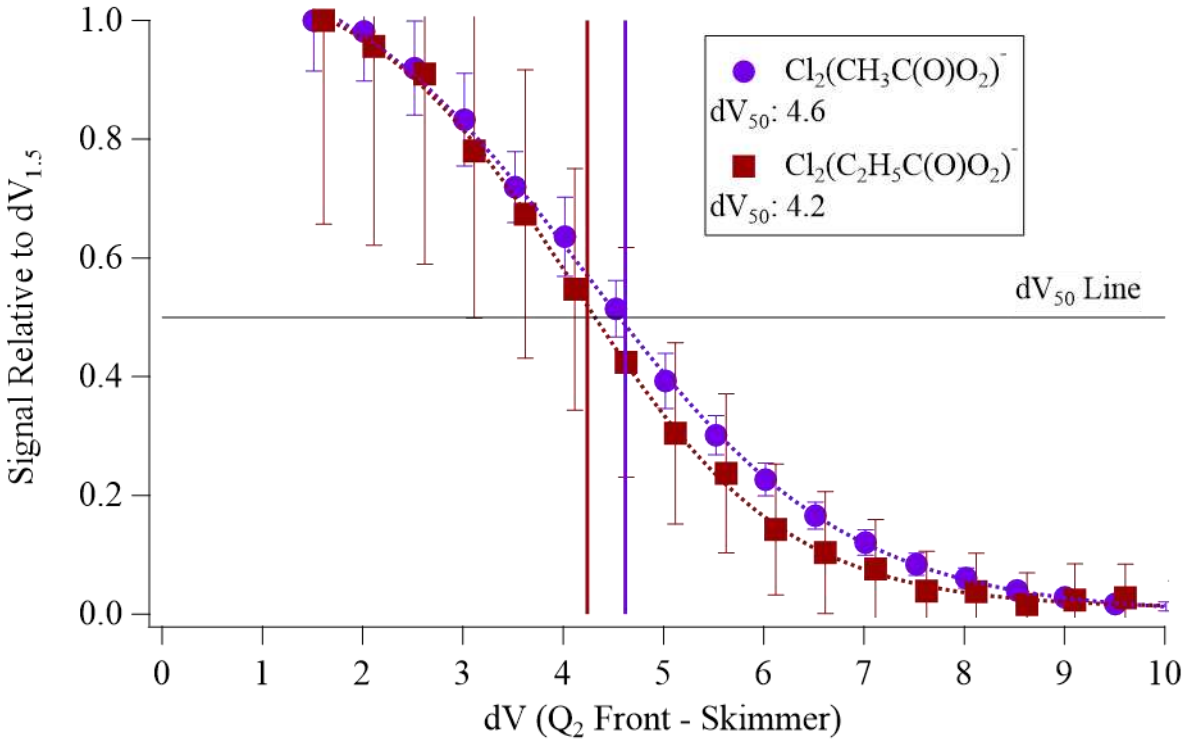

Figure D.ix dV scan data for $Cl_2(CH_3C(O)O_2)^-$ and $Cl_2(C_2H_5C(O)O_2)^-$ (ratio relative to dV = ~1.5) measured from MEK photolysis in the photolysis reactor system. Dashed lines represent sigmoidal fits to the analyte signal ratio data and solid vertical lines indicate the position of half-maximum signal in dV-space (dV_{50}). We use the similar dV_{50} values for $Cl_2(CH_3C(O)O_2)^-$ and $Cl_2(C_2H_5C(O)O_2)^-$ observed in this experiment to assume a similar cluster binding energy and, therefore, similar Cl_2^- CIMS sensitivity to $CH_3(O)O_2$ and $C_2H_5C(O)O_2$. $Cl_2(C_2H_5C(O)O_2)^-$ data shifted by +0.2 dV for ease of visibility.

		Reagent Ion							
		O_2^-		Cl^-		Cl_2^-		Cl_3	
Analyte	**Ion**	R^2	*Slope*	R^2	*Slope*	R^2	*Slope*	R^2	*Slope*
Nitric Acid	NO_3^-	0.96	0.26	0.66	-0.97	0.89	-0.70	0.77	-0.03
	$O_2NHO_3^-$	1.00	0.98	0.72	-3.65	0.93	-2.60	0.79	-0.13
	$ClHNO_3^-$	0.99	-0.46	0.73	1.73	0.93	1.23	0.79	0.06
	$Cl_2HNO_3^-$	0.95	-0.32	0.92	1.36	1.00	0.89	0.54	0.03
Formic Acid	$HC(O)O^-$	1.00	1.02	0.93	-2.55	1.00	-1.86	0.72	-0.11
	$O_2HC(O)OH^-$	1.00	1.01	0.92	-2.52	1.00	-1.85	0.74	-0.11
	$ClHC(O)OH^-$	0.92	-0.43	0.68	0.96	0.86	0.76	0.95	0.05
	$Cl_2HC(O)OH^-$	0.92	-0.26	1.00	0.72	0.96	0.50	0.50	0.02
Acetic Acid	$CH_3C(O)O^-$	0.99	1.02	0.90	-2.54	0.98	-1.86	0.74	-0.11
	$O_2CH_3C(O)OH^-$	0.99	1.03	0.91	-2.54	0.98	-1.87	0.74	-0.11
	$ClCH_3C(O)OH^-$	0.99	-0.85	0.95	2.16	1.00	1.56	0.68	0.09
	$Cl_2CH_3C(O)OH^-$	0.75	-0.21	0.94	0.62	0.83	0.41	0.29	0.02
Propanoic Acid	$C_2H_5C(O)O^-$	0.98	1.01	0.95	-3.73	0.99	-2.38	0.67	-0.12
	$O_2C_2H_5C(O)OH^-$	0.98	1.01	0.95	-3.73	0.99	-2.38	0.67	-0.12
	$ClC_2H_5C(O)OH^-$	0.95	-0.42	1.00	1.63	0.98	1.01	0.55	0.04
	$Cl_2C_2H_5C(O)OH^-$	0.52	-0.18	0.74	0.79	0.59	0.44	0.11	0.01
Isobutyric Acid	$C_3H_7C(O)O^-$	0.99	1.03	0.80	-4.23	0.96	-3.29	0.63	-0.12
	$O_2C_3H_7C(O)OH^-$	0.99	1.03	0.80	-4.24	0.96	-3.29	0.63	-0.12
	$ClC_3H_7C(O)OH^-$	0.84	-0.31	0.93	1.50	0.97	1.09	0.35	0.03
	$Cl_2C_2H_5C(O)OH^-$	0.06	0.05	0.05	0.19	0.00	0.00	0.39	-0.02
Ozone	O_3^-	0.99	0.98	0.75	-3.11	0.90	-2.59	0.71	-0.11
	CO_3^-	0.99	0.98	0.75	-3.12	0.90	-2.59	0.70	-0.11
Acetyl Peroxy Radical	$CH_3C(O)O^-$	0.98	0.93	0.77	-5.70	1.00	-3.74	0.72	-0.14
	$CH_3C(O)OO^-$	0.99	0.99	0.75	-6.03	1.00	-3.98	0.73	-0.15
	$Cl_2CH_3C(O)OO^-$	0.30	0.12	0.00	0.02	0.18	-0.36	0.72	-0.03

Table D.x R^2 and slopes for all correlation fits of analyte ions and reagent ion counts presented in Figures 4.v. $Cl_2CH_3C(O)OO^-$ data from the initial 40 ppm tank test are shown here. Linear fits of $Cl_2CH_3C(O)OO^-$ data to the retest of Cl_2 concentration correlations with 40 ppm and 10 ppm Cl_2 tanks (Figure D.xi) returned Slope = 0, R^2 = 0.002 and Slope = 0.53, R^2 = 0.99, respectively.

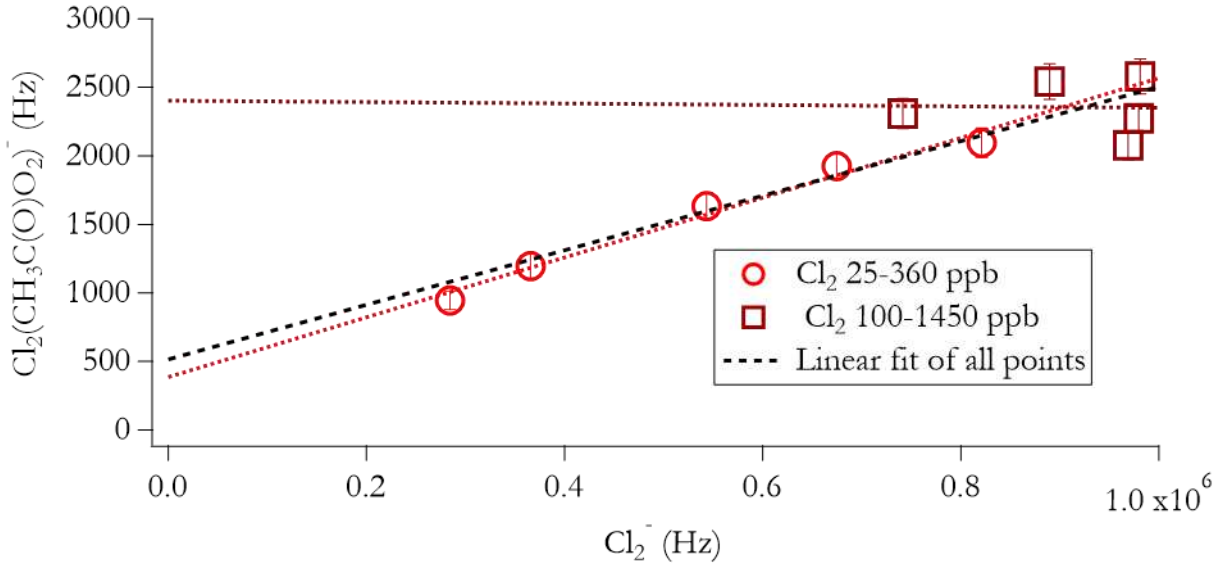

Figure D.xi Observed relationship between $Cl_2(CH_3C(O)O_2)^-$ (produced by acetone photolysis) and Cl_2^- during alteration of the Cl_2 reagent gas mixture. 10 ppm Cl_2 cylinder (25-360 ppb Cl_2 in reagent gas mixture) data shown with light red circles and 40 ppm cylinder (100-1450 ppb Cl_2 in reagent gas mixture) data shown with dark red diamonds. Dotted lines are the linear least-squared fits to the 10 ppm and 40 ppm datasets, the black dashed line is the linear least-squared fit to the whole dataset. Cl_2 concentrations from the 40-ppm tank reflect those used for acid and ozone response in Figure 4.v and Table D.x. The non-linear relationship between Cl_2^- background counts and $Cl_2(CH_3C(O)O_2)^-$ signal here indicates that $Cl_2(CH_3C(O)O_2)^-$ was only directly dependent on Cl_2^- up to Cl_2 reagent gas concentrations of ca. 400 ppb. Past this concentration, it is possible that secondary chemistry in the IMR, perhaps involving reactions of Cl with $CH_3C(O)O_2$, diminishes observed sensitivity. Further testing of this reagent ion system is needed to stabilize and maximize Cl_2^- CIMS response to $RC(O)O_2$.

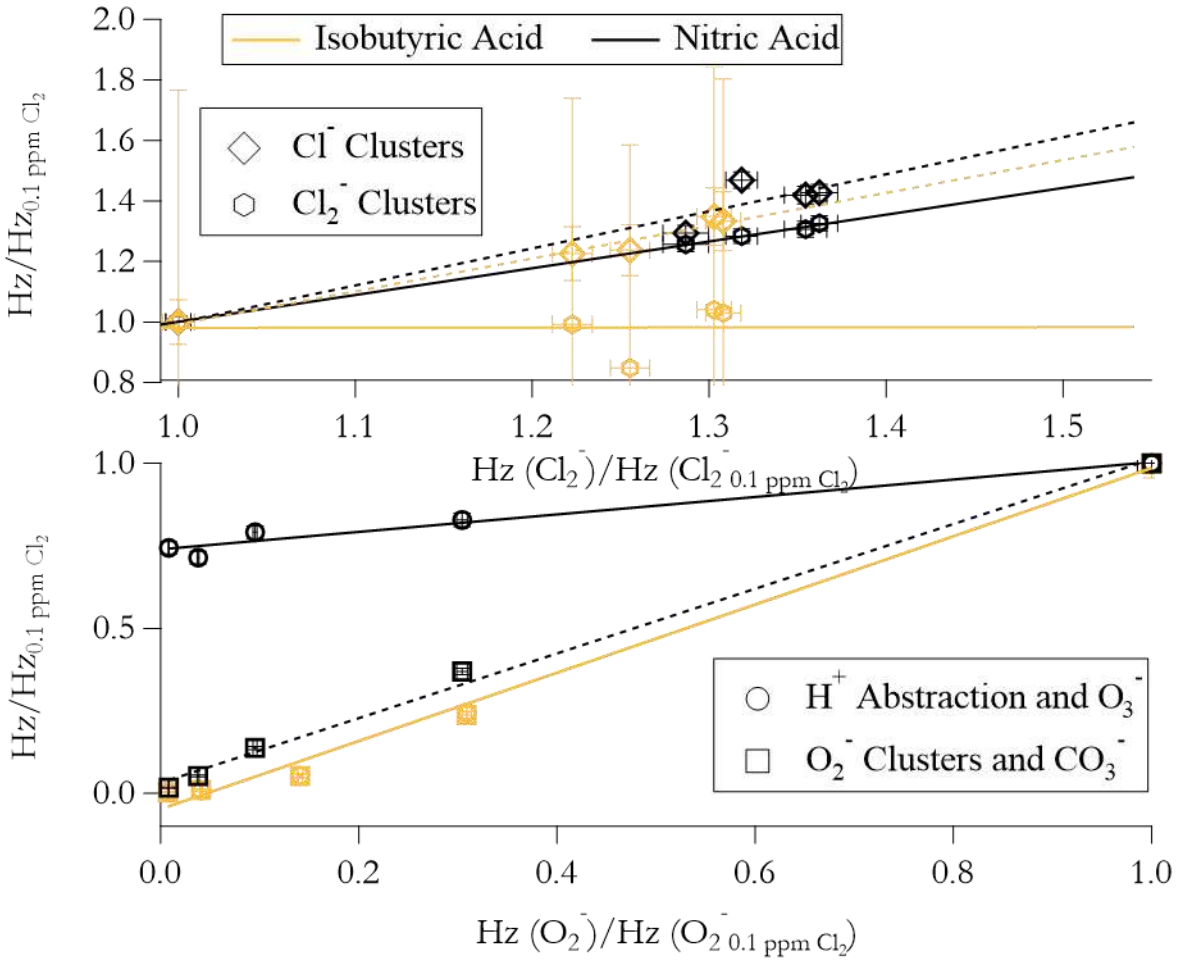

Figure D.xii Analyte ion correlation plots for analytes not included in Figure 4.v. These are organized in the same manner as the plot in Ch. 4. Isobutyric acid was left off to improve readability of the graph. Isobutyric acid-Cl^- clusters behaved similarly to other organic acids. Cl_2^- cluster sensitivity was poor. We did not calibrate the Cl_2-CIMS for HNO_3. HNO_3 was examined in this test for an expected reaction with Cl_3^- (See Amelynck et al. reference[108]) from Ch. 4. No HNO_3 product ion correlates clearly to Cl_3^-. dV scans indicated that Cl_3^- was more tightly bound than any analyte ion, including those of HNO_3. Cl_3^- was less reactive than expected from limited literature information.